

REPORT DOCUMENTATION PAGE			Form Approved OMB NO. 0704-0188		
<p>The public reporting burden for this collection of information is estimated to average 1 hour per response, including the time for reviewing instructions, searching existing data sources, gathering and maintaining the data needed, and completing and reviewing the collection of information. Send comments regarding this burden estimate or any other aspect of this collection of information, including suggestions for reducing this burden, to Washington Headquarters Services, Directorate for Information Operations and Reports, 1215 Jefferson Davis Highway, Suite 1204, Arlington VA, 22202-4302. Respondents should be aware that notwithstanding any other provision of law, no person shall be subject to any penalty for failing to comply with a collection of information if it does not display a currently valid OMB control number.</p> <p>PLEASE DO NOT RETURN YOUR FORM TO THE ABOVE ADDRESS.</p>					
1. REPORT DATE (DD-MM-YYYY) 06-10-2014		2. REPORT TYPE Ph.D. Dissertation		3. DATES COVERED (From - To) -	
4. TITLE AND SUBTITLE Holographic recording and applications of multiplexed volume bragg gratings in photo-thermo-refractive glass			5a. CONTRACT NUMBER W911NF-10-1-0441		
			5b. GRANT NUMBER		
			5c. PROGRAM ELEMENT NUMBER		
6. AUTHORS Daniel B. Ott			5d. PROJECT NUMBER		
			5e. TASK NUMBER		
			5f. WORK UNIT NUMBER		
7. PERFORMING ORGANIZATION NAMES AND ADDRESSES University of Central Florida 12201 Research Parkway, Suite 501 Orlando, FL 32826 -3246			8. PERFORMING ORGANIZATION REPORT NUMBER		
9. SPONSORING/MONITORING AGENCY NAME(S) AND ADDRESS (ES) U.S. Army Research Office P.O. Box 12211 Research Triangle Park, NC 27709-2211			10. SPONSOR/MONITOR'S ACRONYM(S) ARO		
			11. SPONSOR/MONITOR'S REPORT NUMBER(S) 58500-EL-HEL.27		
12. DISTRIBUTION AVAILABILITY STATEMENT Approved for public release; distribution is unlimited.					
13. SUPPLEMENTARY NOTES The views, opinions and/or findings contained in this report are those of the author(s) and should not be construed as an official Department of the Army position, policy or decision, unless so designated by other documentation.					
14. ABSTRACT Volume Bragg grating (VBG) structures are capable of diffracting incident light into a single diffraction order with high efficiency given the Bragg condition is met. The Bragg condition depends on both the wavelength and angle of the incident light making VBGs useful for filtering and manipulating both the wavelength and angular spectrum of a source. Recent research in the holographic recording of volume Bragg gratings in photo-thermo-refractive (PTR) glass has shown that these gratings are extremely useful components in high power laser systems for spectral narrowing, transverse mode control, beam combining, and pulses stretching and compression.					
15. SUBJECT TERMS PTR glass, volume hologram, volume Bragg grating					
16. SECURITY CLASSIFICATION OF:			17. LIMITATION OF ABSTRACT UU	15. NUMBER OF PAGES	19a. NAME OF RESPONSIBLE PERSON Leonid Glebov
a. REPORT UU	b. ABSTRACT UU	c. THIS PAGE UU			19b. TELEPHONE NUMBER 407-823-6983

Report Title

Holographic recording and applications of multiplexed volume bragg gratings in photo-thermo-refractive glass

ABSTRACT

Volume Bragg grating (VBG) structures are capable of diffracting incident light into a single diffraction order with high efficiency given the Bragg condition is met. The Bragg condition depends on both the wavelength and angle of the incident light making VBGs useful for filtering and manipulating both the wavelength and angular spectrum of a source. Recent research in the holographic recording of volume Bragg gratings in photo-thermo-refractive (PTR) glass has shown that these gratings are extremely useful components in high power laser systems for spectral narrowing, transverse mode control, beam combining, and pulses stretching and compression.

This dissertation expands upon previous research in PTR VBGs by investigating multiplexed volume Bragg gratings and their applications in laser systems. By integrating several VBGs into the same volume of PTR, splitting and combining elements have been developed that allow for high power beam combining with significantly reduced complexity. Several configurations of multiplexed beam combiners are demonstrated for both spectral and coherent combining systems with high power results giving 420 W with 96% efficiency. Multiplexing was also used to produce unique phase structures within VBG. This effect was exploited to create extremely narrowband spectral filters called moiré Bragg gratings. The technical challenges of producing moiré gratings in bulk glass has revealed new insights into PTR glass and narrowband filtering of 15 pm in the near infrared was achieved and applied to longitudinal mode selection in a laser cavity. Finally, the possibility of increasing the level of multiplexing has been investigated. This has led to scaling the number of beam combining channels, integrated multi-notch filters, and generated several potentially interesting devices for future research. The summation of this work indicates a promising future for multiplexed VBGs in PTR glass.

HOLOGRAPHIC RECORDING AND APPLICATIONS OF MULTIPLEXED VOLUME
BRAGG GRATINGS IN PHOTO-THERMO-REFRACTIVE GLASS

by

DANIEL BERNARD OTT

B.S. Rose-Hulman Institute of Technology, 2007

M.S. University of Central Florida, 2011

A dissertation submitted in partial fulfillment of the requirements
for the degree of Doctor of Philosophy
in CREOL, The College of Optics and Photonics
at the University of Central Florida
Orlando, FL

Spring Term
2014

Major Professor: Leonid Glebov

ABSTRACT

Recent developments in holographic recording of volume Bragg gratings (VBGs) in photo-thermo-refractive (PTR) glass have demonstrated their utility as components in high power laser systems for spectral narrowing, transverse mode control, beam combining, and pulse stretching/compression. VBG structures are capable of diffracting incident light into a single diffraction order with high efficiency given the Bragg condition is met. The Bragg condition depends on both the wavelength and angle of the incident light making VBGs useful for filtering and manipulating both the wavelength and angular spectrum of a source.

This dissertation expands upon previous research in PTR VBGs by investigating multiplexed VBGs and their applications in laser systems. Multiplexing involves the integration of several VBGs into the same volume of PTR glass. This process enables the fabrication of splitting and combining elements which have been used for high power beam combining with significantly reduced complexity as compared to other combining schemes. Several configurations of multiplexed beam combiners were demonstrated for both spectral and coherent combining systems with high power results yielding a combined power of 420 W with 96% efficiency. Multiplexing was also used to produce unique phase structures within VBGs. This effect was exploited to create extremely narrowband spectral filters called moiré Bragg gratings. The technical challenges of producing moiré gratings in bulk glass have revealed new insights into the use of PTR glass as a recording medium and produced devices capable of narrowband filtering of only 15 pm in the near infrared. Experiments were performed using such devices as intra-cavity laser elements for longitudinal mode selection. Investigations have also been made into increasing the level of multiplexing possible within PTR glass. These explorations included

scaling the number of beam combining channels, fabrication of integrated multi-notch filters, and generated several other potentially interesting devices for future research. The summation of this work indicates a promising future for multiplexed VBGs in PTR glass.

ACKNOWLEDGMENTS

My primary source of inspiration and support during graduate school was Christina Willis. She was always able to keep me on track whenever I questioned my commitment to this doctorate. Her emotional support has been invaluable during this process. Of course she also falls into the top of the categories for family, friend, and colleague. It's wonderful to have a partner that can relate to the struggles of graduate school. Meeting her was definitely the best and least expected outcome of pursuing a PhD at CREOL.

The support from my parents is what kicked off this whole journey. I want to thank my parents for their encouragement to pursue this degree and I certainly acknowledge their hands in my success. I'm blessed to have come from a happy home with loving and caring parents. They were my first teachers and provided a world of opportunities to help me develop mental and physical skills that I needed. The sense of hard work that they instilled in me has served me very well. My siblings have also been a source of support for me. As Rebecca and Andrew pursue their own graduate degrees it's nice to hear of their experiences and successes. Having grown up together, we can relate on level much different than I share with other friends. This level of support means a lot to me and I'm glad to share such camaraderie with them. Best of luck in your careers. My youngest sibling, Audrey almost certainly thinks we are all crazy for staying in school for so long. I'm very excited to see what she gets up to in the years to come. Finally, to my new family of in-laws, thank you all for your loving support and welcoming me so graciously into your family.

I have been very fortunate to have a number of great friends that have also been a source of support through the years. I don't often get to see my friends from high school, but I hold dear the times we do get into contact. Their enthusiasm for this degree and the excitement for when I show up in Des Moines has really helped inspire me to keep on. From Colorado, Kristen Vannoy was one of the most personally close friends I ever had. Our conversations were always therapeutic. Of course my Orlando friends were the closest support system that I had during my time in grad school. One of the reasons that I came to CREOL was because I liked the people here, and I definitely met a lot of great folks during my time here. Certainly they kept me sane during the last five plus years. I'm excited to catch up with them again after the postdoctoral diaspora has shaken out.

I'm also indebted to my colleagues at CREOL and the members of PPL. There is much overlap between social and work circles and it has made work a true pleasure. I have been sincerely fortunate to work with so many brilliant people. Solving problems, or coming up with new ones, was never really a problem when surrounded by such great minds. It's always odd to step back and recognize what a weird little bubble of intelligence we live and work in. I specifically would like to thank Ivan Divliansky, Vasile Rotar, Julien Lumeau, Boris Zeldovich, George Venus, and Leon Glebov for being my primary sources of mentorship, advice, and guidance. I've learned an incredible amount and owe this dissertation to being able to stand on their shoulders.

I would like to also thank the Directed Energy Professional Society (DEPS) for the DEPS Graduate Directed Energy Scholarship in High Energy Lasers for 2011-2013. The projects that I worked on were partially funded by the following agencies: HEL/JTO, AFRL, and NASA. I can't stress enough how nice it was to be well funded by CREOL, these agencies, and Dr. Glebov throughout my graduate career.

TABLE OF CONTENTS

LIST OF FIGURES	ix
LIST OF TABLES	xx
1 INTRODUCTION	1
Comparison of Filtering Properties of Dispersive Elements	2
Spectral Filtering by Fabry-Perot Etalon	6
Diffraction by a Volume Bragg Grating	9
Coupled Wave Theory to Describe VBGs.....	13
Recording Materials for VBGs	20
Recording Methods for VBGs	31
Multiplexed Gratings	34
2 ADVANCES IN HOLOGRAPHIC RECORDING.....	41
Aberrations of Recording Beams.....	41
Phase Stabilization During Holographic Recording	53
3 SINGLE VBGs FOR LASER APPLICATIONS.....	76
4 MULTIPLEXED GRATINGS FOR BEAM STEERING.....	83
Scaling Multiplexed Channels for High Power Spectral Beam Combining.....	84
2x TBG for Coherent Beam Combining.....	93

4x RBG for Coherent Beam Combining.....	100
5 MOIRÉ BRAGG GRATING.....	113
Theoretical Description.....	116
Measurement of Axial Profile.....	125
Sources of Decreased Peak Transmission.....	142
Application in a Laser System	150
6 MANY CHANNEL MULTIPLEXED VBGS.....	158
Broadband Mirrors and Multi-notch Filters.....	159
Broad Angle Mirror	162
Many Channel Splitter	169
7 CONCLUDING REMARKS.....	176
LIST OF REFERENCES	179

LIST OF FIGURES

Figure 1: Common methods for creating angle/wavelength selectivity. a.) prism b.) thin transmitting diffraction grating c.) blazed grating in the Littrow condition d.) thick transmitting grating.	3
Figure 2: A model of a Fabry Perot etalon. Light incident at θ is reflected by factors of r for external reflections and r' for internal reflections. The total reflectivity from each pass is given on the right hand side of the etalon.	7
Figure 3: Read out geometries two types of VBGS. a.) shows the transmitting Bragg grating and b.) the reflecting Bragg grating along with basic designations of tilt.	10
Figure 4: The off axis recording geometry for the recording of transmitting and reflecting Bragg gratings. The angle of incidence (θ) of the recording beams inside of the media determines the resonance properties of the final grating. Recording is shown in purple, transmitting Bragg grating readout in green and reflecting Bragg grating readout in red.	12
Figure 5: The spectral response of an RBG with a period of 360 nm, thickness of 4.0 mm and RIM of 270 ppm to light incident at 10° and detuned from a wavelength of 1064 nm.	15
Figure 6: The angle response of an RBG with a period of 360 nm, thickness of 4.0 mm and RIM of 270 ppm to light at 1064 nm wavelength and detuned from an angle of incidence of 10°	16
Figure 7: The spectral response of a TBG with a period of 3 μm , thickness of 2.0 mm and RIM of 270 ppm to light incident at 10° and detuned from a wavelength of 1064 nm.	16
Figure 8: The angle response of a TBG with a period of 3 μm , thickness of 2.0 mm and RIM of 270 ppm to light at 1064 nm wavelength and detuned from an angle of incidence of 10°	17

Figure 9: The design curve for the spectral selectivity (FWHM) of a reflecting Bragg grating with efficiency of 99% at a number of common laser wavelengths.	20
Figure 10: The change in refractive index in exposed PTR depends on the applied photo-dosage as well as the development time.	29
Figure 11: Two methods for producing reflection and transmission holograms.	32
Figure 12: Recording setup for holographic exposure for producing VBGs in PTR glass.	33
Figure 13: The deteriorated spectral response of an RBG recorded with a single wave of each Zernike aberration. Plots show various probe locations and the various rows show different subsets of the Zernike aberrations.....	46
Figure 14: The appearance of the primary aberrations when viewed by a shear plate with a lateral shear of approximately 1/3 of the beam radius.	48
Figure 15: The shear plate image of the recording beam at the output of the beam condition portion of the holographic recording setup.	49
Figure 16: A simulation of a shear plate image using two parts spherical, one part coma and two parts of either defocus or astigmatism.	50
Figure 17: The expected deterioration of a 20 mm RBG with 20 ppm RIM in the presence of the measured aberrations of the recording beam assuming worst possible contributions.	52
Figure 18: The decrease of visibility as the variation in phase fluctuations increases. Phase variation σ is shown as a fraction of the recording wavelength. Detail is shown on different scales in the inset.	58

Figure 19: The VBG recording setup showing the paths of the recording/probe beam. The side view shows how the beam is split between a recording portion and a probe portion for measuring phase.	59
Figure 20: Ramping of the PZT voltage allows a shift in the detector voltage, centered about the DC level, to be converted to a fraction of a phase shift once the period is determined. Red line shows a fit to the experimental data in blue.....	60
Figure 21: Diagram of a retroreflector in a phase stabilization system with designation of variables for calculating lateral sensitivity.	62
Figure 22: Experimental setup to demonstrate the lateral sensitivity of a TBG in comparison to a corner cube retroreflector. The PZT is used to shift the respective measurement device. The effect of lateral shift on the signal measured at the detector is monitored.	64
Figure 23: The interference signals received from measurements of lateral sensitivity of a TBG in red and a retroreflector in blue.....	66
Figure 24: The phase before and during the recording of a baseline, unstabilized RBG.	68
Figure 25: The transmission spectrum of a RBG that was recorded without stabilization. The measured data is in red and theoretical fit in blue.	69
Figure 26: The phase and PZT signal before and during a recording using phase stabilization in the presence of high frequency phase noise.....	70
Figure 27: Transmission spectrum of the RBG recorded with phase stabilization in the presence of high frequency noise. The measured data is in red and theoretical fit in blue.	70
Figure 28: The phase and PZT signal before and during the recording of a RBG with phase stabilization and long term drift.....	72

Figure 29: Transmission spectrum of the RBG recorded with phase stabilization in the presence of long term drift. The measured data is in red and theoretical fit in blue.....	72
Figure 30: A comparison of the phase drift of the recording system (red) to the temperature at the recording plane (blue), demonstrating a close correlation of the phase drift to temperature.	74
Figure 31: A narrowband RBG with bandwidth 24 pm and 32% efficiency with resonant wavelength of 976.75 nm.....	77
Figure 32: Design curve of the angular selectivity of an unslanted 100% diffraction efficiency TBG with resonant wavelength of 1064 nm using grating thickness and Bragg angle as design parameters.	78
Figure 33: The angular selectivity of a TBG designed for transverse mode selection of a beam with 0.5 mm diameter. Measured results (dots) are in excellent agreement with theoretical calculations (line).....	79
Figure 34: The angular selectivity of a twice over-modulated TBG designed for transverse mode selection of a beam with 0.5 mm diameter. Measured results (dots) are in excellent agreement with theoretical calculations (line). For comparison, the angular selectivity of the similar non-over-modulated TBG is shown as red dashes.	81
Figure 35: Schematic of a 2x multiplexed RBG for spectral beam combining using a third out of resonance input to combine three beams.	85
Figure 36: The diffraction efficiency of the two arms of a 2x RBG for SBC measured by probing along the combining arm with a low power tunable laser. Efficiency is >99% with bandwidth of 215 pm +/- 10 pm.....	86
Figure 37: The housing for thermally controlling the multiplexed RBG for beam combining. ...	88

Figure 38: The fraction of power present along the grating thickness for an RBG designed for 1064 nm with 230 ppm RIM shows that 90% of the power is reflected within the first quarter of the grating.	89
Figure 39: A reflection only multiplexed grating for spectral beam combining of four laser channels.....	90
Figure 40: The reflection spectrum of the four channel spectral beam combining with each channel demonstrating combining efficiencies above 98%.....	91
Figure 41: Coherent beam combining using a multiplexed 2x TBG to couple two laser cavities.	94
Figure 42: The basic operation of a multiplexed TBG being used as a high efficiency splitter on the left and a high efficiency combiner on the right.	96
Figure 43: The experimentally measured angular selectivity of a 2x TBG for CBC tested as a splitter. Arm 1 and Arm 2 refer to the left and right splitting arm as viewed from above.	97
Figure 44: System for testing the performance of a multiplexed TBG (M-TBG) for coherent beam combining.....	99
Figure 45: Coherent beam combining using a multiplexed RBG to couple two laser cavities. .	100
Figure 46: Source of parasitic resonance due to multiplexing. Bragg angles that are multiples of each other will allow Arm 1 to be reflected by the grating for Arm 2 at the normal incidence Bragg wavelength.	101
Figure 47: Using a 4x RBG as beam combiner and as a beam splitter. The loss ports exhibit the direction of light if the efficiency of the overall device is not high enough or if misalignment is present.	102

Figure 48: The diffraction efficiency of each arm of the 4x RBG for CBC using a probe beam at normal incidence to the grating.....	105
Figure 49: A series of wavelength spectra of efficiency of each arm at different angles of incidence with respect to the grating normal.	105
Figure 50: The design for a new multiplexed RBG for CBC targeting better alignment and equality of grating strength.	107
Figure 51: Overmodulated multiplexed RBG for CBC used as a splitter. Total reflection efficiency is high, but reflected arms do not produce flat top spectral response due to higher detuning selectivity for thicker RBGs.....	110
Figure 52: The spectral response of a multiplexed RBG for CBC measured as a splitter at a thickness that meets the minimum individual DE requirement.	110
Figure 53: An undermodulated multiplexed RBG for CBC measured as a splitter. The expected combining efficiency is low, but overlap of the spectral response in each reflected arm is very good.....	111
Figure 54: The moiré pattern formed by two overlapping sinusoids with slightly different periods. The points of constructive and destructive interference produce a secondary visual pattern.	113
Figure 55: A simulated image of a moiré Bragg pattern is shown above and the corresponding RIM is shown below. At the zero points of the RIM, a phase shift can be seen in the high frequency modulation.	116
Figure 56: A single period of the moiré envelope is decomposed into the two mirrors and cavity analogous to a Fabry-Perot etalon.....	119

Figure 57: A comparison of the FPE method (blue) and full couple wave analysis (red) of an MBG. Left shows full spectrum and right shows just resonant transmission. Grating parameters are: envelope period = 7.5 mm, grating thickness = 7.5 mm, $n_1=n_2=130$ ppm, $\lambda_0=1064$ nm, resulting in a transmission bandwidth FWHM of 5 pm.....	122
Figure 58: A design curve showing transmission bandwidth for moiré Bragg gratings. Design parameters are the period of the moiré envelope and the refractive index modulation.	123
Figure 59: An MBG demonstrating above 90% transmission. Green dots show measured results, Blue shows FPE theory and Red is coupled wave theory. The primary cause of reduction of transmission efficiency is the difference of the reflectance of each cavity mirror.	124
Figure 60: An image of an MBG used for demonstrating methods for determining the envelope profile. Photo-darkening of different regions is evident.	126
Figure 61: Setup for testing the axial profile of an MBG using losses.....	127
Figure 62: The transmission through the transverse direction of the MBG for measuring spatially dependent combined losses.....	128
Figure 63: The wavefront data of double pass transmitted light at 633 nm through the face of an MBG.	129
Figure 64: The line profile near the center of the wavefront data taken with the Zygo interferometer.....	129
Figure 65: Using diffraction to measure the transverse profile of an MBG. Due to the large thickness of the grating and angle of incidence, there is a wide cone of diffraction that occurs.	130
Figure 66: The cone of diffraction is able to be imaged from the scattering of blue light when measuring an MBG in a transmission grating geometry.	131

Figure 67: Scanning an MBG for diffraction with positive and negative angles of incidence allows maxima and minima to be located easily since the diffraction in the two arms will be equal at these points as shown here.	132
Figure 68: The diffraction efficiency of an MBG measured as a transmission grating in the transverse direction. Using the symmetry of the scans at positive and negative angles of incidence (AOI) allows the locations of the maxima and minima of the envelope pattern to be determined.....	133
Figure 69: An alternative diffraction measurement for determining the axial profile of an MBG utilizing only the primary transmission ray.	134
Figure 70: The signal from an axial scan of an MBG using only the primary transmission ray to determine the locations of the envelope zeros.	135
Figure 71: A summary of the measured locations of envelope zeros of an MBG using different transverse measurement techniques.....	136
Figure 72: The spectral transmission of the MBG that was cut to produce a phase shift in the center of the volume using the aggregated results of the transverse measurement techniques. .	137
Figure 73: Side view of the recording of an MBG in PTR (a) and a top view of an unprocessed grating (b) along with the cutting locations for producing a tilted MBG with sine and cosine envelope profiles.....	138
Figure 74: The transmission spectrum of an MBG obtained at the point of minimum transmission bandwidth of 30 pm corresponding to a sinusoidal envelope profile.	139
Figure 75: The transmission spectrum of an MBG obtained at the point of maximum transmission bandwidth of 90 pm corresponding to a cosine envelope profile.....	140

Figure 76: The FWHM bandwidth of the transmission peak across a tilted MBG shows a sinusoidal tunability with horizontal position.....	141
Figure 77: The peak transmittance of the MBG resonance across the face of a tilted MBG shows consistently high transmission that is unaffected by the envelope pattern.	141
Figure 78: An MBG spectrum demonstrating the effect of a gradient of resonant wavelength approximately equal to the bandwidth of the transmission peak.....	144
Figure 79: The relative increase in the spectral width of the filter ($\Delta\lambda_{out}$) due to a relative change in the resonant wavelength across the working aperture.	145
Figure 80: The drop in peak transmission due to a relative change in the resonant wavelength across the working aperture.	146
Figure 81: The vertical gradient in a MBG recorded in a low absorption PTR glass melt.	148
Figure 82: The transmission spectrum of a MBG recorded in low absorption glass with 15 pm transmission bandwidth and 90% transmission. Solid red is CWT simulation and blue dots are measured values.....	149
Figure 83: The setup for characterization of the spectral transmission of an MBG with a high resolution tunable laser. A 3 dB coupler is used to determine alignment by monitoring the intensity of back reflection from the gratings rejection band.	151
Figure 84: Transmission spectra of an MBG in PTR glass with length = 5.3 mm, refractive index modulation $n_1=126$ ppm, $n_2=234$ ppm. Blue – theory, red – experiment.	152
Figure 85: Angular selectivity of an MBG in PTR glass with length = 5.3 mm, refractive index modulation $n_1=126$ ppm, $n_2=234$ ppm. Blue – theory, red – experiment.	153

Figure 86: A fiber laser with free space section of cavity incorporating a MBG for mode selection. A scanning Fabry Perot interferometer is used to determine the longitudinal modes present in the laser.	154
Figure 87: The spectrum of the output of the fiber laser system operating without an MBG in the cavity as measured by scanning Fabry Perot etalon.	155
Figure 88: The spectrum of the output of the fiber laser system operating with an MBG in the cavity as measured by scanning Fabry Perot etalon, demonstrating a reduction of the longitudinal modes to a total of three.....	155
Figure 89: Examples of many channel multiplexed gratings. From left to right: broadband mirror, broad angle mirror, and many channel splitter.	158
Figure 90: The transmittance spectrum of a broadband mirror distinct, seperated spectral responses for each grating. Results demonstrate the recording of 18 gratings in one piece of PTR with a rejection efficiency greater than 90%.	161
Figure 91: The use of a broad angle mirror to increase the number of back reflections for a divergent beam.....	163
Figure 92: The transmission spectrum of a five channel broad angle mirror. Blue shows the measured transmission through the device. Red shows the transmission spectrum of a single RBG with a thickness of 10.45 mm and RIM of 100 ppm.	165
Figure 93: The angular acceptance of the five channel broad angle mirror for light at 1063.90 nm. Blue shows measured data. Red shows the angular acceptance of a 10.45 mm grating with RIM of 100 ppm.....	167

Figure 94: The angular acceptance of the five channel broad angle mirror at different angles of incidence. The top row shows the response to wavelengths higher than nominal resonance and the lower row shows the response for wavelengths lower than the nominal wavelength of 1063.90 nm.	168
Figure 95: The many channel splitter can be used in several ways. a.) shows the use as a coherent 1:N splitter, b.) shows the system reversed to give a coherent N:1 combiner, and c.) shows a wavelength demultiplexer which is achieved by using a different angle of incidence.....	170
Figure 96: The transmission spectrum of the coherent splitter, as measured with a tunable laser. Reflected light is split into 20 channels separated by 0.75°	171
Figure 97: The reflection bandwidth of the 20 channel multiplexed VBG depends on the angle of incidence of light on the grating structure. Incidence at 10° gives a coherent beam splitter/combiner. At angles far from normal, the device acts as a wavelength division de/multiplexer.	172
Figure 98: At an angle of incidence of 7° , the individual gratings start to decouple and the spectra start to shift away from each other. At this alignment, the gratings acting independently with an efficiency of about 30%.	174

LIST OF TABLES

Table 1: A comparison of the first order diffraction efficiencies for various types of thin gratings [3].	5
Table 2: The wavefront profile for the various Zernike aberrations.	43
Table 3: Wavefront error of the recording beams measured at various locations.	52
Table 4: The M^2 values of beams reflected from a four channel multiplexed reflecting Bragg grating.	92

LIST OF ACRONYMS

AOI – angle of incidence

CBC – coherent beam combining

CWT – coupled wave theory

DE – diffraction efficiency

FBG – fiber Bragg grating

FPE – Fabry-Perot etalon

FSR – free spectral range

FWHM – full width at half maximum

MBG – moiré Bragg grating

P-V – peak to valley

ppm – parts per million

PSG – phase-shifted grating

PTR – photo-thermo-refractive

PZT – piezo-electric transducer

RBG – reflecting Bragg grating

RIM – refractive index modulation

RMSE – root mean square error

SBC – spectral beam combining

SVEA – slowly varying envelope approximation

TEC – thermo-electric cooler

TBG – transmitting Bragg grating

VBG – volume Bragg grating

WFE – wavefront error

WFS – wavefront sensor

1 INTRODUCTION

The primary goal of this dissertation is to discuss methods for manipulating properties of light. This can be as simple as controlling the direction of a laser beam. While mirrors are the standard optical device to achieve redirection of light, other devices do exist to fill this role. Beyond the simple direction of a beam of light, it is important to understand that any light source will generate some spectrum of angles as well as a spectrum of wavelengths that can also be manipulated. The extent of these spectra will vary depending on the source, with a light bulb filament as an example with very broad angle and wavelength spectra. The light generated by laser sources is typically far removed from the light bulb filament in terms of the angle and wavelength content. In fact, when first introduced to the concept of a laser we are told that these sources have a single wavelength (monochromatic) and are highly directional. Relatively speaking this is true, but upon closer inspection, there does exist a narrow wavelength spectrum and some level of divergence (angular spectrum) for any laser source. Being able to control either or both of these spectra is extremely important for the development of laser systems and applications that use laser light. Because of the very narrow band of spectral content that exists in a typical laser beam, specialized tools are needed to filter or otherwise manipulate the light in both the angular and wavelength domain. Volume Bragg gratings (VBGs) are one such tool for filtering laser light in wavelength or angle. These devices will be the primary focus of this dissertation as they are able to produce high efficiency filters by diffraction into a single order. This is extremely critical for high power laser systems, where the purpose is to efficiently generate as much optical power and avoid losses which contribute to heating. In particular, the

goal of this work is to demonstrate novel devices that are comprised of multiple grating structures recorded within the same volume. The resulting multiplexed filters have a number of unique properties that allow tailoring of filtering properties such that new applications for volume gratings can be explored. In order to understand the benefits of using thick volume structures and set the stage for the properties of multiplexed volume gratings, it is necessary to compare the performance of these devices to other common optical filters.

Comparison of Filtering Properties of Dispersive Elements

For optical filtering in the wavelength or angular domains, one of the most common methods for filtering is the use of a dispersive element. Examples of several common dispersive devices are shown in Figure 1. All display a level of angular dispersion in that they are able to convert a wavelength into a specific angle of deviation and can therefore be used in applications like spectroscopy where it is desirable to filter, with high resolution, various wavelengths. Figure 1a shows the separation of input light into different angular components using a simple prism. These angularly separated components are then accessible by placing a pinhole at the appropriate location to select the desired spectral component.

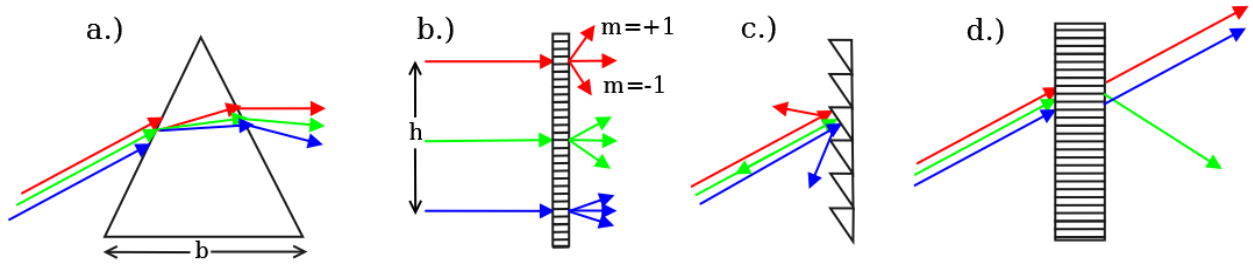


Figure 1: Common methods for creating angle/wavelength selectivity. a.) prism b.) thin transmitting diffraction grating c.) blazed grating in the Littrow condition d.) thick transmitting grating.

$$\Delta\lambda_{min} = \frac{\lambda}{b \frac{dn}{d\lambda}} \quad (1)$$

The spectral resolution of a prism is determined by balancing the angular dispersion induced by the prism and the minimum resolvable slit, due to diffraction, used to select the desired spectral region. This resolution is given by Eq. 1, with b being the length of the prism base, λ is the central wavelength, and $dn/d\lambda$ is the dispersion of refractive index at λ . So, while narrow bandwidths on the order of tens of picometers are possible, prisms must become very large or be made of highly dispersive glass.

A more compact geometry is the surface or thin grating shown in Figure 1b and c. Thin gratings are often used in place of prisms due to their ability to create higher levels of dispersion without the bulk of prisms and without the restrictions of the prism dispersion on the spectral resolution. Surface gratings are created using holographic recording using the interference of two plane waves, lithographic recording using a phase plate to transfer a grating profile into a photosensitive material, or mechanical ruling to inscribe a grating pattern into a substrate [1].

The result of these processes is a periodic phase or amplitude profile. The most basic grating is composed of a sinusoidal phase or amplitude profile. Light incident on this surface will diffract in discrete orders governed by the grating equation, Eq. 2.

$$m \lambda = \Lambda (\sin \theta_m + \sin \theta_i) \quad (2)$$

Here, Λ is the period of the grating, λ is the wavelength of the incident light and θ_i is the angle of incidence with respect to the grating normal. The value m indicates the order of diffraction and the value θ_m is the output angle that the diffracted light makes with respect to the grating normal. It is evident that the thin grating will produce an angular spread of the incident light that depends on the wavelength of the light and multiple diffraction orders will be created. The resolution of such a grating can be calculated by determining the change in wavelength that is acceptable before the m order for that wavelength overlaps with the $m+1$ or $m-1$ order of the central wavelength of the incident light. This resolution is given by:

$$\Delta\lambda_{min} = \frac{\lambda^2}{w \sin \theta_m} \quad (3)$$

The minimum wavelength selectivity is determined by the central wavelength λ , the width of the beam w , and the angle of the diffracted order θ_m . Like prisms, mentioned previously, gratings are commonly found in moderate resolution (~ 100 pm) spectrum analyzers and are often used in favor of prism due to their greater angular dispersion [2]. Comparison of Eq. 3 and Eq. 1 shows that thin gratings are able to achieve narrower wavelength selectivity compared to prisms of a

similar size. Additional benefits of the diffraction grating include the relative ease of producing gratings for any wavelength and diffraction gratings formed by acousto-optic modulators have the ability to create actively tunable diffraction gratings. The maximum efficiency of a thin diffraction grating is dictated by the type of grating that is used. Table 1 shows a comparison of the various types of thin gratings. Amplitude gratings consist of period changes in transparency and phase gratings consist of periodic changes of the refractive index. Blazed gratings are a special category of thin gratings which rely on surface reflections from a periodic sawtooth pattern. These exhibit very high theoretical bandwidth at the design wavelength and broadband performance, though resolving power remains the same since the diffraction pattern follows the same relations as a classic thin grating.

Table 1: A comparison of the first order diffraction efficiencies for various types of thin gratings [3].

<u>Thin Grating profile:</u>	<u>Zero-Order, %</u>	<u>First Order, %</u>
Sinusoidal amplitude	25	6.25
Square-wave amplitude	25	10
Sinusoidal phase	10	33.9
Square-wave phase	0	40.25
Classical blazed	0	100

In summary, the dispersive elements here form a class of very common filtering elements that are able to transform a wavelength spectrum into an angular spectrum such that filtering can be achieved. Relatively high resolution and efficiency is possible with these devices, but several other technologies exist that can outperform dispersive elements. These devices will be discussed in the subsequent sections.

Spectral Filtering by Fabry-Perot Etalon

Dispersive elements are only one type of optical filter. Other filtering devices include absorption, thin film, Lyot, Fabry-Perot and atomic line filters in the spectral domain and simple angular selective filters such as pinholes and lenses in the spatial domain [4-7]. A full review of these filters would reveal a long list of features and drawbacks. Fundamentally, the method by which they achieve spectral and angular filtering differs from the primary topic of this dissertation, volume Bragg gratings. There does exist one type of common spectral filter, the Fabry-Perot etalon, that does have a strong relation to the multiplexed volume Bragg gratings that will be discussed in later sections. Because of the close relation to VBG filters, it is important to discuss the properties of Fabry-Perot filters in detail.

Filtering by the Fabry-Perot cavity is achieved in both the angle space and wavelength space, but it is most commonly used as a spectral filter. This narrow band filter can be formed by using two high reflectivity mirrors as in the case of a laser resonator, or by the surface reflections from a plate in the case of an etalon (FPE). The diagram in Figure 2 shows the operation of a simple FPE with light incident at an arbitrary angle.

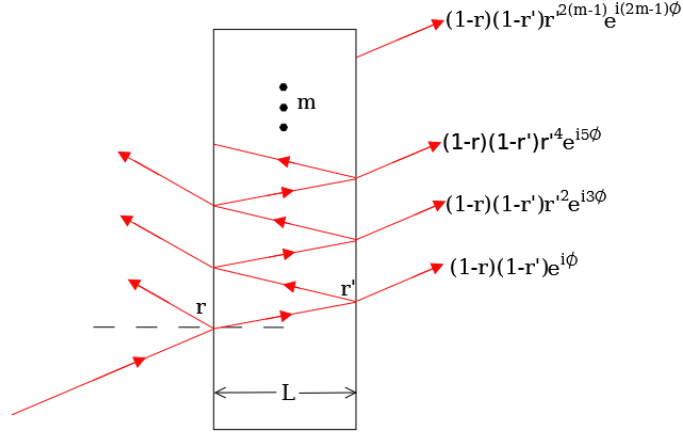


Figure 2: A model of a Fabry Perot etalon. Light incident at θ is reflected by factors of r for external reflections and r' for internal reflections. The total reflectivity from each pass is given on the right hand side of the etalon.

The surface reflections serve as cavity mirrors and propagation through the media serves as the cavity. By summing the amplitude and phase of the transmitted light generated by the series of multiple reflections and propagations through the cavity, the output transmission spectrum can be calculated. The results for the transmission spectrum are shown in Eq. 4.

$$T = \frac{1}{1 + \left(\frac{2F}{\pi}\right)^2 \sin^2 \frac{2\pi nL \cos \theta}{\lambda}} \quad (4)$$

The transmittance is governed by the index of refraction of the cavity n , the wavelength of light λ , the length of the cavity L and the angle made within the cavity θ , as shown in Figure 2. The spectrum of a FPE contains multiple narrow linewidth peaks which are separated by the free spectral range (FSR). The FSR is a measure of the density of longitudinal modes which are allowed to resonate in the cavity and is given by Eq. 5. The parameter F is the finesse. The

finesse determines the quality of the cavity and relates the spectral width of the narrow bandpass filter to the distance between the filter peaks which is characterized by the FSR. The finesse is defined as follows for a cavity formed by two mirrors of unequal reflectivity:

$$FSR_{\lambda} = \frac{\lambda^2}{2nL} \quad (5)$$

$$F = \frac{FSR_{\lambda}}{\Delta\lambda} = \frac{\pi(R_1 R_2)^{1/4}}{1 - \sqrt{R_1 R_2}} \quad (6)$$

Here, R_1 and R_2 represent the reflectance of the individual mirrors in Figure 2. Typically R_1 and R_2 are equal, or at least assumed to be, but for the formulation of theory in later sections, this formula has been kept generalized. An inequality of the mirror reflectance will result in a decreased peak transmission given by Eq. 7. As the metric for determining the quality of an etalon, the finesse can be affected by any source of misalignment or error, such as tilts or surface errors in the mirrors [8].

$$T_{max} = \frac{(1 - R_1)(1 - R_2)}{(1 - \sqrt{R_1 R_2})^2} \quad (7)$$

FPEs are extremely sensitive to the quality of the input beam. The spectral width and the angular selectivity of an FPE are directly proportional with a ratio of around 0.3 rad/nm [9]. Therefore, FPEs require well collimated beams and have low angular acceptance. Also, due to the larger number of cavity round trips for a high finesse cavity, absorption losses will exhibit a large effect

on the total output power. For mirror reflectivity of above 90%, the effects of absorption can be amplified by 300 to 10,000 times which results in a lowering of the peak transmission and increase of the filter's spectral width [10]. The sensitivity of the FPE is demonstrated by the effect of surface roughness on the spectrum. Root mean square error (RMSE) roughness of 15 nm is enough to induce scattering of 10% which can allows for rejection band light to leak through the filter [11].

$$\Delta\lambda = \frac{\lambda^2(1 - R)}{2 \pi L \sqrt{R}} \quad (8)$$

The FPE is one of the narrowest optical filters with spectral widths determined by mirror reflectivity. The spectral width of a lossless FPE cavity with $R_1=R_2$ is given by Eq. 8. The resonator length also contributes to the spectral width of the resonator, making longer resonators desirable. A longer cavity also results in a decrease of the FSR. As will be shown in the next section, standard volume gratings can only approach the narrow filtering ability of FPE but also have a number of benefits such as wider angle acceptance.

Diffraction by a Volume Bragg Grating

The final wavelength/angle selective element in Figure 1d is the volume grating. The volume grating is a special category of grating which deserves particular attention due to its ability to spectrally filter light with high resolution. The term volume Bragg grating (VBG) is often

applied to this type of grating due to the origin of its discovery by Sir William Bragg. In 1915 Bragg published a method for using x-ray diffraction from a crystal lattice to determine crystal structure [12]. This work demonstrated a strongly resonant diffraction condition exists when light is incident on a periodic structure such as a grating. When the thickness of the grating is made large enough, the diffraction orders will reduce to the point where there is only one order present which constitutes volume grating behavior [13].

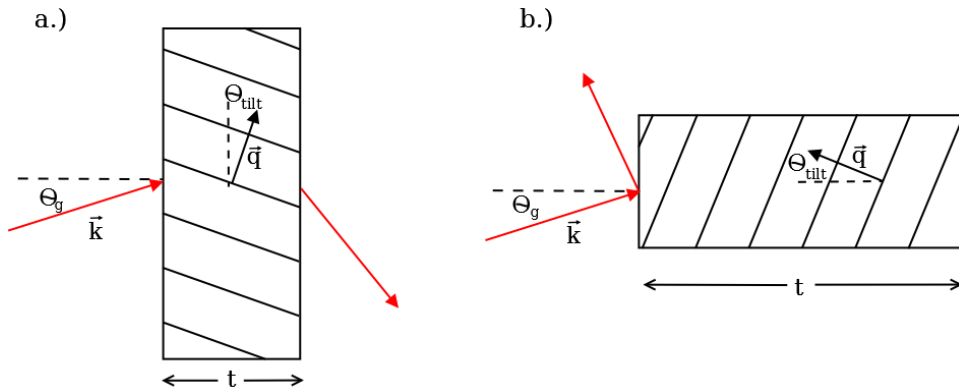


Figure 3: Read out geometries two types of VBGS. a.) shows the transmitting Bragg grating and b.) the reflecting Bragg grating along with basic designations of tilt.

A VBG can be used in two geometries shown in Figure 3. Both geometries include an arbitrary tilt angle θ_{tilt} for the grating vector q and light with wave vector k is incident at angle θ_g through a grating of thickness t . The transmission geometry for the Bragg grating (TBG), is shown in Figure 3a. Here light is incident at an angle greater than 45° with respect to the grating vector. Diffracted light is transmitted through the grating. The reflection geometry (RBG) is shown in Figure 3b. In this geometry light is incident at an angle less than 45° with respect to the grating vector and reflected back in the plane of the incident light. Typically, the grating vector is

orthogonal to one of the surface normals of the grating media or at a small angle. Therefore, corner gratings, those with light incident at near 45° to the grating vector, will not be considered here. The Bragg condition which defines resonant diffraction for these two types of gratings is given in Eq. 9 and Eq. 10.

$$\lambda_{TBG} = 2\Lambda \sin(\theta_g + \theta_{tilt}) \quad (9)$$

$$\lambda_{RBG} = 2\Lambda \cos(\theta_g + \theta_{tilt}) \quad (10)$$

Here, the Bragg condition is written in terms of λ the wavelength of the incident light, θ_g and θ_{tilt} which give the Bragg angle as defined in Figure 3 and Λ is the grating period. These angles are defined within the media and Snell's Law can be applied to determine the angle of incidence in air.

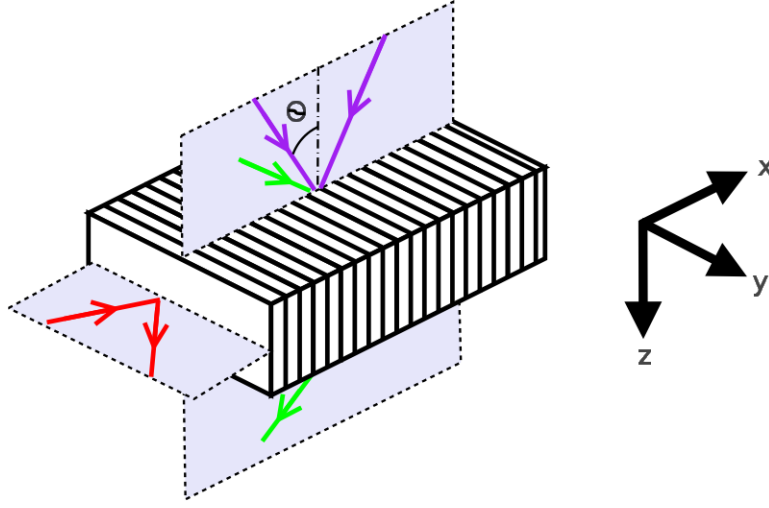


Figure 4: The off axis recording geometry for the recording of transmitting and reflecting Bragg gratings. The angle of incidence (θ) of the recording beams inside of the media determines the resonance properties of the final grating. Recording is shown in purple, transmitting Bragg grating readout in green and reflecting Bragg grating readout in red.

Before describing the mechanisms for diffraction produced by VBGs, the critical parameters, variable definitions, and coordinate conventions must be defined. Figure 4 shows an off axis recording geometry where two plane waves are incident inside the media at an angle $|\theta|$ with respect to the normal. This simple recording geometry is commonly used to create both transmitting and reflecting Bragg gratings. The readout of the grating as a transmitting Bragg grating (TBG) is shown in green and occurs in the same plane as the recording. The readout as a reflecting Bragg grating (RBG) is shown in red and occurs in a plane orthogonal to the recording plane. The recording parameters that dictate the final grating design are the writing wavelength in vacuum λ_w , the half angle of interference inside the glass θ_w , and the index of refraction at the writing wavelength n . These values can be used to give the grating period (Λ) which will, in turn, determine the resonant wavelength of the final grating. The grating has a wave vector which will be denoted using q in Eq. 11.

$$q = \frac{2\pi}{\Lambda} = \frac{4\pi n \sin \theta_w}{\lambda_w} \quad (11)$$

The direction of q is orthogonal to the angle bisector of the two writing beams. Figure 4 shows an unslanted grating. The angle bisector is parallel with the surface normal of the medium (z axis), therefore the grating vector is along the x axis. The bars in the grating correspond to a sinusoidal refractive index modulation (RIM) due to the interference of the two plane waves. This case is the simplest form of VBG. Additional complexity can result from the addition of tilt introduced between the surface normal and the grating vector, or by adding an apodization to the grating profile, i.e. structuring the intensity of the interference pattern as a function of x and/or y . The uniform, unslanted VBG will be discussed as it is the simplest case and provides for basic understanding of the filtering properties of a VBG. A discussion of modeling Bragg gratings with non-uniform profiles will occur in a later section.

Coupled Wave Theory to Describe VBGs

The predominant model for mathematically describing Bragg gratings was formulated by Herwig Kogelnik in 1969. Kogelnik's work using coupled wave theory (CWT) to describe diffraction from VBGs is widely used in modeling the spectral and angular characteristics of these elements [14]. A multitude of other methods for modeling grating spectra exist with varying degrees of precision [15-17]. The CWT approach is often preferred due to its relative speed and simplicity. The nature of the CWT method is to calculate the sum total amplitude and phase of the forward

and backward propagating waves as they pass through each part of the VBG. A full derivation of this method is covered in many texts [14, 18, 19] and only the end results and implications of this methodology will be presented.

The solutions to the volume hologram, using CWT in one dimension, require the definition of two coupled electro-magnetic waves representing the diffracted and transmitted waves. These electro-magnetic waves are made to satisfy the scalar wave equation with the assumption that the second derivatives in the wave equation are negligible. With proper boundary conditions defined, and a reordering of terms, analytical solutions are possible for several types of gratings including TBGs and RBGs with slant angles and losses. The results for the lossless dielectric gratings are shown below. The coefficients ν and ξ represent the dimensionless coupling and detuning parameters.

$$\nu = \frac{t \pi n_1}{\lambda_0 \cos(\theta_g - \theta_{tilt})} \quad (12)$$

$$\xi = \frac{(\lambda - \lambda_0) 2\pi n_0 t}{\lambda_0^2} \quad (13)$$

$$DE_{TBG} = \frac{\nu^2}{\xi^2 + \nu^2} \sin^2 \sqrt{\nu^2 + \xi^2} \quad (14)$$

$$R_{RBG} = \frac{\nu^2 \tanh^2 \sqrt{\nu^2 - \xi^2}}{\nu^2 - \xi^2 + \xi^2 \tanh^2 \sqrt{\nu^2 - \xi^2}} \quad (15)$$

The variables θ_g and θ_{tilt} represent the angle of the incident light inside the grating and the tilt angle of the grating lines. Both angles are defined with respect to the incident surface normal. Variable t represents the thickness of the grating, λ_0 is the Bragg wavelength, and n_I is the amplitude of the sinusoidal refractive index modulation. Using typical values that will be encountered in this dissertation for the coupling and detuning parameters yields the representative spectral and angular responses shown in Figure 5, Figure 6, Figure 7 and Figure 8.

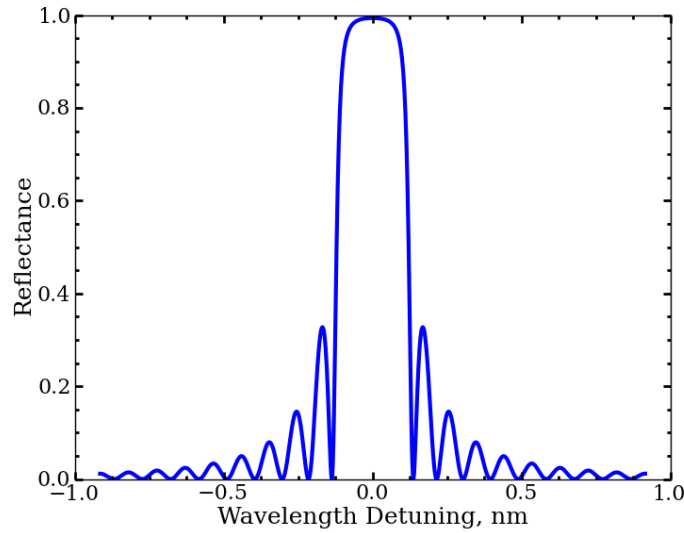


Figure 5: The spectral response of an RBG with a period of 360 nm, thickness of 4.0 mm and RIM of 270 ppm to light incident at 10° and detuned from a wavelength of 1064 nm.

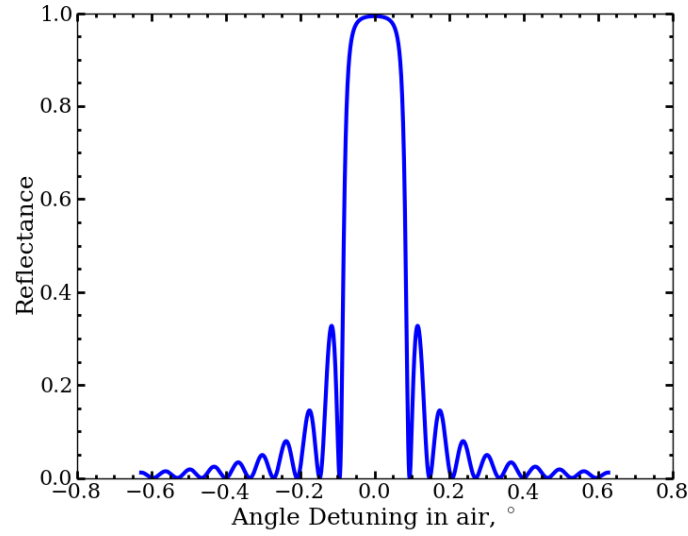


Figure 6: The angle response of an RBG with a period of 360 nm, thickness of 4.0 mm and RIM of 270 ppm to light at 1064 nm wavelength and detuned from an angle of incidence of 10° .

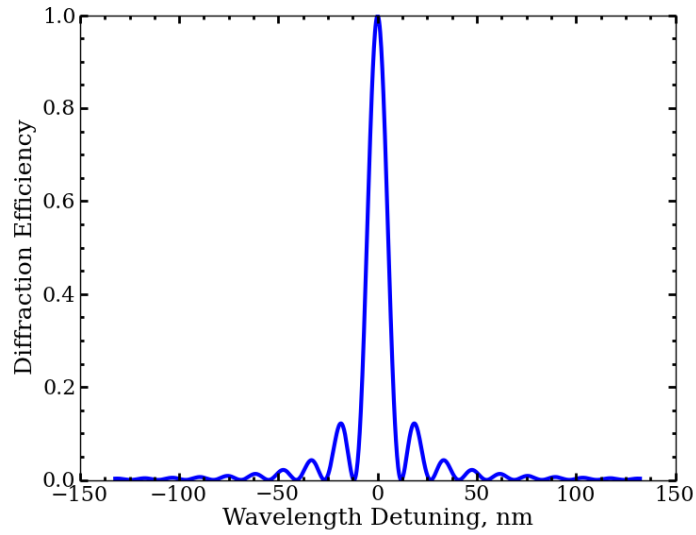


Figure 7: The spectral response of a TBG with a period of 3 μm , thickness of 2.0 mm and RIM of 270 ppm to light incident at 10° and detuned from a wavelength of 1064 nm.

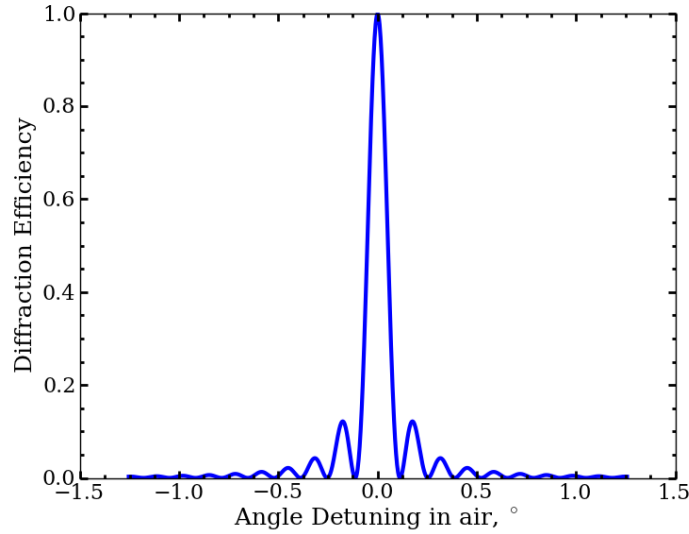


Figure 8: The angle response of a TBG with a period of 3 μm , thickness of 2.0 mm and RIM of 270 ppm to light at 1064 nm wavelength and detuned from an angle of incidence of 10° .

A note on nomenclature is in order at this point. When speaking of measurements of gratings, the values for angle are determined as the angle of incidence (AOI) with respect to the surface normal in air. The equations relating to Bragg incidence use angles and wavelengths within the media in order to simplify the appearance of the equations. For design and modeling of VBGs, the more physical values of AOI and wavelength in air have been used, so that all values presented here will be in air rather than within the media, unless otherwise specified. The measure of grating efficiency is given in terms relative efficiency. Relative efficiency is measured by normalizing the irradiance of the diffracted light to the transmitted light. This relative measurement differs from absolute efficiency, which is a measure of the diffracted irradiance normalized by the incident irradiance, in that it removes the contribution of losses that occur within the medium. In understanding the strength of a grating it is important to

characterize the losses separately from the actual grating efficiency. The use of the term diffraction efficiency (DE) refers to the exiting diffracted irradiance normalized to the total of the exiting diffracted and exiting transmitted irradiance. In the use of the terms transmittance and reflectance, the amount of irradiance is normalized to the light which is transmitted through the device far out of the Bragg resonance and, again does not include losses which occur in the media. These terms are distinct from transmissivity and reflectivity which relate to measurements of the electric field values. TBGs are always characterized by their diffraction efficiency and RBGs are characterized by either their transmittance or reflectance. The peak DE for TBGs or reflectance for RBGs occurs at a detuning of zero such that the input parameter is the dimensionless coupling parameter ν , which will be referred to as the grating strength following [19]. These peak values can be calculated using the grating strength and Eq. 16 and 17.

$$DE_{max} = \sin^2 \nu \quad (16)$$

$$R_{max} = \tanh^2 \nu \quad (17)$$

The spectral widths for the two types of gratings can also be calculated from Eq. 14 and 15 by solving for locations where the efficiency drops to a predefined value. The most commonly used metric is the full width at half maximum (FWHM). The rules of thumb for the FWHM spectral selectivity for a grating with approximately 10% - 70% efficiency are shown in Eq. 18 and 19. The tangent dependence of the TBG spectral selectivity makes it less useful than the RBG for achieving narrow band filtering. Conversely, TBGs are more common as angular selective devices. Since grating period determines the resonant wavelength, the grating thickness t is the

most critical factor in determining the wavelength selectivity of an RBG. An example design curve for an RBG is shown in Figure 9 showing that increased thickness leads to a decreased bandwidth for a fixed efficiency. In order to produce very narrowband filters, very thick gratings are necessary and excellent homogeneity is required of the material and the holographic recording. Therefore, achieving ultra-narrowband filtering using RBGs is limited by practical factors related to the recording of the hologram and properties of the recording material. RBGs with bandwidths of down to 20 pm with rejection ratios of 30 dB have been demonstrated using photosensitive glass [20]. Methods for decreasing the bandwidth of VBG filters beyond their basic capabilities will be presented in the subsequent sections.

$$\Delta\lambda_{TBG} \approx 0.9 \frac{\lambda \Lambda}{t \tan \theta_g} \quad (18)$$

$$\Delta\lambda_{RBG} \approx 1.1 \frac{\lambda \Lambda}{t} \quad (19)$$

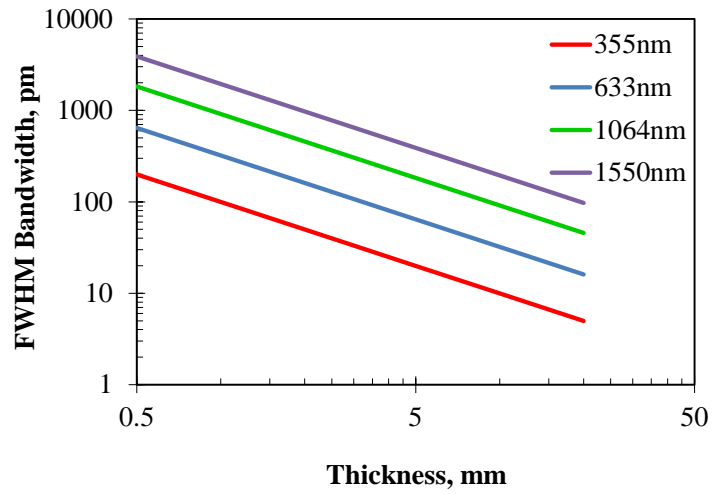


Figure 9: The design curve for the spectral selectivity (FWHM) of a reflecting Bragg grating with efficiency of 99% at a number of common laser wavelengths.

Now that the basic operation of VBGs relating to filtering has been defined it is important to understand what thickness (and therefore filtering selectivity) and efficiencies are possible. This depends primarily on the selection of recording material. A brief overview of some of the properties of commonly used holographic recording materials that can be used to create VBGs will follow.

Recording Materials for VBGs

The process for creating a VBG utilizes a photosensitive material to induce a sinusoidal modulation of refractive index through photo-exposure. Material selection varies based on application and the ideal holographic material has been covered widely [21, 22]. Essentially any

photosensitive material with the appropriate spatial resolution can be used as a holographic recording material. As such, a wide range of popular materials exist. The various strengths and weaknesses of each material make them well suited for different applications. To provide a suitable reference for discussions of the material of choice for this dissertation, some of the features of the most commonly used recording materials will be discussed.

The critical parameters that determine the holographic performance of a material are the spatial frequency response, dynamic range and photosensitivity. The material's physical dimensions, mechanical properties, wavelength sensitivity, and general development are also very important practical considerations. The frequency response is a measure of the feature size that the material can record and dictates what types of Bragg conditions can be achieved. In the most general form, frequency response is characterized by a modulation transfer function, which is a curve showing the visibility of sine waves of varying frequencies. Typically only a single frequency value is given as the frequency response where the modulation begins to drop, or where modulation is reduced by 3 dB. Values are often quoted as lines/mm, line pairs/mm, or the period of the sinusoid. Here all values of frequency response will be converted to the period that can be recorded as it relates most directly to the resonant wavelength of the grating and a low grating period (feature size) limit is associated with a better frequency response.

The dynamic range is a characterization of how much refractive index change can be achieved in a material. This will affect the required thickness of the device for high efficiency and the number of holograms that can be multiplexed. Values will often be quoted in terms of the

refractive index modulation (RIM) which is half of the total change in refractive index and is unitless. Small values of refractive index modulation will be given as parts per million (ppm). The photosensitivity of any type of material can vary by orders of magnitude and are often quoted using different metrics. Often the metric is the photo-dosage required to achieve 100% efficiency (or frequently 1% in the case of photo-refractive crystals) such that a highly sensitive material is characterized by a low dosage number [21]. Other metrics use essentially the inverse of this value so that a high value indicates a more sensitive value. Ultimately these metrics are hard to compare between materials due to efficiency also being affected by the particular device thickness, geometry and Bragg condition. Therefore, these values for photosensitivity are quoted loosely and are to give an idea of the relative dosage required for a typical holographic recording.

The physical dimensions that can be achieved in a particular medium affect the aperture size as well as the spectral selectivity of the device, assuming that there is enough dynamic range in the material for a particular device thickness. Physical parameters of materials are often related to damage thresholds and environmental stability. The wavelength sensitivity is important for determining the source for the recording setup and can have an effect on the minimum achievable period. Some materials have the ability to be sensitized at a variety of wavelengths which is very important for recording aberration free color holograms. Finally, development considerations include how the material is processed after recording. Most materials require some sort of development or bleaching and can also require steps to change the material thickness or otherwise make the hologram ready for its final application. Since many of these

parameters that will be discussed may not be directly comparable between materials, the purpose of this comparison is to give a general overview and discuss the relative order of magnitude of each metric.

One of the earliest holographic materials to be utilized was the silver halide emulsion. This is essentially a volume manifestation of a traditional photo-film and was used by Gabor in his first hologram [23]. A photosensitive silver halide is suspended in an emulsion such as a gelatin. The grain size of this film is much smaller than a traditional photo-film and dictates the frequency response of a particular emulsion. The grating periods that can be achieved can be as small as 0.4 μm . The grain size is also a contributing factor to scattering during reconstruction and recording and can create noise gratings which are holograms of the scattering elements. The films can be sensitized to a variety of different wavelengths for recording full color visible holograms. The sensitivity is around 1-10 $\mu\text{J}/\text{cm}^2$ making silver halide emulsions extremely sensitive and allowing rapid exposure times. The typical thicknesses are on the order of tens of microns and require a wet chemical development process similar to that of traditional photographs in order to develop the latent image. Recently, the refractive index change has been reported as high as 0.07 to give over 90% efficiency in a reflection Bragg grating [24]. Though such high efficiencies have been difficult to achieve typically and obtaining 100% efficiencies is not possible. Due to the high scattering and relatively low efficiencies, this material is better suited for display holograms. Low damage thresholds due to high absorption and the broad spectral selectivity due to the small typical thicknesses do not make silver halide emulsions suitable for laser system applications.

Dichromated gelatin is phase hologram recording material that has found great success in both research and commercial applications. It was first used by Shankoff in 1968 for recording holograms [25]. The material consists of photosensitive ammonium dichromate suspended in gelatin. In regions of photo-exposure, the hardness and solubility increase. This can be processed by removing the soft regions to create a relief grating or by a wetting process to create a phase hologram [26]. The photo-sensitivity is lower compared to silver halide emulsions at 0.1-1 J/cm² and intrinsically occurs in the UV-green regions of the spectrum, though it can be sensitized using dyes to other wavelengths [27]. The primary benefits of this material include low scattering losses, small feature sizes of below 0.4 μm , and a uniform frequency response for other periods making it useful for multiplexed elements containing many different periods. The typical thicknesses are tens of microns with very high dynamic range of around 0.08 allowing dichromated gelatin holograms to achieve efficiencies of 100%, though the spectral and angular selectivity is very wide due to the small thicknesses. The primary drawback of this material is the environmental instability. The gelatin is very sensitive to humidity which induces swelling and a drop in efficiency. Therefore extensive post processing is required which usually involves baking to remove moisture and hermetically sealing the hologram between glass plates. So while the material is an excellent choice for multiplexing high efficiency gratings, the sensitivity of the device to environment make it unsuitable for many applications.

Photopolymers consisting of a photo-polymerizable monomer suspended in a polymer are commonly used for volume grating production in commercial applications and are a strong

candidate for holographic data storage [28]. Index change is achieved by photo-exposure causing some of the monomer to polymerize. Due to the gradient of monomer concentrations, the monomers then diffuse from regions of low incident irradiance to regions of high irradiance [29]. A bleaching process of exposure to uniform light converts the rest of the monomer to polymer resulting in a refractive index change. This has the advantage of a relatively simple development process making it suitable for applications that require in situ processing. Due to the complex mechanism for refractive index change which relies on a diffusion process, the development kinetics vary for gratings with different spatial frequencies. In particular this material has a poor low frequency response when the feature size is larger than the diffusion length. The thickness of the polymer can range from several microns up to a millimeter and refractive index change up to 0.03 can be achieved allowing for efficiencies of 100% [28, 30, 31]. The sensitivity of this material is typically around 10 mJ/cm² in the UV/blue portion of the spectrum. The drawback of this material for use in laser systems is the low thermal stability and therefore low damage thresholds [32, 33]. For use in high power systems, inorganic compounds provide the best tolerance to laser damage.

The photorefractive crystal as a volume holographic media is a promising candidate for multiplexing, data storage, and holographic processing. Volume holography was first shown using this material in 1968 by Chen in Lithium Niobate [34]. Holograms are induced in photorefractive crystals by illuminating the crystal with an interference pattern and electrons are excited in the bright regions and some transport mechanism (thermal diffusion, drift from the external electric field, or photogalvanic effect) redistributes them. This forms a spatial electric

field pattern that is linearly translated into a refractive index change when the electron transport mechanism is primarily due to drift from the applied electric field. The gradient of the intensity distribution can also be recorded when no external electric field is applied and diffusion is the transport mechanism. The refractive index modulation is strictly speaking an anisotropy pattern which makes these holograms particularly sensitive to polarizations. Since the hologram formation is effectively instantaneous and doesn't rely on the development of a latent image, there are a number of interesting effects that can occur during recording. One of these effects is the ability to directly monitor the change of diffraction efficiency by probing the device with a different wavelength so that a desired efficiency can be achieved [35]. Also the self-diffraction that occurs during recording can be used to monitor any shifting of the interference pattern with respect to the current grating structure, which allows for a convenient way to actively stabilize a recording setup [36]. Another feature of this material that is useful for applications in data storage and optical processing, is the ability to erase and rewrite holograms. Common photorefractives include Lithium Niobate (LiNbO_3) lithium tantalite (LiTaO_3), barium titanate (BaTiO_3), and strontium barium niobate (SBN) [37]. The properties of photorefractive crystals depend strongly on material selection and vary widely with application. Typically thicknesses are on the order of millimeters, with induced RIM ranging from 10-500 ppm and sensitivities in the range of $0.001\text{-}1 \text{ mJ/cm}^2$ at visible wavelengths [38]. The primary drawback of volume holograms in photorefractive crystals is eventual erasure of the stored holograms. This erasure occurs during readout with a uniform beam, though fixing techniques have been developed to compensate for this effect [39]. Despite extensive efforts in hologram fixing, electron migration

eventually causes a degradation of the grating pattern and the storage time of holograms remains a primary concern for fabrication of permanent devices in photorefractive crystals [40].

Photosensitive fibers represent a slightly different class of volume Bragg grating element. Due to fibers being essentially one dimensional structures, the holograms recorded in fibers are primarily reflecting type volume Bragg gratings. This puts fiber Bragg gratings (FBGs) in a unique classification compared to the previously mentioned materials, but many of the properties and applications of FBGs have a direct relation to the multiplexed VBGs that will be discussed in later sections. In particular, FBGs are unique because they can use thicknesses on the order of centimeters compared to other the other materials that have thicknesses on the order of tens of microns to a few millimeters. These are truly thick structures and are common components in telecommunications applications as well as fiber laser development. The refractive index modulation can be induced in photo-sensitive germanium doped silicate fibers using UV radiation or by using pulsed radiation in the near IR for non-doped fibers. Refractive index modulation is achieved in the germanosilicate glasses by material changes that occur at UV absorbing oxygen deficiency centers, though the actual mechanism is still actively studied, and by producing localized damage in the case of high-speed pulsed recording [41]. The first such demonstration of a fiber Bragg grating by Hill produced a reflection grating at 515 nm, corresponding to approximately 0.3 μm period which is indicative of the high frequency response of the material [42]. Since the typical thickness of these gratings is very long, only a small amount of index modulation is necessary for many applications. In the special case of long period gratings, which have an order of magnitude longer periods, much higher RIM is

necessary. Subsequently, the RIM in fiber gratings ranges from as low as 10 ppm in UV exposed fibers, up to 2000 ppm for photosensitive fibers that are hydrogen loaded to increase sensitivity, to as much as 0.035 for gratings recorded by pulsed writing in the IR [43]. The photo-sensitivity of fibers is extremely low and rarely are the details for determining photo-dosage presented in the literature, but typical values for recording parameters yield sensitivity in the 10-100 J/cm² range. Fortunately the actual hologram volume is orders of magnitude lower than for other holographic materials that have been discussed and this sensitivity is not an obstacle for efficient grating production. The primary strength of fiber Bragg gratings is the automatic alignment of the incident light to the grating due to the confinement of the waveguiding structure. This restriction makes them extremely convenient for integrating into an all fiber system, but also limits many of the interesting features that can be designed into free space VBGs such as angular selectivity. The ability to harness the many benefits of multiplexing in free space optics combined with the excellent filtering capabilities of fiber gratings can be realized by using a bulk photo-sensitive glass as a holographic material.

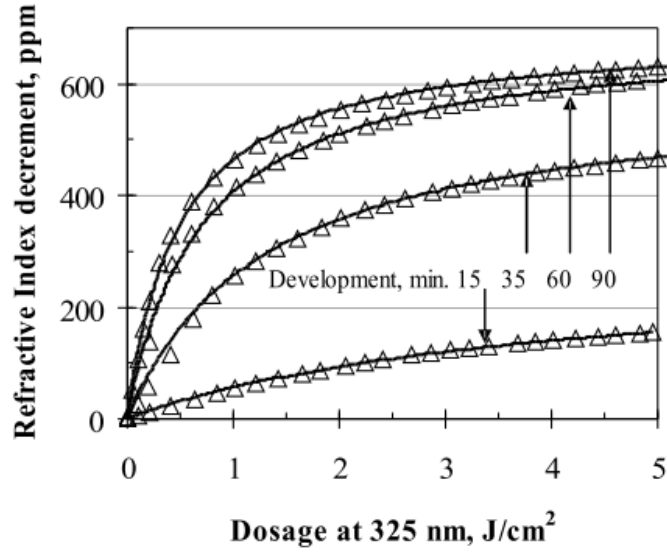


Figure 10: The change in refractive index in exposed PTR depends on the applied photo-dosage as well as the development time.

A holographic recording media that meets these criteria and has been used in recent years with great success is photo-thermo-refractive (PTR) glass. PTR is a photosensitive silicate glass which can be used for the recording of volume phase holograms with high efficiencies and low absorption losses [44–46]. The glass matrix is $\text{Na}_2\text{O-ZnO-Al}_2\text{O}_3\text{-SiO}_2$ glass doped with silver, cerium, and fluorine and is photosensitive to light in the near UV. Refractive index change is achieved through a process of photo-exposure, followed by a thermal development. During photo-exposure, the Ce^{3+} ion absorbs a photon and releases an electron which recombines with silver ions and atomic silver is formed in the region of photo-exposure. Thermal development causes agglomeration of silver atoms to colloidal particles that serve as nucleation centers for precipitation of crystalline phase sodium fluoride in the photo-exposed regions. This crystalline phase precipitation results in a localized stress which induces refractive index change in the

photo-exposed region. The refractive index modulation that is achieved in PTR glass differs from other media in that it depends on more than just the photo-dosage. The thermal development after recording plays a strong role in the RIM. Because of this fundamental difference the sensitivity, as calculated for the other materials, holds little meaning. That said, the typical dosage for recording is around 1 J/cm^2 . In order to achieve a particular RIM after exposure, the baking procedure is designed to give the desired results. The relation between the induced refractive index change and the exposure and development is shown in Figure 10. Many combinations of dosage and development are possible to obtain a desired change in refractive index within the linear portions of these curves. After development a thermally stable, permanent refractive index change is induced in the PTR. The low absorption level and the thermal stability of the glass matrix make this material extremely well suited for high power laser systems or for use in harsh environments. For recording of permanent gratings, this material is far superior to the organic materials or photorefractive crystals. Due to the hologram being recorded into the volume of the material, the grating is extremely robust and can be handled without special precautions. Damage to the surface can easily be polished away unlike an extremely fragile surface grating. The level of refractive index modulation can range from 20 ppm to 1000 ppm. This dynamic range is similar to that typically encountered in photosensitive fibers and requires long interaction lengths. The high optical homogeneity of PTR allows thicknesses ranging from 1 mm to 100 mm so that highly efficient gratings ($>99\%$) can easily be recorded using this level of dynamic range. These thicknesses are on the same order as those for FBGs, but since PTR gratings are recorded as bulk optical devices, many of the interesting features of free space VBGs can still be exploited in such a material. The ability to record gratings with large

thicknesses and low refractive index modulation means that extremely narrow spectral and angular filters can be achieved according to Eq. 18 and 19. For high power systems, long interaction lengths, and apertures of several millimeters PTR glass is an exceptional holographic recording material.

Recording Methods for VBGs

While thin gratings can be etched as surface reliefs, VBGs require the grating structure to exist throughout the volume of the recording media. This can be done in three common ways: point by point inscription with a short pulse laser, phase mask to create a sinusoidal interference pattern, or a holographic recording [13, 47, 48]. While phase mask and point by point recording techniques are typically applied to VBGs recorded in fiber (FBGs), holographic recording remains the most common technique for creating Bragg gratings in bulk recording media such as PTR glass. Direct writing is extremely flexible and can generate arbitrary grating patterns, but is typically a slow process that is used for long period gratings [49]. The phase mask is very robust recording device that is commonly used to fabricate fiber Bragg gratings (FBGs) but lacks versatility in that it can only transfer a particular grating period. The efficiency of the phase mask is also limited to about 80% due to diffraction into the zeroth and higher diffraction orders [49]. Holographic recording is an excellent middle ground where low loss, high quality fringes can be recorded with configurable grating periods and tilts. In designing custom volume gratings for laser systems, holographic recording is preferred.

Within the sub-category of holographic recording there are a number of types of recording setups that can be used and brief review of these systems is in order. In following the progression of holography, the first setup that was demonstrated is the Gabor hologram, also called an inline hologram [23]. The original proposed setup is shown in Figure 11a. This is an extremely simple holographic setup and variants are used to record reflecting Bragg gratings that are resonant at the recording wavelength. Another approach is the off-axis recording geometry that was developed by Leith to separate the reference beam from the reconstructed wavefront [50]. The original setup is shown in Figure 11b but in practice, the actual interference angle is usually controlled by steering mirrors. Both methods were demonstrated using some object to distort the phase of the object beam and interfere this object beam with a planar reference beam to generate a visible hologram. For producing the uniform phase gratings that will be discussed here, no object will be used. This will create what is essentially a holographic recording of a planar laser beam.

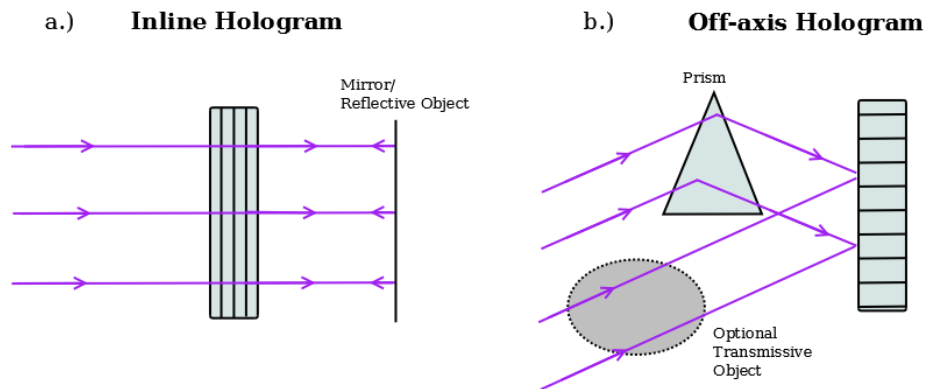


Figure 11: Two methods for producing reflection and transmission holograms.

The details of the recording setup used for the remainder of this work are shown in Figure 12. The entire set up is on a vibration isolating table and enclosed by two acrylic boxes to damp temperature fluctuations and air currents. A helium cadmium laser at 325 nm and approximately 40 mW of optical power is used as the recording source. The shutter system allows the exposure to be controlled remotely so that the operator does not disturb the system prior to recording. Two expanders are used to generate appropriate beam sizes for the beam shaping and for the final exposure. Beam shaping is accomplished using a pi-shaper by AdlOptica to convert a Gaussian input beam to a flat top profile. The final expanded beam is approximately 30 mm in diameter.

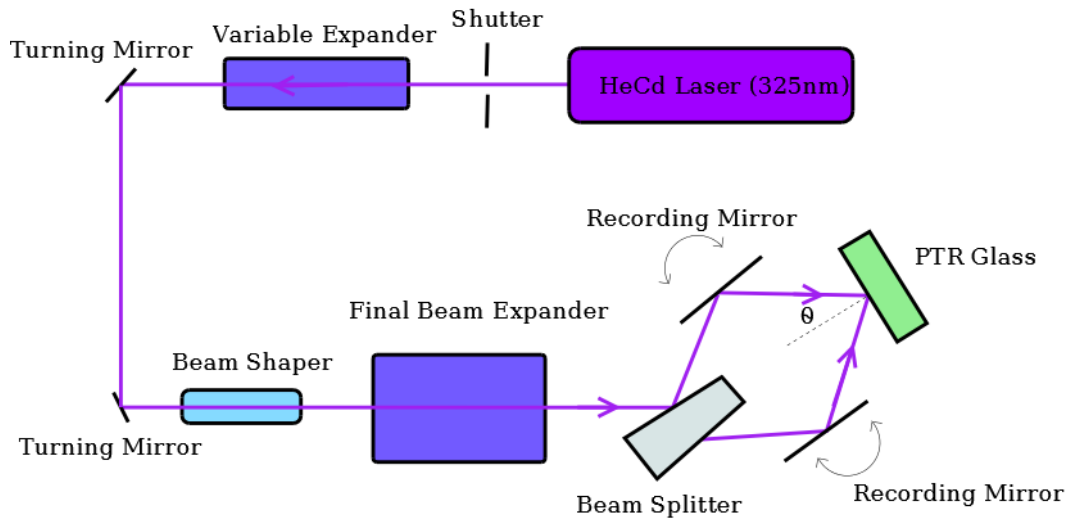


Figure 12: Recording setup for holographic exposure for producing VBGs in PTR glass.

After the shaping and expansion of the beam, the light is split into two paths by a beamsplitter and recombined by two mirrors at the recording plane. The mirrors are used to control the angle of incidence and therefore the grating period. The recording media is placed on a two axis stage with controls for tip and tilt of the sample so that tilted gratings can be recorded. The stages are

motorized so that gratings with precise and repeatable periods and tilts can be recorded. This repeatability is extremely important when recording gratings with tolerances of the resonant wavelength on the order of tens of picometers. Motorized control is also critical for producing multiplexed gratings since the relations between each recorded grating determines the interplay, or lack thereof, between each grating. Using this setup VBGs can be recorded with precision of the grating period within 20 pm and tilt angle better than 0.01° . The high level of precision and repeatability of the recording setup allows grating designs to be finely tuned and meet the tight tolerances required for laser systems development.

Multiplexed Gratings

The concept of recording many gratings within a recording media finds applications in data storage, beam combining, wavelength multiplexing or demultiplexing devices, optical logic, and spectral sensors [51–55]. Multiplexing discrete gratings is fundamentally a transitional technology from single gratings to holographic imaging. Two distinct classes of multiplexed gratings can be identified. In the first, multiple independent gratings are recorded. Each grating serves some purpose and the function remains unchanged by the inclusion of other gratings into the device. Such a device serves the same goal as a similar system using discrete gratings, but in a more compact geometry. Cross-talk between the holograms is undesirable for these types of gratings. Examples where these kinds of devices find application are spectral beam combining systems and holographic data storage. The second type of multiplexed grating is the interdependent grating. In this situation each grating only functions properly due to its interaction

and coupling to the other grating structures. Examples are moiré gratings, coherent beam combining systems, and to a certain extent holographic images. The various applications that benefit from multiplexed gratings of either type will be discussed in this section.

For communication systems, wavelength multiplexing and demultiplexing devices are in high demand. By encoding data on several wavelength channels, data rates can be increased significantly and devices for addressing each channel individually are critical to realizing such a scheme. Various devices exist for achieving these results, including angularly dispersive devices, interferometer systems, and arrayed waveguides. Angle dispersion methods are convenient in that all splitting and combining is done with a single device, but are generally only efficient at demultiplexing operations in terms of insertion loss [56]. The other systems rely strongly on consistent path lengths and therefore are extremely sensitive to vibrations and thermal changes. One of the most robust ways to address individual channels is using a series of FBGs and optical circulators. This same sort of filtering can be realized in a single free-space optical element with a multiplexed grating. Such a grating can be designed to redirect each wavelength channel into discrete spatial locations with high efficiency so that they can be addressed individually. These systems have been demonstrated in photorefractive crystals, emulsions and photopolymers [57-59]. Thermally and temporally stable materials such as PTR glass are excellent candidates for recording devices of this nature. Therefore, demonstrating multiple channel splitting of closely spaced wavelength channels can be very useful for this field.

A related use of multiplexed gratings is in shaping the spectral amplitude and phase of optical signals in fiber. This is useful in dispersion compensation for long optical networks as well as for high speed photonics. Such multiplexed gratings are of the interdependent type where the interplay of each multiplexed grating gives some final desired result. Examples of spectral shaping systems include dispersion compensation by recording many sinusoids such that a final desired profile is achieved in the grating as shown by Painchaud [60]. This can also be accomplished by moving/phase shifting the interference pattern which results in phase multiplexed FBGs [61]. The simplest variant of this type of grating is the moiré grating which contains two collinear Bragg gratings of slightly different period. This process can generate gratings with a very narrow transmission peak or perform grating apodization to remove unwanted side-lobes in the reflection spectrum [62]. These types of filters that operate in transmission are very useful for fiber applications because they eliminate the need for an optical circulator.

Beam combining of high power lasers is greatly desired in applications for manufacturing due to limitations of the output power of a single laser from the onset of non-linear effects. For applications that require delivery of combined beams at long range, it is necessary to ensure both diffraction limited beam quality and high radiance (defined as power divided by the product of the solid angle in the far field and the beam's M^2) [63]. When the power required at a target exceeds the levels available from a single laser system meeting the beam quality criteria, it is necessary to combine several lower power diffraction limited laser sources. Multiplexed diffraction gratings can be used to achieve these goals with a single optic. The two main ways of

achieving combining are Spectral Beam Combining (SBC) and Coherent Beam Combining (CBC). In SBC, multiple incoherent beams are superimposed such that they propagate to the same far field location. Beams of slightly different wavelengths are used such that no detrimental interference effects occur, but are closely spaced so as to obtain a high spectral radiance. Maintaining a narrow bandwidth of the combined beam is desirable for applications where all beams must be within a particular gain bandwidth for use in a laser system or within atmospheric transparency window for propagation to long range targets. While this is fundamentally the same principle as wavelength division multiplexing, the practical considerations of SBC at high power are focused on thermal management and are vastly different than for low power communication systems. Most demonstrations of SBC utilize a surface diffraction grating in the Littrow condition [64-66]. Fundamentally these geometries can be replaced by a high efficiency multiplexed volume Bragg grating to achieve the same results and recent experiments demonstrating combining using VBGs in PTR have shown promising results [67]. In CBC, coherent beams are combined such that their relative phases interfere constructively. Matching the phase of each combined beam can be achieved passively or by incorporating an active phase control with feedback [68-71]. The use of passive CBC eliminates the need for phase detection and high speed electronics and has been recently demonstrated using multiplexed VBGs in PTR [72, 73]. The low absorption losses and high efficiency of VBGs recorded in PTR glass, make both spectral and coherent beam combining attractive applications for the technology discussed in this dissertation.

A whole host of other applications are also achieved by multiplexing Bragg gratings. Multi-wavelength sensors and spatial spectral imaging have been demonstrated and are useful in spectroscopic measurements and spectral imaging [74, 75]. Optical computing is also a field that benefits from multiplexing of gratings, ranging from optical processing operations to optical data storage. In particular holographic data storage relies heavily on the ability to encode data on multiplexed holograms. This technology has yet to find commercial success, but a great deal of research has been conducted towards this goal [51, 76, 77]. In holographic data storage, efficient multiplexing of gratings dictates the storage density that is achievable and therefore multiplexing dynamics are incredibly important to this field.

In each of these applications, complex grating behavior is at play. Cross coupling (alternatively called cross-talk) between the individual grating responses may or may not be desirable for a given application. Additionally, the formation of the individual gratings and their interplay during the recording and development stages can have a significant effect on multiplexed gratings. To address these issues, there are numerous publications that cover the dynamics of how multiplexed gratings interact with each other [78, 79]. Many of these studies deal with a specific device design or address the grating formation in a particular recording material. So while the results of the referenced publications are not necessarily applicable to everything that will be discussed in this work, general conclusions and methods from these studies provide useful information. For instance in multiplexed gratings where coupling is desired, such as in a coherent beam combining grating or logical AND gate grating proposed by Kowarschik [54], the importance of generating equal RIM in the individual recordings is shown with several specific

examples. In such gratings, calculations have shown that the lower frequency grating will have a higher diffraction efficiency [80]. For gratings where coupling is unwanted, the interplay of the individual gratings is of primary interest. In this case, the necessary detuning separation of two Bragg gratings such that they do not cross couple has been shown to occur when the first zeros of each grating's detuning response overlap [80]. When grating responses are separated by more than this criterion, an extremely detailed analysis of multiplexed gratings shows that essentially no high order diffraction occurs [81]. When multiplexing is achieved by simultaneous recording as opposed to sequential recording, unwanted diffraction gratings are formed due to crosstalk between the numerous recording beams. So when $n/2$ holograms are desired, n recording beams must be used, but this will generate $n(n-1)/2$ gratings. A middle ground can be achieved where no cross talk occurs but each recording develops quasi-simultaneously. This quasi-simultaneous recording occurs by interleaving the recording time of each different grating or it can be achieved by recording simultaneously using mutually incoherent or unpolarized recording beams [82]. These additions either come at greater complexity or are not scalable beyond two multiplexed gratings. Difficulties can also occur in sequential recordings when the previous recording causes some diffraction of the recording beams. These effects are most prevalent when recording at the same wavelength as reconstruction and only when a significant index modulation is induced before development. It is important to note that for multiplexing gratings in PTR glass, sequential recording is utilized but recording is always at a different wavelength than the designed operational wavelength. Another potential source of problems in sequential recordings is the combinational gratings which exist due to sum and differences of two grating wave vectors. Combinational gratings can produce measureable responses but only with specific

recording parameters and even then only demonstrating low efficiencies ($<1\%$) [83]. These results show that for a material such as PTR, sequential multiplexing of gratings is the most applicable type of recording and will not result in significant unwanted higher order diffraction.

This background information concludes the discussion of the state of the art in recording of volume Bragg gratings. Common dispersive and spectral filtering elements have been discussed and compared to volume gratings. The filtering that can be achieved with a volume grating and the theory relating to volume diffraction has been explained. The various recording materials, methods and applications for volume holography have been investigated. The use of PTR glass was shown to be an excellent candidate for a holographic recording material for multiplexed VBGs. The following sections will discuss advances that I contributed to the art of multiplexing volume Bragg gratings with applications in laser system development.

2 ADVANCES IN HOLOGRAPHIC RECORDING

The recording of high quality VBGs depends primarily on the recording media and the holographic setup. With access to a high performance media, such as PTR glass, the advancements in holographic recording are focused on improving and characterizing the holographic setup. For reference, the full setup is shown in Figure 12. Two sources of potential error in the recording of volume Bragg gratings were identified within the setup. The first was wavefront aberrations and the second was vibration and phase instability of the recording setup. The work done in addressing improvements of recording setup will be discussed in this section.

Aberrations of Recording Beams

The effect of aberrations in the recording beams on VBG quality was investigated by modeling contributions of different aberrations and by characterizing the recording setup. Aberrations are deviations of the phase front of a beam from an ideal phase front and are characterized by a set of coefficients. Primarily, the Zernike polynomial expansion of aberrations will be used since it is an ortho-normal set of polynomials that can be separated such that the effect of each aberration can be studied independently [84]. This polynomial expansion is also used frequently in commercial wavefront sensors (WFS), therefore the Zernike expansion is convenient for comparing theoretical calculations to measurements using a WFS.

A theoretical model of the effect of recording beam aberrations on hologram formation was lacking for thick media. Previous calculations only focused on a single plane of interference where perfect overlap of the recording beams occurs [85-87]. While this analysis was valid for thin gratings and fibers, for VBGs in PTR the depth of the recording is on the order of several millimeters (see the z axis of Figure 4) and perfect overlap cannot occur through this entire depth. Therefore a new and more complete model was necessary. This new model starts by considering the interference of an aberrated beam with a flipped and tilted version of itself as occurs in the setup of Figure 12. The interference can be written to include the effect of the aberrated wavefront using the standard two beam interference equation in Eq. 20, where I_1 is the irradiance of the incident beam and is assumed to be constant across the aperture, k is the wavenumber of the recording beam, θ is the angle of interference and d is a symmetric shift of the two beams that varies through the depth.

$$I(x, y, z) = 2I_1 \cdot [1 + \cos(2kx \sin \theta + \phi(x + d(z), y) - \phi(-x + d(z), y))] \quad (20)$$

The phase term ϕ is composed of the sum of the various orders of Zernike polynomials which are listed in Table 2. In these polynomials, the coordinates are normalized to the radius of the aperture of interest and therefore primed values denote a coordinate that is normalized to the radius of the recording beam aperture. The relative shift (d) of the two beams in the x direction varies through the depth of the medium (z). In the polynomials listed, $d(z)$ is explicitly written in terms of the z coordinate and the angle of interference within the PTR sample θ , such that $d(z) =$

$z \tan \theta$. The origin of these coordinates is at the center of the grating. The coefficients used in these polynomials are for peak-to-valley wavefront error. That is, the amplitude of a given wavefront aberration is specified by the difference between the maximum and minimum phase distortion across the aperture. The polynomials for RMSE wavefront are of the same form but use different coefficients. The phase term for each Zernike polynomial order are listed in Table 2 along with the associated aberration name.

Table 2: The wavefront profile for the various Zernike aberrations.

Zernike Polynomial	Aberration	$\varphi(x+d(z),y) - \varphi(-x+d(z),y)$
0	Piston	0
1	Tilt x	$2x'$
2	Tilt y	0
3	Defocus	$8x'z'\tan\theta$
4	0° Astigmatism	$4x'z'\tan\theta$
5	45° Astigmatism	$4x'y'$
6	Coma x	$2x'(9z'^2\tan^2\theta+3x'^2+3y'^2-2)$
7	Coma y	$12x'y'z'\tan\theta$
8	30° Trefoil	$2x'(3l'^2\tan^2\theta+x'^2-3y'^2)$
9	0° Trefoil	$12x'y'z'\tan\theta$
10	Spherical	$24x'z'\tan\theta(2z'^2\tan^2\theta+2x'^2+2y'^2-1)$

Inserting any combination of these wavefront profiles into the two beam interference pattern allows the local grating period and tilt throughout the entire volume of the recording material to be determined. With an understanding of how the local period and tilt of a grating is affected by aberrations, the spectral response of this type of grating can be determined for light incident at any point. In PTR VBGs, the effect of aberrations is most noticeable in RBGs due to the typically larger interaction volumes than those encountered when using TBGs. The spectral response of an RBG with light incident normal to the surface, is calculated by using a coupled wave theory-based transfer matrix approach that allows gratings with non-uniform parameters to be analyzed [88]. In this approach, thin slices of the grating along the x direction are assumed to satisfy the slowly varying envelope approximations (SVEA) and have uniform parameters within the slice. For each slice, a matrix is assigned and matrix multiplication allows the spectral response for the entire device to be calculated. Since the grating is non-uniform in the y and z directions as well, a summation of the spectral responses across a finite aperture defined by the readout beam is necessary to understand the full effect of aberrations on grating performance in real world applications.

An example of these calculations was carried out by Marc SeGall for a typical RBG that might be created in PTR to act as a spectrally selective output coupler in a laser system [89]. The x,y,z dimensions of the simulated sample is 20 mm x 25 mm x 10 mm. The ideal grating, recorded with unaberrated beams is designed to produce a resonant wavelength of 1064 nm with RIM of $n_I = 20$ ppm which, through the 20 mm thickness will result in a 68.5% reflection and a spectral width of 24 pm FWHM. This is a very narrowband grating with a relatively large thickness. Such

a device is extremely sensitive to shifts of Bragg wavelength because of the narrow spectral response and the large thickness will mean that even small aberrations can generate large wavefront distortions at the edges of the aperture. Therefore this device represent the most sensitive VBG with respect to aberrations that would be recorded in this setup. The simulations were completed for a Gaussian probe beam with a diameter of 5 mm incident on the grating along the x axis at three different points on the grating given by: (a) center using $y = z = 0 \text{ mm}$, (b) right using $y = 6.25 \text{ mm}$, $z = 0$, and (c) up using $y = 0$, $z = 2.5 \text{ mm}$. These simulations are shown in Figure 13 using one wave of each aberration. The aberrations in the top row correspond to those aberrations that do not have a chirp (i.e. a spatially dependent change in grating period) in the x direction and are therefore able to be calculated without using the transfer matrix step. The aberrations in the lower row required the full treatment of transfer matrix followed by summation of spectral responses over the probe beam aperture.

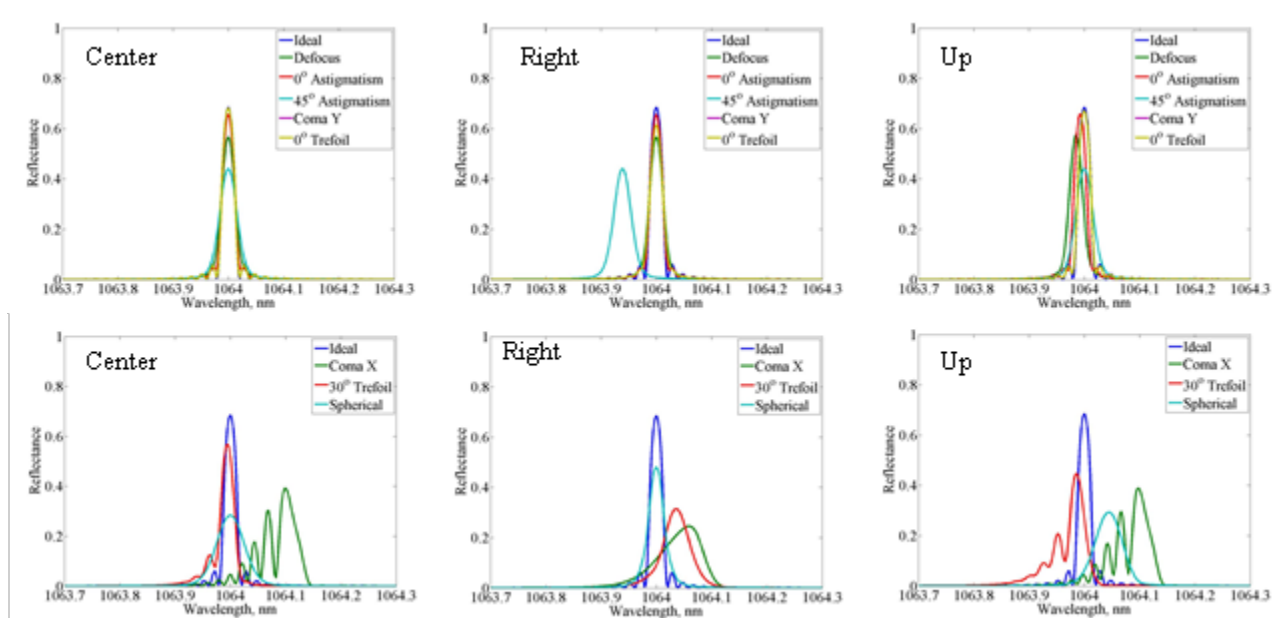


Figure 13: The deteriorated spectral response of an RBG recorded with a single wave of each Zernike aberration. Plots show various probe locations and the various rows show different subsets of the Zernike aberrations.

It is clear that aberrations can significantly deteriorate the spectral response of a typical RBG when present on the order of one wave. This is especially true for aberrations that induce chirp in the x direction such as Coma X, Spherical and 30° Trefoil where dramatic shifts and distortions of the spectrum occur at different probe locations. All other aberrations result primarily in decreases of efficiency and washing out of the side lobes. For typical laboratory systems, aberrations are much lower than one wave and only rarely approach half of a wave. These results are intended to clearly show the effect that a reasonably large aberration can have on performance and that the capability exists to model the effect of an arbitrary level of aberration.

From showing that aberrations in the recording beam can have a significant effect on RBGs, it was necessary to determine the magnitude of aberrations present in the recording system. Common methods for determining the aberrations present in a beam are to use a lateral shearing interferometer, or a split path interferometer such as a Michelson, Sagnac, or Mach-Zehnder. In each system the aberrated beam is being used as a reference for itself. Therefore, to obtain any interference fringes for analyses, the interfering beams must have at least some level of lateral shear or the reference and the object will always give perfect interference fringes. Analysis of interferograms with these setups can be done qualitatively by looking at the shape of the interferograms or analyzed numerically to obtain quantitative results. For the present discussion it is sufficient to look at the effects qualitatively. As this is a more traditional method of measuring aberrations, most literature uses the Seidel aberrations. Though the aberration names seem the same between the Zernike and Seidel, there is not a one to one correspondence, only a similarity the shape of the wavefront error. For this discussion, which only addresses simple first order approximations of aberration content, these similarities are sufficient.

$$W(x,y) = Spherical \cdot (x^2 + y^2)^2 + Coma \cdot y(x^2 + y^2) + Astigmatism \cdot (x^2 - y^2) + Focus(x^2 + y^2) + Tilt_y \cdot x + Tilt_x \cdot y + Piston \quad (21)$$

The Seidel wavefront expansion is given in Eq. 21 with the wavefront error W being defined using coefficients that represent contributions by each type of aberration across an aperture of normalized coordinates x and y . The interferogram produced by a shear plate can be simulated by the addition of $W(x, y)$ and $W(x-shear, y)$. Aberrations of either or both shearing surfaces

(characterized by an interferometer with a calibrated reference) can also be introduced into the simulation when an imperfect shear plate is used. Simulations of how a shear plate image looks were calculated using the Seidel equation for the various aberrations. The amount of shear that was used in the simulations was determined from the thickness of the shear plate that was used in the actual measurement which is approximately $1/3$ of the beam diameter. The results are shown in Figure 14 with the dimensions of each subplot being equal to the diameter to the beam. It is clear that defocus and astigmatism produce the same result; straight line fringes across the aperture and they are indistinguishable from the interference of two tilted wavefronts. This makes the lateral shear plate less than ideal for determining aberrations in a beam since it must use itself as a reference, but it is a simple and fast method for obtaining a rough estimate of the aberration content in a beam.

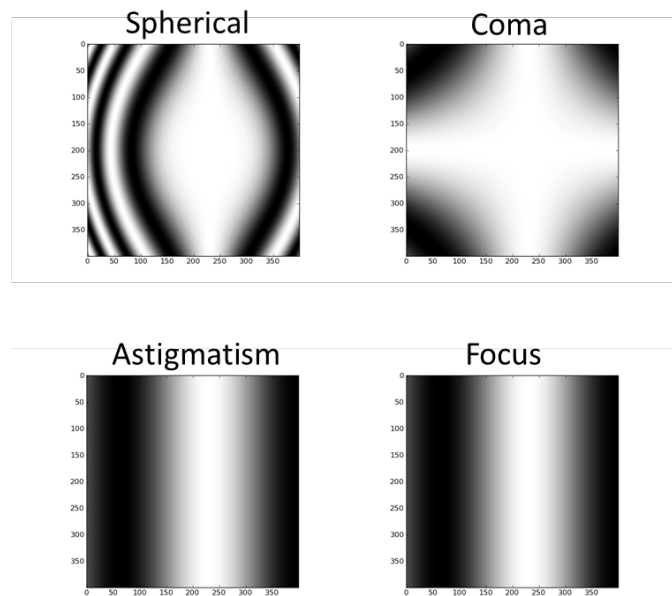


Figure 14: The appearance of the primary aberrations when viewed by a shear plate with a lateral shear of approximately $1/3$ of the beam radius.

The aberrations after the final beam expander from Figure 12 were characterized using a shear plate with 10 mm of lateral shear. The RMSE wavefront error induced by the shear plate is less than 0.025 waves of 633 nm light across the test aperture. The shear image is shown in Figure 15. A simulation trying to match the shape of this image is shown in Figure 16. This simulation suggests that approximately 40% of the wavefront distortion is caused by spherical aberration and either defocus or astigmatism with some coma. Again, this measurement only provides a slight idea of the aberrations present in the system but does prompt a more detailed investigation to ensure that high quality recordings are being achieved.

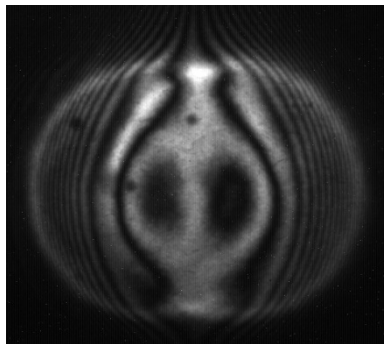


Figure 15: The shear plate image of the recording beam at the output of the beam condition portion of the holographic recording setup.

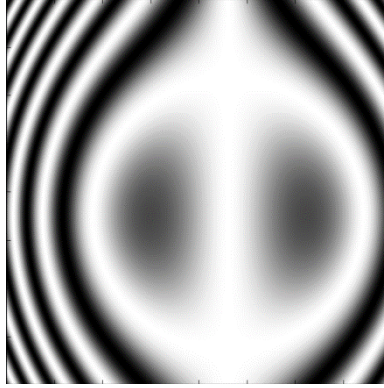


Figure 16: A simulation of a shear plate image using two parts spherical, one part coma and two parts of either defocus or astigmatism.

The ambiguity that is present in shearing interferometry made it less than desirable for analyzing the beam quality without a suitable reference. A more direct approach is to use a wavefront sensor to directly measure the beam quality. Various types of wavefront sensors (WFS) exist which analyze small portions of the incident beam for local pointing direction [90, 91]. The spatially dependent pointing vectors are used to determine the phase front of the incident beam. The wavefront sensor used to characterize the recording beam is a Phasics SID4 wavefront sensor that uses a 4-wave lateral shearing interferometer based on a modified Hartmann test [92]. This essentially uses a two dimensional thin diffraction grating to split the incident beam into 4 beams propagating at slightly different angles and forming a two dimensional interference pattern in the form of a grid. Distortions in this grid are used to calculate the local wavefront gradient and a Zernike polynomial fit is used to determine the aberrations present.

The WFS was used to measure aberrations at several critical points along the beam path of the holographic recording setup so that the source of the aberrations could be determined. These

results are summarized in Table 3. Because the final beam was larger than the aperture of the WFS, two measurements were made. In the first, only the central portion of the beam (~8 mm x 8 mm) was measured. To obtain full aberration information, a second measurement was made by using a focusing lens to make the beam fit within the aperture of the device. The defocus was subtracted out of this measurement as it was taken in an artificially focused beam. The individual aberrations are relatively low in the final beam but the wavefront distortion does approach the level of 0.5 wave peak to valley (P-V) across the aperture of the final beam. The Pi-shaper does contribute to the defocus in the beam but this has been compensated for by adjusting the focus of the final beam expander. Overall, there is some increase of spherical and coma aberrations from the input beam but these results show that the additional beam shaping optics do little to decrease the initial recording beam quality. To show the worst possible effect that such aberrations can have on an RBG, the simulation method of this section was used to calculate how much the measured aberrations could deteriorate the spectral shape of the RBG which was simulated previously. The ‘worst case’ was generated by modifying the signs of each aberration and probing the grating with a 5 mm beam in the ‘up’ position since this gave the most extreme deteriorations. The results of these simulations are shown in Figure 17. Although some deterioration of the side lobes exists and there is a small drop in peak efficiency of about 1%, the bandwidth remains the same. These effects have been decided to be insignificant considering that they are a worst case scenario. Based on this analysis, the current recording setup is capable of producing high quality RBGs with thicknesses of 20 mm and minimal distortions of spectral shape due to aberrations.

Table 3: Wavefront error of the recording beams measured at various locations.

	Total WFE P-V/RMSE	Defocus	Astigmatism 0°/45°	Coma x/y	Trefoil 0°/30°	Spherical Aberration
After 1 st expander	0.526/0.065	-0.002	-0.009/0.021	0.015/0.004	-0.005/ -0.025	0.001
After Pi-shaper	1.531/0.32	0.286	0.023/-0.004	0.038/0.006	-0.013/ -0.011	-0.028
Final Beam Center	0.249 /0.037	0.0	0.006 /-0.005	0.002 /-0.004	-0.017/ -0.031	0
Final Beam + Lens – Defocus	0.499/0.09	NA	0.003 /0.033	- 0.047/0.056	-0.019/ 0.007	-0.015

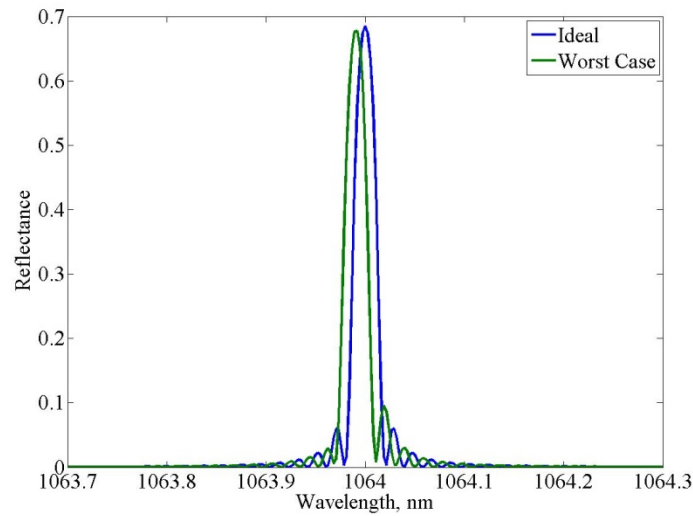


Figure 17: The expected deterioration of a 20 mm RBG with 20 ppm RIM in the presence of the measured aberrations of the recording beam assuming worst possible contributions.

Phase Stabilization During Holographic Recording

After finding the effect of wavefront distortions on holographic VBG recording to be insignificant for our recording setup, the next major source of holographic degradation to be considered is the vibration stability of the recording system. The vibrational stability is a critical parameter for holographic recording because interference patterns with periods as low as 200 nm are frequently used. Any motion in the delivery optics or recording media at a fraction of this level can cause a smearing and washing out of the interference pattern. This results in a low contrast refractive index modulation and makes the strength of the VBG dependent upon the vibrations of the surrounding environment. To achieve high quality volume gratings with high-efficiency, it is necessary to be able to generate a uniform sinusoidal modulation throughout the volume of the medium as well as a high contrast refractive index modulation. As an example, for gratings being designed as output couplers for laser systems, it is usually necessary to achieve very specific spectral width and angular selectivity in addition to precise diffraction efficiencies, making it critical to have exact control over the RIM [93]. The primary detriment to obtaining consistent fringe visibility, and therefore high-quality VBGs, is shifting of the interference fringes during the recording process. Such fringe movement can be due to vibrations of beam delivery optics or the sample, as well as localized changes in the relative density of air along the paths of the recording beams.

By measuring and controlling the relative phases in the recording beams, high visibility fringes can be maintained throughout the recording. The resulting VBG will have a consistent refractive

index modulation with efficient use of the material's dynamic range. To control the phase of the interference pattern, a number of different methods have been proposed [94-98]. The most common is the use of the dynamic grating formation, or through the use of an auxiliary grating to diffract a portion of each recording beam into the other recording beam to generate an interference pattern [95, 96]. For a universal recording setup, capable of recording many different kinds of gratings with different periods, it is preferable to avoid the use of an auxiliary grating since this is only applicable to a single grating period and is not a versatile solution, requiring a new reference grating for each new grating period. The use of self-diffraction to produce wave-mixing from a dynamically formed grating has shown the best performance in phase control. This method allows for direct monitoring of the relative shift of the interference pattern and the current grating structure. The drawbacks of this method relate to the restrictions that it places on the recording media. Using the dynamic grating formation requires the recording medium to have low absorption at the recording wavelength and not introduce significant distortions into the beams. Most importantly, the material must also form a weak grating during the recording process. This may not always be the case when a latent image is formed and further development is necessary, or where the dimensions of the recording substrate are not able to produce useful diffraction. So, while the use of dynamic wave-mixing is applicable to some holographic recording setups, it lacks the flexibility necessary for recording gratings in a variety of materials including PTR glass. To address this issue, a new, simple, flexible method for phase stabilization that can be applied to most common holographic recording setups is proposed. The method shares the same path as the recording beam but does not place any requirements on the recording medium. This method combines some of the aspects of the last system proposed by

Guest [97] and the system by Muhs [98], but provides better flexibility and sensitivity to phase shifts.

Before describing the method for stabilizing interference fringes, it is important to determine the effect of an uncontrolled fringe pattern. When using two beam interference to record a grating, as shown in Figure 12, the resulting spatial RIM is directly proportional to the two beam interference intensity pattern when operating within the linear region of the material photosensitivity curve [99]. This interference pattern is given by Eq. 22,

$$I(x) = I_1 + I_2 + 2\sqrt{I_1 I_2} \cos(2kx \sin \theta + \phi) \quad (22)$$

where I_1 and I_2 represent the irradiance of each recording beam, and the resulting refractive index modulation profile is proportional to the cosine with a period determined by the wave vector (k) of the recording beam and the angle of interference, θ . The term ϕ is the relative shift in phase between the two recording beams. Modification of any of the arguments in the cosine of Eq. 22 will result in a shifting fringe pattern. The wave vector of the recording laser is held constant and it is assumed here that the angle of interference is stable at the arcsecond level such that no significant change in period occurs. This stability has been confirmed experimentally in the recording setup by measuring the angle stability of the recording mirrors by forming a Sagnac interferometer and monitoring the shifts of fringes. Practically speaking, this level of stability in angle is not difficult to achieve with commercially available optical mounts and a vibration-isolated table. The most significant effect on the interference pattern comes from changes in ϕ ,

primarily due to vibrations and air fluctuations. This results in a shifting of the relative phases between the recording beams as a function of time. The recorded interference pattern in this case is given by Eq. 23.

$$I_{final}(x) = I_1 + I_2 + \int_0^T 2\sqrt{I_1 I_2} \cos(2kx \sin \theta + \phi(t)) dt \quad (23)$$

The effect of randomly varying phase difference about a mean value can be calculated to determine a tolerance to phase noise allowable in a recording system. For this calculation a randomly varying phase difference described by a Gaussian probability density function is assumed, which will allow the effect on the fringe pattern to be described by a single parameter relating to the variance of the phase fluctuations. The probability density for a randomly distributed phase variation is shown in Eq. 24.

$$W(\phi) = \frac{1}{\sqrt{2\pi}\sigma} e^{-\frac{\phi^2}{2\sigma^2}} \quad (24)$$

Here σ is the RMSE about the average phase value. The interference pattern can then be described by the integral in Eq. 25.

$$I_{final}(x) = I_1 + I_2 + \int_{-\infty}^{+\infty} W(\phi) \cdot 2\sqrt{I_1 I_2} \cos(2kx \sin \theta + \phi) d\phi \quad (25)$$

The fringe visibility of the resulting interference pattern (V) is the metric which will be used to determine the quality of the recorded grating. This value is a normalized indicator for the amount of the maximum possible index change that can be achieved:

$$V = \frac{I_{max} - I_{min}}{I_{max} + I_{min}} \quad (26)$$

Equation 25 was integrated numerically for a number of σ values to determine the effect of fringe shift on the visibility. The results are shown in Figure 18 as a function of the fraction phase variation, measured in fractions of the recording wavelength. As the amplitude of the phase variations increases, the fringe visibility starts to decrease, resulting in a weakened RIM. The value of σ in radians can be determined from the x axis by multiplying by 2π . For high values of σ beyond 0.5 waves, the fringe pattern will be effectively washed out because the phase during recording will cover a full 2π range. Therefore, practical systems for holographic recording are most likely operating in the range depicted. The inset in Figure 18 shows the region of minimal phase fluctuations in which we operate using phase stabilization. In this region the decrease of visibility is relatively slow. A tolerance of fluctuation amplitude less than 5% of a recording wavelength will guarantee fringe visibility >95% of the optimum value.

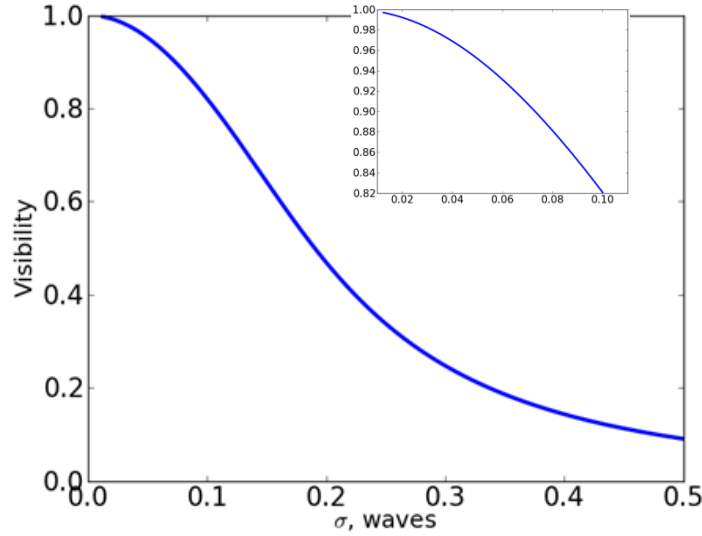


Figure 18: The decrease of visibility as the variation in phase fluctuations increases. Phase variation σ is shown as a fraction of the recording wavelength. Detail is shown on different scales in the inset.

To eliminate this unwanted phase noise, the setup shown in Figure 19 will be used to control phase fluctuations by sampling a small portion of the recording beam to measure the relative phase of the recording beams, while the rest of the beam is used for the recording. The portion of the beam used for phase measurement will be called the probe beam. The phase measurement is achieved through a corner cube retroreflector which is placed above the sample. The probe and recording beams trace along collinear paths to reach the recording plane and the probe beam is then reflected back along this path to double the relative phase deviations which are incurred. At the detector plane, the back-reflected probe light forms an interference pattern and the corner cube is adjusted in position to achieve overlap of the two collinear probe beams so that the entire beam diameter gives a zero fringe interference pattern. The intensity of this pattern can be related to the relative phase of the two recording beams. One of the primary benefits of this method is

that the precision of this alignment can be very coarse. The retroreflector guarantees angular alignment and beam overlap can be achieved without the use of precision stages.

As the relative phases of the paths change, the irradiance at the detector will vary as Eq. 22 with $\theta=0$. By using a retroreflector, the system can be easily moved and realigned for recording gratings of different period and arbitrary grating tilt angles. The detector signal is used as feedback and a piezo-electric transducer (PZT) is placed beneath one of the mirrors to correct for measured phase fluctuations by maintaining a constant detector signal.

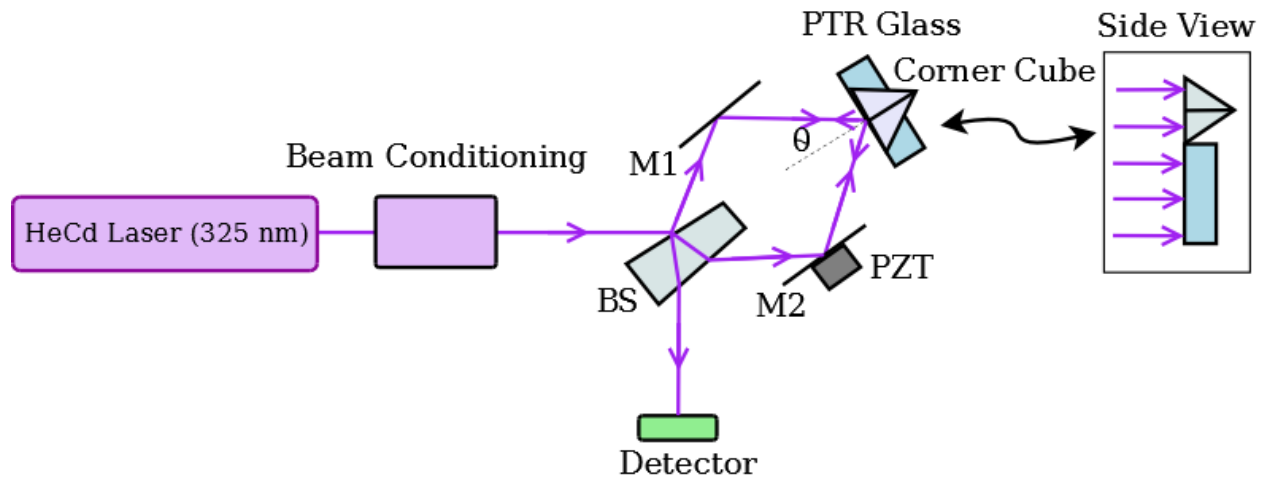


Figure 19: The VBG recording setup showing the paths of the recording/probe beam. The side view shows how the beam is split between a recording portion and a probe portion for measuring phase.

The phase difference in the recording beam can be extracted from the measured variations in the detector voltage. In order to determine the conversion factor between the detector's voltage and the probe beam phase difference, a calibration of the system was performed prior to any

measurement of phase. The calibration was accomplished by driving the PZT with a ramp function to generate a sinusoidal variation in the detector voltage with a period corresponding to a phase difference in the probe beam of 2π as shown in Figure 20. By fitting a sinusoid to this curve, a conversion function was calculated to convert a detector voltage to a phase difference between the beams.

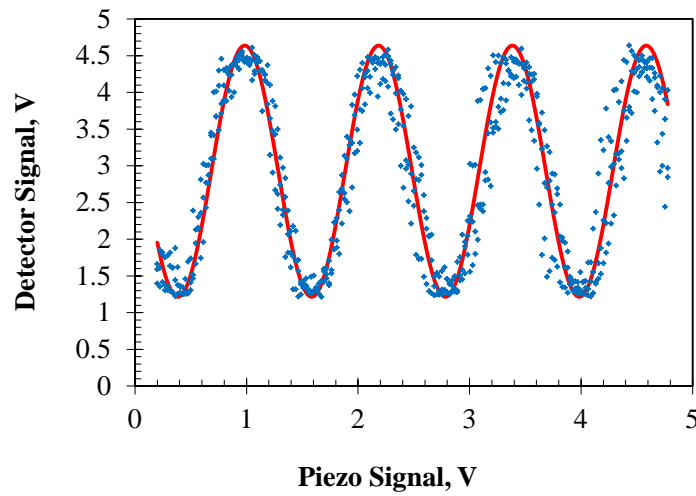


Figure 20: Ramping of the PZT voltage allows a shift in the detector voltage, centered about the DC level, to be converted to a fraction of a phase shift once the period is determined. Red line shows a fit to the experimental data in blue.

While the shifting of the phase of the two recording beams is important to the stability of the setup and has many components that can contribute to errors, the shifting of the sample and how it is mounted must not be ignored. The sample has 6 degrees of freedom, but primarily tilt about the y axis and displacement in the x axis of Figure 4 can contribute to errors in the recording. The roll about the z axis can also potentially disrupt the fringe visibility. The magnitude of the effect

will depend on the location of the center of rotation for this axis. For example if the center of rotation is at the center of the sample, then the top and bottom portions of the grating will be moving in opposite directions causing inhomogeneous distortions across the face of the grating. More likely, the center of rotation will be somewhere below the sample in the mounting structure, in this case all portions of the sample will move in the same direction with roughly the same amplitude (depending on the distance to the rotation point and size of the sample). Therefore, motion of roll about the z axis, can be considered similar to displacement in the x axis given that these assumptions hold for the recording setup in question. The errors of tilt about the y axis only affect the recording substantially due to the different shift that they induce of the front of the material relative to the back. Therefore, the displacement in x , which will be referred to as lateral shift, is a critical motion to control. The questions of whether or not the proposed system is sensitive to these motions must be answered.

For comparison, the most common method of phase stabilization [97] using a grating has recently been shown to be sensitive to lateral displacement [100]. While counterintuitive, a shift of a transmitting or surface reflection grating by one period will shift the relative phase of the transmitted and diffracted orders by 2π . Therefore, there is a one to one correspondence between the lateral shift in the measurement device (measured in number of wavelengths) and the shift of the interference pattern which is being monitored to measure phase. This makes phase control systems using a grating able to measure and correct for lateral shifts.

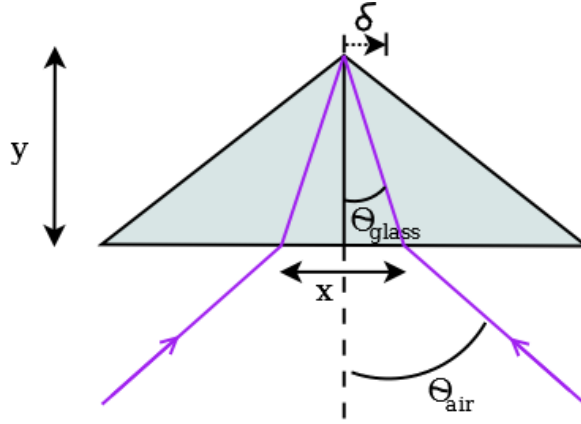


Figure 21: Diagram of a retroreflector in a phase stabilization system with designation of variables for calculating lateral sensitivity.

To show that a retroreflector is also sensitive to these shifts, the nature of the optical path to and from the retroreflector must be considered. The optical path encountered by a ray which has traveled from a particular phase plane, reflected off of any part of the retroreflector and back to that initial plane, is equal to twice the distance from the starting plane to the optical center of the corner cube [101]. Therefore it is possible to model optical path length in an interferometer by geometrically drawing a line from a reference point in the beam path to the optical center of the corner cube. Since this system deals with measuring relative lateral shifts, the location of this optical center is not important and can be considered to be located at the corner cube vertex [102]. With this understanding, it is intuitive from Figure 21 that a shift of δ will cause a relative shift between two beams incident at the same angle. This is because the optical path for one beam will shorten, while the other will lengthen. Mathematically this takes the form of Eq. 27.

$$OPD_{\text{glass}} = 2 n_0 \sqrt{(x + \delta)^2 + y^2} - \sqrt{(x - \delta)^2 + y^2} \quad (27)$$

$$\text{where } y = \frac{x}{\tan(\theta_g)}$$

Where OPD is the optical path difference, θ_g is the angle of the probe beam within the glass, n_0 is the refractive index of the corner cube (therefore hollow corner cubes will produce the same results with $n_0 = 1$), and the planes of equal phase are taken to be at the corner cube's front surface for simplicity. Assuming the shift is small, the square of the displacement is negligible, and Eq. 27 can be simplified to the result in Eq. 28.

$$OPD_{\text{glass}} = 2 n_0 2\delta \sin(\theta_g) \quad (28)$$

This OPD gives the phase difference that can be detected when a lateral shift of δ occurs in the retroreflector. Considering that the period of the grating is given by Eq. 29, then if the retroreflector shifts by one grating period, the measured OPD will be twice the wavelength of the probe/recording beam. That is, the induced phase shift in the probe beam will be twice the lateral shift of the recording plane when quantified as a phase value. This is due to the invariance of the product of $n_0 \sin\theta$ by Snell's law, and the use of the same beam as the probe and for recording. The result is exactly what is desired because any phase shifts that occur before the recording plane are also doubled in the probe beam because of the double pass configuration. Therefore, this system is able to accurately measure lateral shifts of the recording plane.

$$\Lambda = \frac{\lambda}{2 \sin(\theta_{air_{rec}})} = \frac{\lambda}{2 n_0 \sin(\theta_{glass_{rec}})} \quad (29)$$

An experimental verification of the sensitivity to lateral motion was conducted to confirm the accuracy of the approximations. The experimental setups for comparing the sensitivity of the retroreflector to the sensitivity of a TBG are shown in Figure 22. Along with verifying the presence of lateral sensitivity in a retroreflector, experimental verification of the lateral sensitivity of a transmitting VBG is important since all previous discussion in the literature of grating sensitivity to lateral motion was conducted using thin gratings. To date, no studies have been conducted which relate to the sensitivity of a phase stabilization system to lateral motion. Since this is motion is equally detrimental as phase changes that occur in the delivery path, such a study is extremely important.

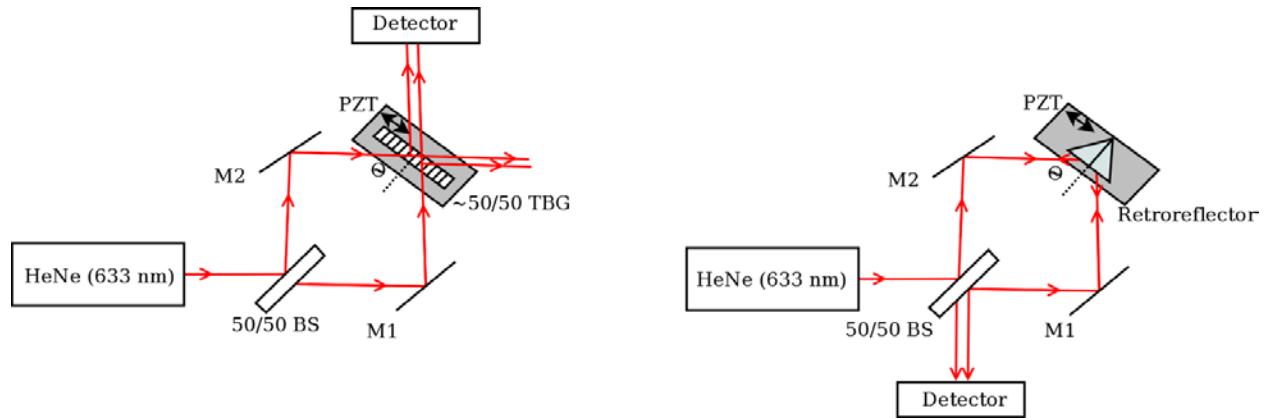


Figure 22: Experimental setup to demonstrate the lateral sensitivity of a TBG in comparison to a corner cube retroreflector. The PZT is used to shift the respective measurement device. The effect of lateral shift on the signal measured at the detector is monitored.

The piezoelectric transducer was oriented such that it could induce lateral shifts of the two phase measurement devices. Both interferometers were aligned to measure the interference of a He-Ne laser operating at 633 nm and incident on the devices at approximately 13.5° . The TBG is designed to diffract a beam at this angle with approximately 50% diffraction efficiency. To observe the sensitivity to lateral motion of each of the setups, the PZT was ramped through a voltage range and the intensity change at the detection plane was monitored. The two signals that were received are shown in Figure 23. Both methods result in periodic signals at the detectors caused by phase incursion between the interfering beams and, therefore, demonstrate measureable sensitivity to lateral shifts induced by the PZT. The most important feature to note is the roughly twice higher frequency of the oscillations in the retroreflector signal as expected by theory. The difference between the frequencies of each signal is not exactly a factor of two. This discrepancy is simply due to not precisely controlling the direction of the PZT motion to be exactly orthogonal to the axis of interference. Another important feature is the higher visibility of the fringes produced by the retroreflector. While this increased visibility isn't necessarily related to a difference between the systems, it does highlight ease of alignment afforded by the use of the retroreflector. A reference grating system requires that the grating be aligned to the interfering beams in tip about the y axis, roll about the z axis and for small beams, displacement about the z axis to get good beam overlap. This alignment is very time consuming to optimize, whereas the corner cube can be aligned without precision stages in a matter of seconds to obtain an interferogram at the detection plane. Despite these differences it is clearly shown that both methods have sensitivity to lateral motion and the relative sensitivity confirm the results in

Eq. 28, making both methods equally suitable for correcting these detrimental motions in a holographic recording.

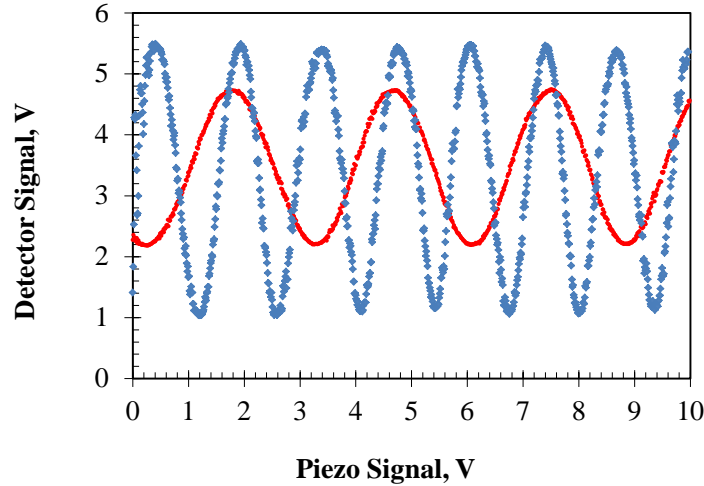


Figure 23: The interference signals received from measurements of lateral sensitivity of a TBG in red and a retroreflector in blue.

It is important to note that the performance of a phase stabilization system cannot be completely evaluated by detecting the feedback signal with the system operating in an open feedback loop and then closing the loop and comparing the relative amplitudes of fluctuations between the stabilized and unstabilized system. While this would demonstrate the effectiveness of the feedback system, it does not directly show the effect that this has on the quality of the VBG recording. If phase stabilization results in no change in the grating performance, the system is either measuring incorrectly or phase fluctuations are not responsible for quality of recording. Based on the analysis of the effects of phase fluctuations in this section, the primary effect of an unstabilized system is to reduce the RIM. Therefore, by demonstrating an improvement of a

grating's RIM it can be concluded that phase fluctuations were deteriorating the RIM depth and that phase stabilization was successful in controlling these fluctuations. This experiment was conducted using the setup depicted in Figure 19 to record reflecting VBGs with a resonant wavelength of 978 nm and the time for each recording was 22 min. From these recordings an increased RIM due to increased fringe visibility in the phase stabilized recordings is expected to be observed. In a reflecting VBG with high diffraction efficiency, an increased RIM will correspond to a higher bandwidth. The RIM can be calculated by matching measured spectral response to those calculated by theory. Before the exposure of each grating, the feedback signal was monitored so that the phase noise present in the recording environment could be determined. After exposure and development, the gratings were cut to a thickness of 3.75 mm and measured using a wavelength tunable laser. The transmission spectrum of each grating was used to determine the RIM induced in each recording. This method of testing phase stabilization demonstrates the effect of stabilization directly on the desired result, rather than in an indirect method as is typically done in the literature. Showing an improvement in the final device, not only proves effectiveness of the system, but also confirms the calculations showing fringe instability leading to a decreased RIM.

The first grating of this experiment was recorded with no stabilization present. Figure 24 shows the phase difference calculated from the measured feedback signal before and during the recording, using Figure 20 for conversion. The relative phase of the beams has both high frequency noise and a slowing drift in one direction. These oscillations are the result of phase drift in one direction because the detector is measuring the sinusoid of a phase term and there is a

2π phase ambiguity. Using the Eq. 23 the best fringe visibility that can be achieved by recording in this condition is $76\% \pm 5\%$ of a perfect recording with no phase shifts. Uncertainty in this measurement is due to changes in the average intensity in the recording beam and is evident only when observing a change in the inflection points of the signal in the region near $\pm\pi/2$. The transmission spectrum is shown in Figure 25. The refractive index modulation can be calculated based on knowledge of the spectral bandwidth and length of the grating. For a 3.75 mm thick RBG with resonant wavelength of 978 nm, a 430 pm bandwidth corresponds to 490 ppm index modulation.

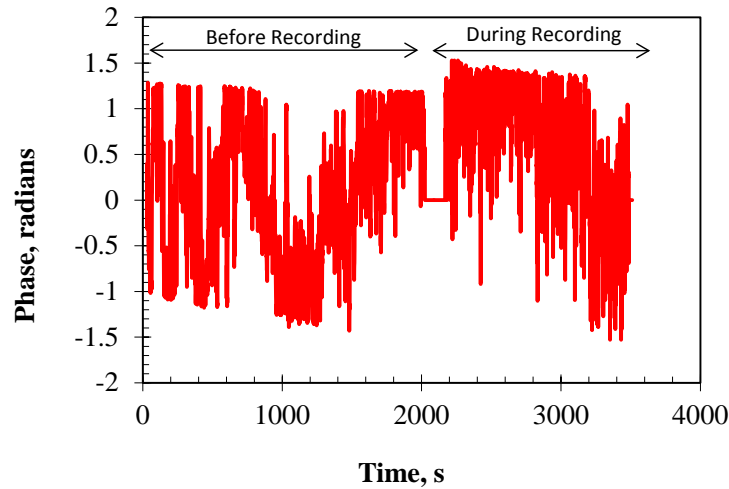


Figure 24: The phase before and during the recording of a baseline, unstabilized RBG.

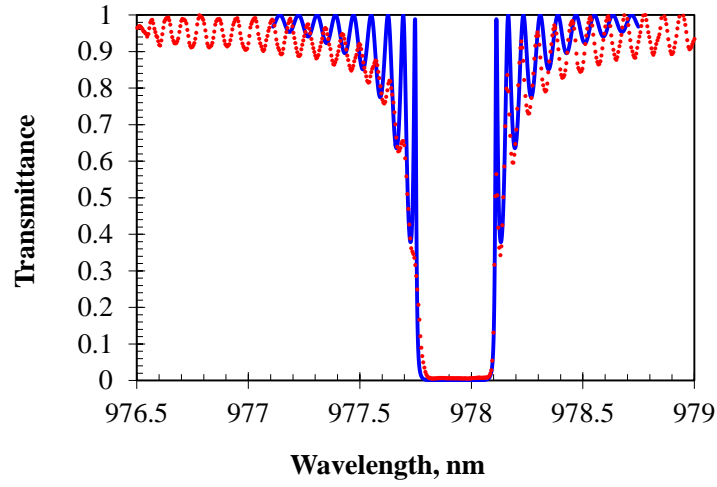


Figure 25: The transmission spectrum of a RBG that was recorded without stabilization. The measured data is in red and theoretical fit in blue.

A second RBG was recorded using the same parameters. During the recording process, the PZT was used to maintain a constant relative phase of the recording beams. Figure 26 shows the phase variations immediately before recording and during. The remaining noise has an RMSE of 0.0052λ and the expected visibility of this recording is 99.8%. The signal sent to the PZT during the recording is shown on the same plot to demonstrate how it was used to counteract the phase noise. At a thickness of 3.75 mm, the bandwidth of 660 pm as shown in Figure 27 corresponds to an index modulation of 740 ppm.

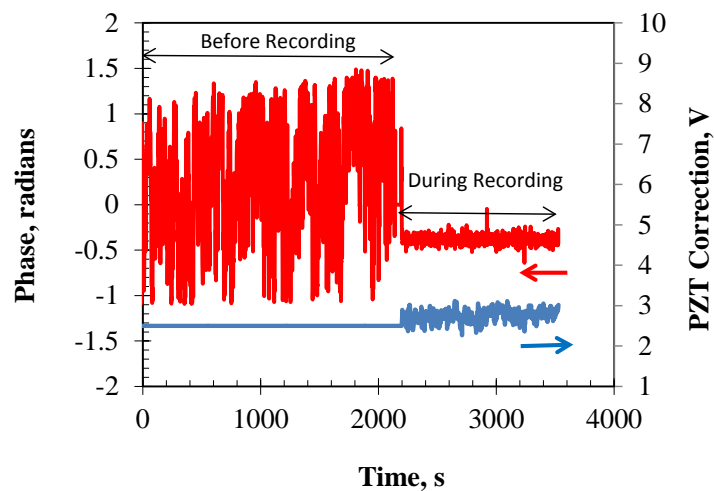


Figure 26: The phase and PZT signal before and during a recording using phase stabilization in the presence of high frequency phase noise.

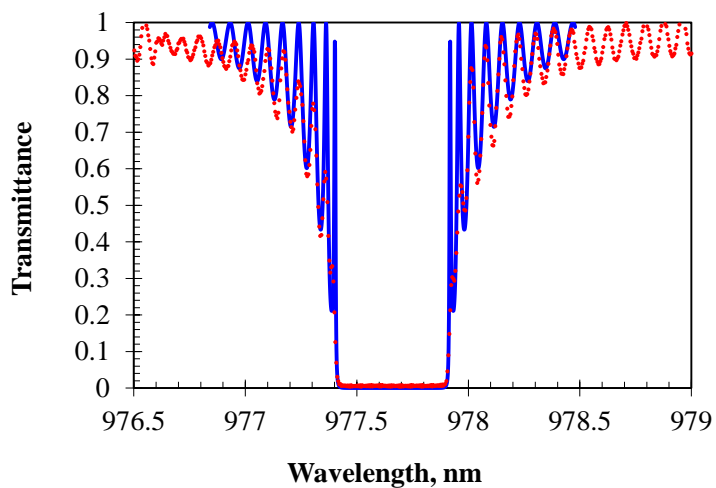


Figure 27: Transmission spectrum of the RBG recorded with phase stabilization in the presence of high frequency noise. The measured data is in red and theoretical fit in blue.

The grating shown in Figure 27 did not undergo a long-term drift as was present in the unstabilized case, so a third RBG was recorded where the environmental phase variation (Figure 28) showed a long term drift similar to that of the grating without phase stabilization in Figure 24. The expected visibility from the measured relative phase during recording is 99.7% and the RMSE is 0.0057λ . The correction voltage applied to the PZT shows a linear drift during the recording, indicating that it is working against the linear drift in the environment as expected. At a thickness of 3.75 mm, the bandwidth of 670 pm in Figure 29 corresponds to a refractive index modulation of 750 ppm. This value matches well with that of the grating in Figure 27, confirming proper measurement of relative phase and effective correction. Thus the grating recorded without phase stabilization has a RIM that is 66% of the RIM in the grating recorded with stabilization. This deviates from the calculation that predicts 76%, but is of the right general scale given the uncertainty in the measurement and typical homogeneity of RIM of about 5%. The use of this phase stabilization system is shown to correct the phase to a level where consistent high visibility fringes can be recorded over long exposure times.

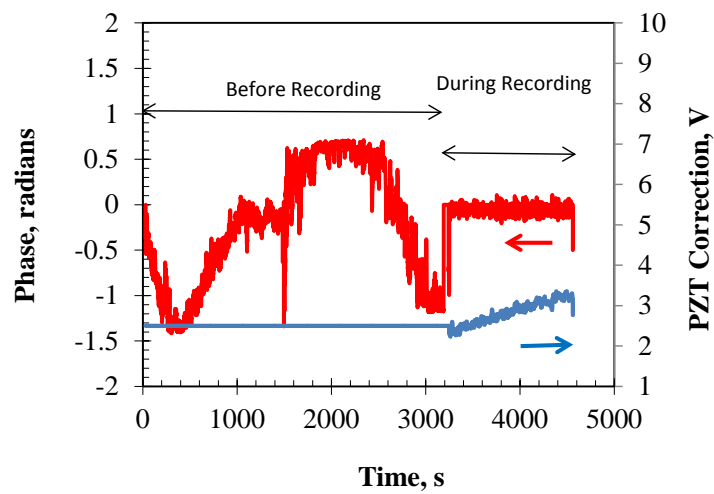


Figure 28: The phase and PZT signal before and during the recording of a RBG with phase stabilization and long term drift.

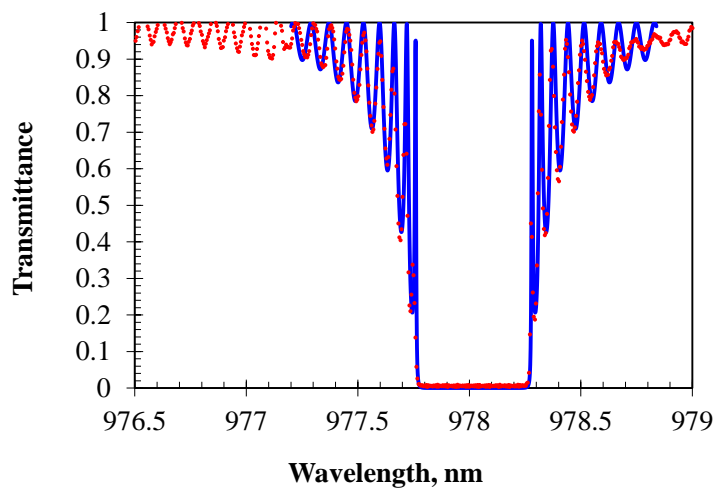


Figure 29: Transmission spectrum of the RBG recorded with phase stabilization in the presence of long term drift. The measured data is in red and theoretical fit in blue.

As an additional investigation, the source of the slow drift was explored. The motivation of this investigation was that while successful phase correction was demonstrated, the drift of the system would often be so severe that the PZT would run out of its range of correction. The desire for the phase stabilization was to have a fundamentally stable system with an active feedback control to make minor corrections. The source of the drift was traced to the sample mount which showed a correlation with the ambient temperature of the room. Figure 30 shows the temperature drift overlaying the phase drift. The linear drift of temperature appears to cause a linear drift of the phase (if phase unwrapped) and the slowing of the temperature drift correlates with the rapid slowing of the phase drift. This experiment provided reasonable data for supporting the idea that the recording platform was drifting in position or angle due to temperature variations. Using a different mount with less thermal dependence reduced the oscillations significantly. For the purposes of demonstrating phase stabilization, the less stable mount was used as it provided an excellent challenge for the control system to overcome.

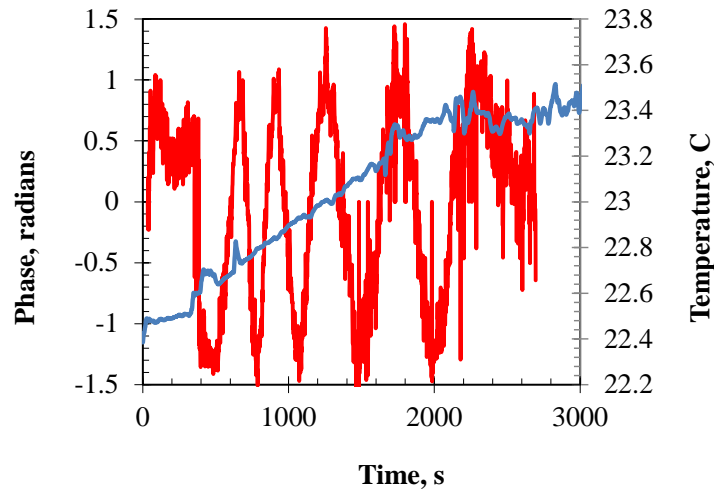


Figure 30: A comparison of the phase drift of the recording system (red) to the temperature at the recording plane (blue), demonstrating a close correlation of the phase drift to temperature.

In conclusion, the major detriments to high quality VBG recording have been addressed in the holographic recording system used to create the VBGs for this dissertation. The issue of wavefront aberrations in the recording beams has been shown to be insignificant. This was determined by developing a complete model of the effect of aberrations in a thick recording media and characterizing the actual aberrations in the system. Given the worst-case contributions of the measured aberrations, minimal distortions of the reflection spectrum of a very narrowband reflection grating were calculated using this model. Therefore, wavefront aberrations were determined to be insignificant for the VBGs recorded in this dissertation and attention was placed on measuring and controlling vibrations in the recording setup. A demonstration of a new method for phase stabilization was shown to be effective in stabilizing the relative phases of a two beam interference pattern. The method can be applied to the recording of VBGs of arbitrary period without the need for specialized components or difficult alignment procedures.

Simulations regarding the effect of shifting phase show that RMSE variations must be maintained below 0.05λ to maintain fringe visibility above 95%. The proposed system was shown to produce phase stabilization of both the probe and recording beams well within this tolerance. An increase of 50% in the induced refractive index modulation was shown by using phase stabilization during the recording of several gratings. This phase control setup provides the ability to create repeatable VBGs with maximum refractive index modulation by ensuring fringe visibility of close to 100%.

3 SINGLE VBGs FOR LASER APPLICATIONS

While the main focus of this dissertation is multiplexing of gratings, it is beneficial to demonstrate examples of precision recording of standard single VBGs before moving on to more elaborate geometries. Single VBGs are useful for laser systems as output couplers, for locking of laser diodes in external cavity configuration, and for laser beam combining systems. These applications are well studied and use VBGs in a straightforward method to bend light within a particular Bragg condition. For output couplers that are used to lock a laser to a very narrow spectral bandwidth, this is typically achieved using an RBG with low index modulation and long interaction length. The ability to create a homogeneous recording through a very thick substrate limits the extent of the filtering that can be achieved, though devices and methods for overcoming these limitations will be discussed in further sections. Practically speaking, a thickness of around 25 mm is the limit for current PTR VBG technology discussed in this dissertation based on Figure 12. Depending on the resonant wavelength of the grating, this corresponds to a bandwidth of around 20 pm. To demonstrate experimentally that this is possible with the recording setup, an RBG was recorded to be an output coupler and longitudinal mode selector at 976.75 nm. The spectrum of this grating is shown in Figure 31, and exhibits a bandwidth of 24 pm with a reflectance of 32% in 23 mm of glass. Such a filter can create single frequency laser for cavity lengths less than 2 cm.

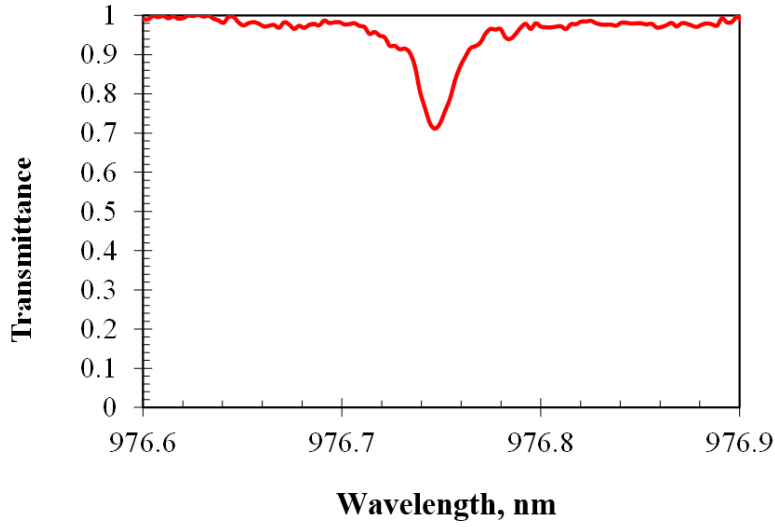


Figure 31: A narrowband RBG with bandwidth 24 pm and 32% efficiency with resonant wavelength of 976.75 nm.

While the use of the reflection bandwidth of an RBG is commonly utilized for spectral filtering, the angular selectivity of the TBG has not been extensively utilized. Analogous to single longitudinal mode selection by an RBG, the angular acceptance of the TBG can be used to generate single transverse mode within a laser cavity. The angular spectrum of a zeroth order transverse electro-magnetic wave has a width (FWHM) that is determined by the beam's $1/e^2$ radius at the beam waist and the wavelength as is given by Eq. 30 [103].

$$\theta_{\text{FWHM}} = \frac{4\lambda}{2\pi w_0} \quad (30)$$

The design of the bandwidth for a longitudinal mode selector in an RBG is straightforward since it is designed for a normally incident operation, and bandwidth is not strongly dependent on the

angle of incidence. In contrast, the Bragg angle can vary much more widely in the case of the TBG and becomes an important design tool. Assuming that a constraint is placed on the diffraction efficiency such that n_I is used to achieve 100% DE, the parameters that effect bandwidth are the Bragg angle (controlled by the grating period) and the thickness. Additional design constraints are the physical geometry of the recording which limits the periods that can be recorded and the Raman-Nath boundary discussed on page 9. If the grating qualifies as thin, then multiple diffraction orders occur and 100% diffraction efficiency cannot occur.

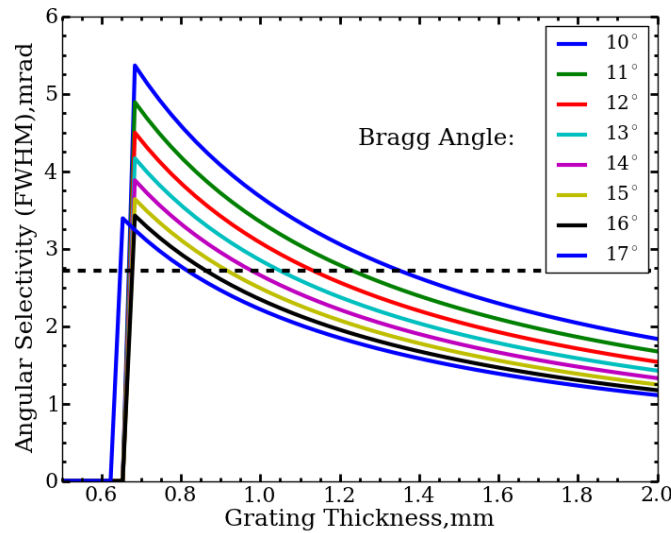


Figure 32: Design curve of the angular selectivity of an unslanted 100% diffraction efficiency TBG with resonant wavelength of 1064 nm using grating thickness and Bragg angle as design parameters.

Simulations were run for a TBG to have a bandwidth (FWHM) of 2.71 mrad in order to create a single transverse mode in a 0.5 mm diameter beam (at $1/e^2$ of maximum) for a wavelength of 1064 nm. These results are shown in Figure 32. Light is incident at the various Bragg angles and

the relation between thickness and angular acceptance is shown. The RIM is varied so that diffraction efficiency is always 100%. The cutoff occurring at low thicknesses is for $\text{RIM} > 800 \text{ ppm}$ to give a sense of what gratings are practical in PTR glass. The final design of the grating is such that light is incident approximately normal to the surface and the grating is tilted within the media to diffract light at twice the Bragg angle in air with respect to the surface normal, making alignment much simpler for the end user. This alternative configuration does not change the bandwidth of the grating by more than a couple of hundredths of milliradians and hence Figure 32 remains a valid design curve.

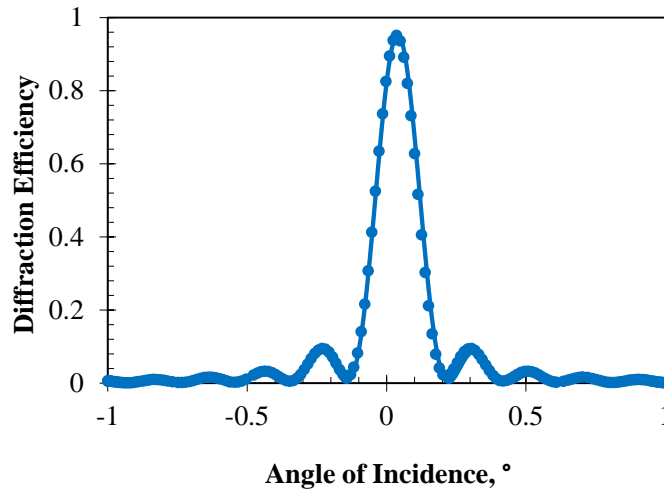


Figure 33: The angular selectivity of a TBG designed for transverse mode selection of a beam with 0.5 mm diameter. Measured results (dots) are in excellent agreement with theoretical calculations (line).

A 1 mm thick grating with an angle of incidence of 0.04° , a grating tilt of 8.66° (corresponding to an untilted TBG with Bragg angle of 12.9°) and RIM of 460 ppm was recorded. The measured

angular selectivity at 1064 nm is shown alongside a fit with theory in Figure 33. The FWHM bandwidth is 2.91 mrad (0.167°) and the diffraction efficiency is 95%. Using two such gratings, the filtering can be applied to two orthogonal planes to generate a single order transverse mode [104].

It is evident from Figure 32 that achieving certain angular bandwidths can be difficult from a practical point of view. Namely, very broad selectivity requires a smaller thickness than can be obtained using PTR glass, or a small Bragg angle which corresponds to a very small recording angle. With the setup of Figure 12, this means a very long propagation distance. To overcome this, another convenient but often overlooked feature of the transmission Bragg grating can be used. This feature is the sinusoidal dependence of diffraction efficiency on thickness as given in Eq. 16. Typically a high efficiency grating is achieved by making the coupling constant ν equal to $\pi/2$, but this same efficiency can occur with ν equal to $3\pi/2$ which will be called a twice over-modulated grating (single over-modulated grating with $\nu=\pi$ gives 0% efficiency at the Bragg angle). While efficiency remains the same, the shape and bandwidth of the angular spectrum will change significantly. This design feature can be used in one of two ways: first by keeping thickness constant but by tripling the index modulation to give a wider angular selectivity and secondly by keeping index modulation the same and tripling the thickness of the grating to obtain a more narrow angular selectivity.

To demonstrate this principle, an alternative design for filtering of a 0.5 mm diameter beam was used. In this case, the Bragg angle was kept roughly the same with angle of incidence of 0.29°

with a grating tilt of 9.1° (corresponding to untilted Bragg angle of 13.2°). The thickness of the grating is 1.94 mm and the RIM is 840 ppm. The measured angular spectrum at 1064 nm is shown in Figure 34 with a FWHM bandwidth of 2.57 mrad (0.147°) and 97% efficiency is shown. The results of this design demonstrate that similar efficiency and bandwidths can be achieved using a much different grating thickness by using over-modulation as a design tool.

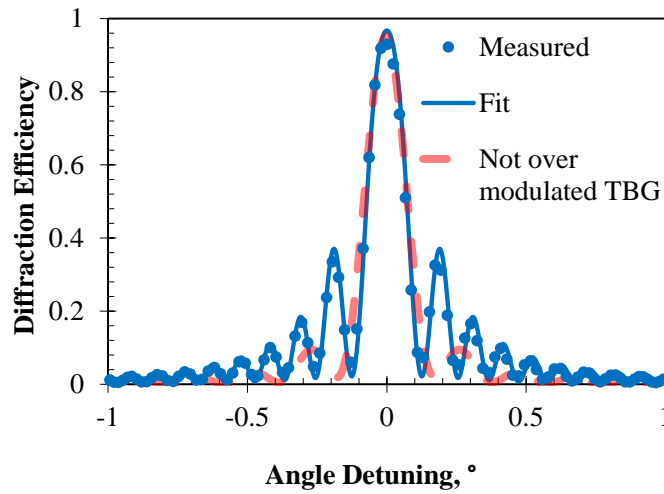


Figure 34: The angular selectivity of a twice over-modulated TBG designed for transverse mode selection of a beam with 0.5 mm diameter. Measured results (dots) are in excellent agreement with theoretical calculations (line). For comparison, the angular selectivity of the similar non-over-modulated TBG is shown as red dashes.

In conclusion, the capabilities to produce high quality RBGs and TBGs for demanding design criteria have been demonstrated. A very narrowband single RBG was measured to produce a bandwidth of 24 pm. The design of TBGs for mode selection produced useful design curves showing practical angular selectivity values that can be achieved in PTR glass. A new type of TBG based on twice over-modulation was shown as a method for producing broader angular

selectivity without requiring thinner media or smaller diffraction angles. Experimentally measured angular selectivity curves show excellent agreement with theory for both standard and twice over-modulated TBGs. These devices were also successfully integrated into a laser system for transverse mode control [104]. This concludes the section on the state of the art of recording single VBGs in PTR glass. In order to realize new functionality with VBGs in PTR it is necessary to investigate multiplexing as a design tool.

4 MULTIPLEXED GRATINGS FOR BEAM STEERING

Having demonstrated the technical capabilities of recording single VBGs it is now appropriate to discuss the first steps taken to multiplex gratings. These are primarily independent gratings recorded in the same piece of glass that do not couple or interact with each other as discussed in the review on multiplexed grating types on page 34. In their most general form, these types of gratings allow a single optical device to redirect multiple laser channels to a desired location. The primary applications that will be studied are beam steering devices for beam combining. The motivation for beam combining is to create a compact high-power laser system with a narrow spectral linewidth and good beam quality. Currently, continuous wave near infrared fiber laser sources are commercially available with power levels of several kilowatts. Scaling fiber laser systems beyond these power levels is mainly limited by thermal and nonlinear effects. There has been much interest in the use of spectral beam combining (SBC) and coherent beam combining (CBC) to combine multiple high power laser systems into a single diffraction limited beam in order to bypass these limitations [63]. In CBC, several lasers emitting at the same wavelength are spatially combined such that all the lasers are locked in phase. In SBC, multiple channels at different wavelengths are superimposed spatially which can be achieved using a dispersive element such as a VBG. In both cases, multiplexed VBGs can be designed to greatly reduce the complexity of the combining setups. This section focuses on the latest progress of multiplexed VBGs for beam steering applications and advances in control of relative grating parameters, as well as the interactions of multiple gratings in volume recording media.

Scaling Multiplexed Channels for High Power Spectral Beam Combining

Recent demonstrations using RBGs recorded in separate pieces of PTR glass have achieved a total combined power of 0.75 kW over a 1 nm spectral range after combining five laser channels using four VBGs [105]. The most commonly used metric for quantifying the beam quality of a zeroth order Gaussian laser beam is called the M^2 parameter, with a value of 1 being diffraction limited and values higher than 1 being associated with the presence of higher order modes [106]. A diffraction limited beam (low M^2 parameter) will produce the smallest possible far field spot size and therefore the largest concentration of energy at a target in the far field. The resulting combined beam in the system demonstrated in [105] had an M^2 of 1.6. The goal of multiplexed VBGs for SBC is to take the system in [105] and realize it using a single optic while achieving similar power levels and improved beam quality. The first step towards this goal is the combination of two high power lasers with a double multiplexed RBG (2x RBG) and a third laser beam which is out of resonance with the device, that is transmitted through the device as shown in Figure 35.

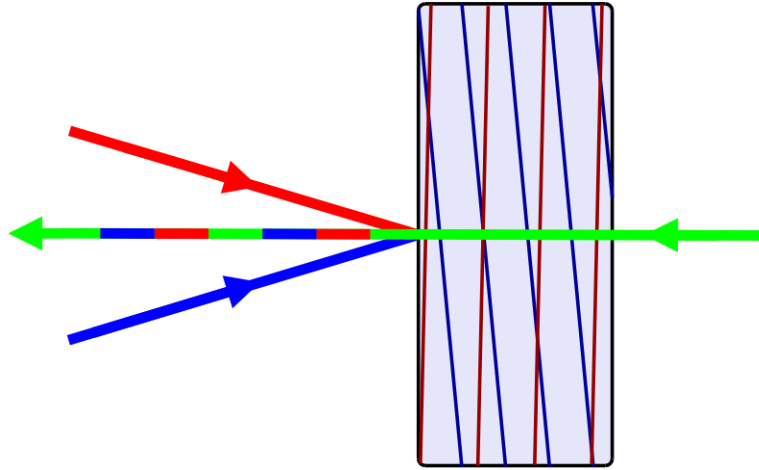


Figure 35: Schematic of a 2x multiplexed RBG for spectral beam combining using a third out of resonance input to combine three beams.

The 2x RBG was designed for two lasers with central wavelengths of 1064.86 nm and 1063.54 nm within a 200 pm tuning range. The grating was designed such that, at 5° angle of incident with respect to the surface normal, each laser is reflected parallel to the surface normal, superimposing them with the third out of resonance transmitted beam. The relative Bragg wavelengths between the two gratings was necessary to be accurate within the tuning range of the lasers (± 100 pm) at the Bragg angle of 5°. To allow an additional level of tuning, both Bragg wavelengths were designed 700 pm lower than the laser central wavelength so that they could be temperature tuned to reach the desired resonance wavelength in the system. Temperature tuning occurs by heating the grating such that the device expands and the resonant wavelength shifts to higher wavelength. Using this method, the resonant wavelength of the grating can be controlled at a rate of 10 pm/C and any unwanted heating due to absorption of high power radiation can be compensated for. Temperature tuning of VBGs is produced by mounting the VBG on a thermo-electric cooler (TEC) to control the grating temperature.

In order to produce high efficiency combining, the strength of each grating needed to be sufficiently high to produce >99% diffraction efficiency. Beyond this target, the design of the relative efficiency of each grating is not critical because there is no degeneracy between the two individual gratings. Any inequality of grating strength would only result in a widening of the reflection bandwidth by tens of picometers. Since the spacing of the wavelength channels is >1 nm this broadening of the bandwidth would still not cause crosstalk between the individual gratings. Therefore, there was no need for precision matching of RIM between the gratings.

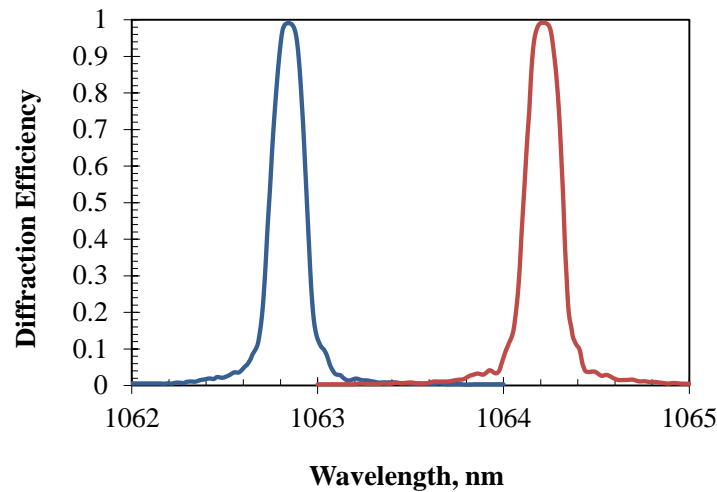


Figure 36: The diffraction efficiency of the two arms of a 2x RBG for SBC measured by probing along the combining arm with a low power tunable laser. Efficiency is >99% with bandwidth of 215 pm +/- 10 pm.

After recording using the system shown in Figure 12, the device was tested using a low power tunable laser along the common path of the combined arm shown in Figure 35. The transmitted light and the light reflected into each of the input arms of Figure 35 were measured as the laser

wavelength was swept through the range of interest. The reflection spectrum of the 2x RBG device used for the SBC experiments is shown in Figure 36. Efficiency for each grating is >99% and the bandwidth is $215 \text{ nm} \pm 10 \text{ nm}$.

One of the most important design requirements for high power beam combining is the use of a combining element with very low levels of absorption. While PTR has extremely low absorption in the near infrared on the order of $10^{-4}/\text{cm}$, even the absorption of several percent of a 100 W laser can lead to significant heating of the element. As the heat load increases, distortions of the combined beam, as well as thermal lensing, result in an increased M^2 value. The heating can be mitigated by recording devices with very low absorption and controlled in the final system by using the aforementioned TEC approach to maintain a constant device temperature [107]. The device has been designed such that scattering losses were limited to <0.1%. This requirement was based on previous experiments using single RBGs for SBC. For the 2x RBG device presented here, scattering losses were the main source of loss in the device and were measured to be 0.05% at 1064 nm. The high reflection efficiency and low losses of this multiplexed grating made it well suited for high power beam combining.

After successful characterization at low power, the 2x RBG was mounted in a copper housing and connected to a TEC (Figure 37) for use as a combiner at power levels of several hundreds of Watts. The beam quality of the input lasers was characterized using a commercially available M^2 meter. The two lasers that were used to reflect off of the 2x RBG had an M^2 value of 1.05 along both axes and the third laser used for transmission through combiner had an M^2 value of 1.13 in

the x direction and 1.16 in the y direction. The x direction is shown in Figure 37 and the x - z plane corresponds to the plane of reflections.

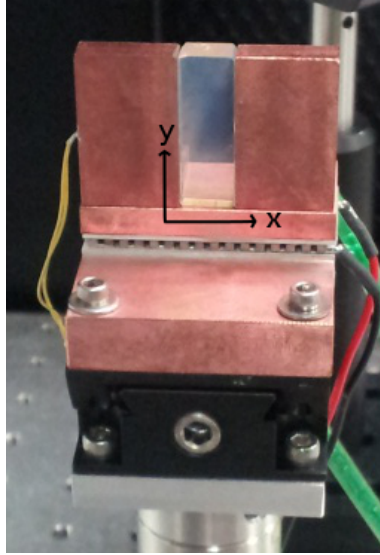


Figure 37: The housing for thermally controlling the multiplexed RGB for beam combining.

The first experiment was done in a reflection only geometry without any laser being transmitted through the combiner. The total combined power was 282 W out of a total of 285 W incident, giving a 99% combining efficiency. The beam quality was preserved with an M^2 of the combined beam being 1.15 in the x direction and 1.08 in the y direction. Throughout the experiment, the 2x RGB was kept at a constant temperature of 70 C using the TEC in Figure 37. Just as heating of the VBG with the TEC can be used to tune the wavelength to a desired value, unwanted heating due to absorption of the high power radiation will cause the grating period to change and go out of resonance, destroying the combining. In this combining configuration, no heating was observed and the TEC was not adjusted to bring the VBG back into resonance.

Next the transmitted laser was added to the setup to study the combining of three channels as depicted in Figure 35. The wavelength of this laser was 1063.3 nm such that it was out of resonance with both of the multiplexed gratings. This setup gave a total combined power of 420 W out of 438 W for a combining efficiency of 96%. Heating of the grating due to the introduction of the third laser was observed and required that the TEC be adjusted by 8° C in order to bring the grating back into resonance. The M^2 was measured to be 1.38 in the x direction and 1.20 in the y direction. This slight degradation of the combined beam quality compared to the incident beam quality can be explained by the heating induced in the 2x RBG.

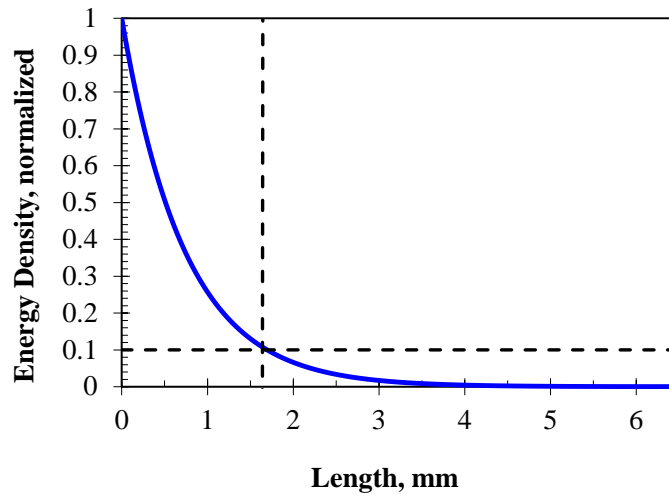


Figure 38: The fraction of power present along the grating thickness for an RBG designed for 1064 nm with 230 ppm RIM shows that 90% of the power is reflected within the first quarter of the grating.

In order to understand why the transmitted beam causes such significant heating, it is important to discuss the dynamics of the reflection by a VBG. Following Ghiringhelli [108], the energy density distribution throughout the thickness of a reflecting grating at Bragg resonance was calculated for the gratings used in these experiments and results are shown in Figure 38. The distribution includes the contributions of both forward and back propagating modes for the grating and was normalized to the maximum energy density occurring at the incident face. It is clear that 90% of the optical power only encounters the first quarter of the grating. As a result, most of the energy is reflected close to the incident surface and the reflected beams occupy a smaller volume fraction than the transmitted beam. Therefore, the transmitted beam travels through a much larger volume fraction of the VBG than a reflecting beam, resulting in significantly higher absorption and heating. This result is of significant importance for beam combining experiments because it demonstrates that implementing a reflection only geometry is more desirable for heat management and results in an improved combined beam quality.

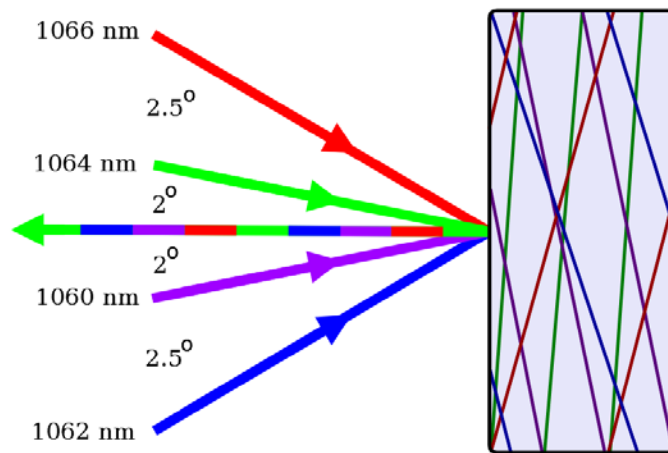


Figure 39: A reflection only multiplexed grating for spectral beam combining of four laser channels.

With successful demonstration of beam combining using a 2x RBG at high power levels, the next step is to demonstrate scalability of such a system. A new multiplexed grating (4x RBG) was designed to combine four laser channels in a reflection-only geometry to minimize the thermal load and detrimental beam distortions. The device and design angles are shown in Figure 39. The performance was tested by probing the common arm with a tunable laser and measuring the splitting efficiency in each of the input arms. The relative diffraction efficiency of each individual grating is shown in Figure 40 and remains above 98% for each combining channel. This characterization shows that scaling of the number of multiplexed gratings recorded in PTR glass can occur while maintaining high efficiency.

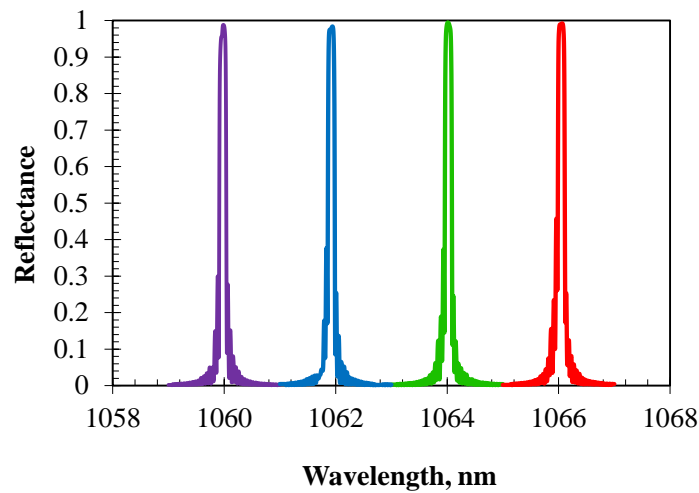


Figure 40: The reflection spectrum of the four channel spectral beam combining with each channel demonstrating combining efficiencies above 98%.

Finally, the reflections from the 4x RBG were characterized with an M^2 meter at low power to demonstrate that there are no inherent deformations being caused by increasing the number of gratings within the sample. The M^2 of each of the beams reflected from the 4x RBG was measured using an M^2 meter as the light incident on the common arm was tuned to each of the reflection peaks. The results are summarized in Table 4. Again, the reflection occurs in the x - z plane. No degradation of the beam quality is observed relative to the incident beam quality after reflection from the multiplexed RBG. These results show that homogeneity of the grating and subsequently, the reflected beam quality, is preserved in a multiplexed grating with increased number of combining channels.

Table 4: The M^2 values of beams reflected from a four channel multiplexed reflecting Bragg grating.

	Wavelength, nm	M^2_x	M^2_y
Incident Baseline	1064	1.13	1.20
Multiplexed	1060	1.10	1.19
RBG	1062	1.12	1.19
	1064	1.07	1.22
	1066	1.10	1.23

From these low power tests, the scalability of multiplexed volume Bragg gratings in PTR for applications in beam combining has been verified using the 4x RBG. Combined with results of high power combining with a two channel multiplexed grating, the pathway to combining more laser systems to achieve higher power beam combining with high efficiency is established.

2x TBG for Coherent Beam Combining

Coherent combining of laser beams can lead to even higher spectral radiance because there is no separation of wavelength between the various input channels. Multiplexed volume Bragg gratings in PTR have recently been used to demonstrate an active coherent combining by locking fiber laser cavities with a common output coupler as shown in Figure 41 [109]. The individual cavities share a common output coupler through the use of the combining TBG and therefore become locked in phase. This recent success has prompted an investigation into understanding and improving the combining efficiencies obtained through the use of multiplexed VBGs. In particular, the critical parameter in multiplexing gratings for coherent combining is the relative efficiency of each grating. For TBGs this is an especially difficult problem because the efficiency changes with the sine of the grating strength according to Eq. 16 whereas the RBGs efficiency will saturate with increasing strength according to Eq. 17. The goal of this study was precise recording of multiplexed transmission gratings for high efficiency CBC.

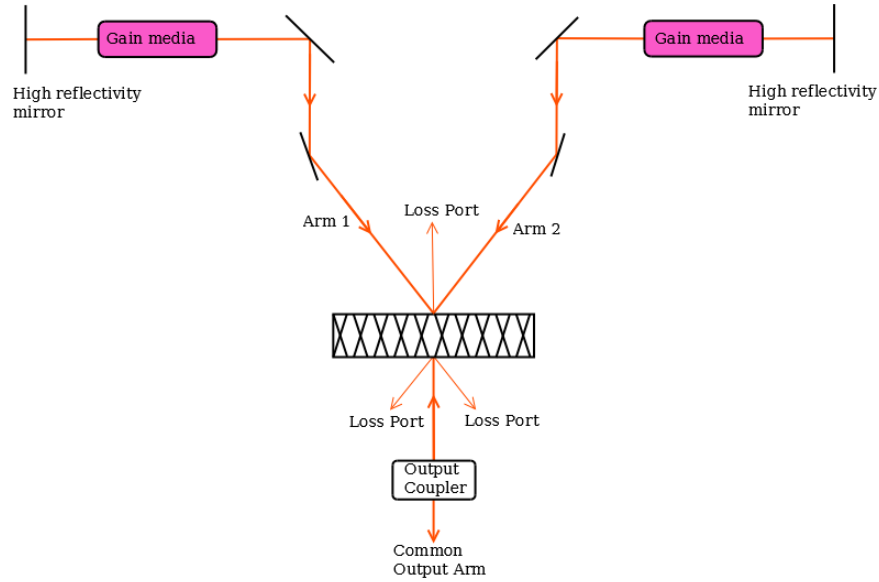


Figure 41: Coherent beam combining using a multiplexed 2x TBG to couple two laser cavities.

The multiplexed TBG designed for these experiments is shown in Figure 42. The device can be used either as a splitter or combiner by the principle of reversibility. The 2x TBG is designed to combine light with a wavelength of 1064 nm from Arm 1 and Arm 2 at $\pm 23^\circ$ in air and produce a common output that is normal to the surface. The period of each grating is $2.7 \mu\text{m}$ and the grating tilt with respect to the surface normal is $\pm 7.6^\circ$. To achieve equal strength of each multiplexed grating, a heuristic approach was used to determine the appropriate dosage to apply to each sequential recording. The dosage of the first recording was 0.346 J/cm^2 and the second recording was 0.354 J/cm^2 corresponding to a difference in applied dosage (and therefore recording time) of 2.4%. The device thickness is 1.97 mm and was developed to produce a RIM of 190 ppm for each individual grating. For reference, if the two gratings were not degenerate, they would each have a diffraction efficiency of 80-85% given these conditions. Since they are degenerate, this RIM produces a combining/splitting efficiency close to 100%. A theoretical

model of sequentially recorded TBGs has been developed by Kowarschik [110]. The 2x TBG for CBC presented here fits into the scenario of section 3.2. Simplification of terms assuming a well aligned, symmetric design geometry with equal RIM for each grating produces the requirement for RIM shown in Eq. 31 such that maximum combining efficiency is achieved.

$$n_1 = \frac{\lambda \sqrt{\cos(2\theta_{tilt})}}{2\sqrt{2}t} \quad (31)$$

Here n_1 is the RIM required for each individual grating, λ is the resonant wavelength, t is the device thickness and θ_{tilt} is the tilt angle of the gratings with respect to the surface normal. In the general derivation, θ_{tilt} is actually the angle between the wave vector of the incident light and the grating planes, but for a symmetric design shown in Figure 42, these two angles are the same. For the device parameters listed above, the required RIM for each grating is 188 ppm giving individual grating efficiency of 80%. Therefore, due to the degeneracy of the two gratings, the individual RIM depends on Eq. 31 and this RIM would not produce 100% efficiency for an individual grating of similar parameters, operating independently.

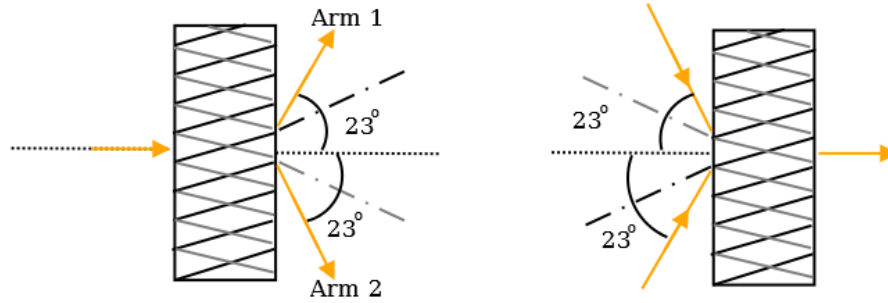


Figure 42: The basic operation of a multiplexed TBG being used as a high efficiency splitter on the left and a high efficiency combiner on the right.

For the purposes of testing the performance of a CBC grating, it is easiest to characterize it as a splitter since no control over the phase of the incident light is required. The principal of reversibility of light allows this characterization to predict the peak combining efficiency that can be achieved by the device as a combiner given effective control over the optical phase of the incident beams. Characterization as a splitter is achieved by sending light of a fixed wavelength to the grating at normal incidence as shown in the left side of Figure 42. Rotating the grating using a motorized stage and monitoring the changes in optical power of the transmitted beam and the light in Arms 1 and 2 allows the angular selectivity of the device to be measured. In Figure 43, the angular selectivity of this device is shown. For high efficiency CBC, the important characteristic of this transmission is the minimum value of the central arm. In this case the minimum transmission is 3.6% meaning that a combining efficiency of up to 96.3% can be expected from this device. The angular selectivity of the 2x TBG also reveals important information about the relative alignment of the two individual gratings within the device. At the point of minimum transmission in the central arm, the transmission efficiency of both Arm 1 and Arm 2 are equal meaning that equal RIM was induced in each grating due to the modification of

applied dosage. The mutual alignment of the gratings can be seen by the fact that all angular spectra are centered at the same angle of incidence and the sidelobes and shape of the angular selectivity of Arms 1 and 2 show excellent overlap.

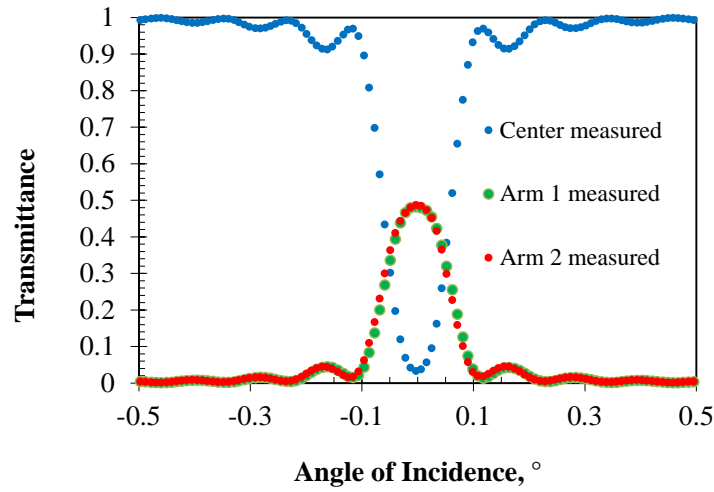


Figure 43: The experimentally measured angular selectivity of a 2x TBG for CBC tested as a splitter. Arm 1 and Arm 2 refer to the left and right splitting arm as viewed from above.

Next, the performance of the device as a combiner was measured in an active beam combining setup shown in Figure 44. In this setup, a 1.5 mW laser is split using a beamsplitter and recombined coherently using the 2x TBG. A PZT is mounted on one of the turning mirrors to allow the relative phase of the incident beams to be controlled. Detectors are used to monitor the relative optical power in the transmitted and combined arms of the setup. In ideal combining, light from both input arms would be directed entirely to Detector 2 when the PZT was shifted such that each input arm interfered constructively. Alignment of the incident beams is achieved by optimizing the diffraction efficiency of each beam into the degenerate central arm. Best

alignment is achieved when, for example, Arm 1 of Figure 44 is diffracted strongly into the central arm as well as partially being directed to Detector 3. This means that the light incident in Arm 1 is ‘seeing’ the grating for Arm 2. This interaction occurs because as soon as light from Arm 1 is diffracted into the common arm, it will start to interact with the second grating because the common arm is degenerate. This complex interplay produces some light being transmitted to Detector 3 when light from Arm 1 is well aligned to the grating, with Arm 2 being blocked. The next step of alignment is to make sure that the two beams in the degenerate arm produce a high visibility zero fringe interference pattern. A good alignment produces diffraction of both incident beams into the common arm with good efficiency, spatial overlap and angular alignment. Such alignment will produce modulation of the intensity of the central arm with high visibility as the PZT is translated, shifting the relative phase of the incident beams. A linear ramp of the voltage applied to the PZT will produce sinusoidal modulation of the intensity at each detector. Monitoring the visibility of this modulation during the PZT ramp provides a good metric for the quality of the alignment with high visibility indicating good alignment. During the linear ramp, the intensity of light reaching all three detectors can be used to calculate the combining efficiency at the point of maximum intensity being sent to Detector 2. Using the aforementioned 2x TBG, this alignment procedure consistently produced a relative combining efficiency of >90%. Factors that contribute to deviations from the results expected by the splitter include the relative polarization and intensities of the beams split by the beamsplitter, and the overall sensitivity of the active combining setup to vibrations. Controlling these factors, or utilizing a passive combining system will allow combining efficiencies to more closely match the splitting efficiency that was demonstrated during characterization.

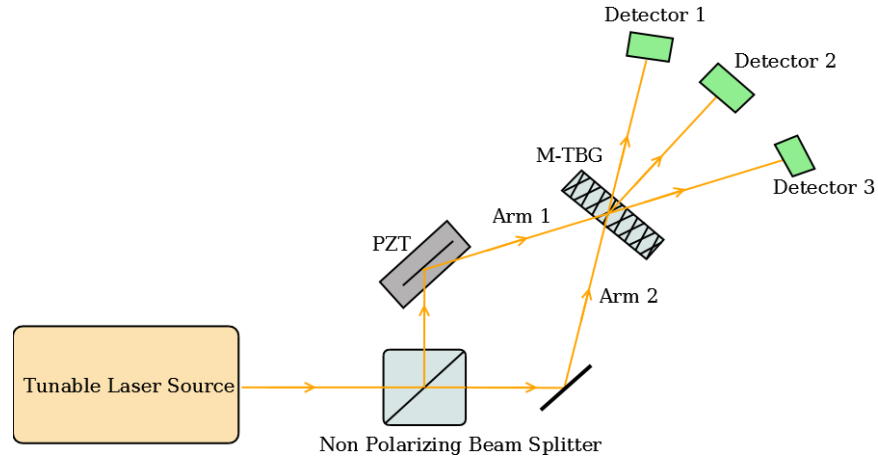


Figure 44: System for testing the performance of a multiplexed TBG (M-TBG) for coherent beam combining.

In conclusion, a 2x multiplexed TBG in PTR glass has been shown to give excellent coherent beam combining efficiency. The angular selectivity of the device shows that important design features such as equality of the sequential recordings, mutual alignment of the gratings and overall efficiency have been precisely controlled and measured. The combining efficiency of >90% matches well with predicted results from measuring the device as a beamsplitter. These results are promising for future coherent beam combining systems that require high efficiency combining

4x RBG for Coherent Beam Combining

The final type of beam steering multiplexed grating is intended for use in coherent beam combining as a reflecting element. This combining geometry differs from the multiplexed TBG on page 93 as shown in Figure 45. The combining setup demonstrates combining of two laser systems, but multiple lasers can be added by multiplexing more reflecting Bragg gratings into a single combiner. The 4x RBG which will be discussed in this section has aspects of both independent and interdependent multiplexing that must be considered when used for CBC.

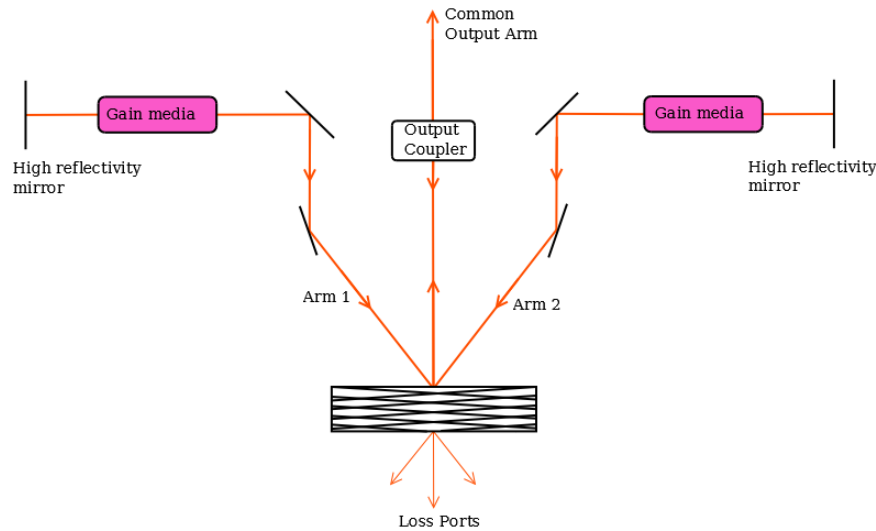


Figure 45: Coherent beam combining using a multiplexed RBG to couple two laser cavities.

The step from a spectral beam combining grating to a coherent beam combining grating requires much more precise control of the recording parameters. Not only are the relative grating tilts important, but now all of the grating periods must precisely match the designed tilt angle. In

spectral beam combining there was a degree of tuning available by adjusting the wavelength of the combining lasers which is no longer available. Additionally it is very important to obtain equal levels of diffraction efficiency in each individual grating. All the gratings have a common channel and therefore will experience cross coupling. Relative differences in the grating strengths will result in unequal splitting between the channels and efficient energy coupling between the channels will not be achieved. This additional constraint on the recording was not present in spectral beam combining since each individual grating operated independently. In summary, a reflecting grating for coherent beam combining must have each grating period and tilt matched so that a common channel exists between each input channel and the diffraction efficiency of each grating must be equal so that when light is incident along the common channel, it is split equally into each of the non-common channels.

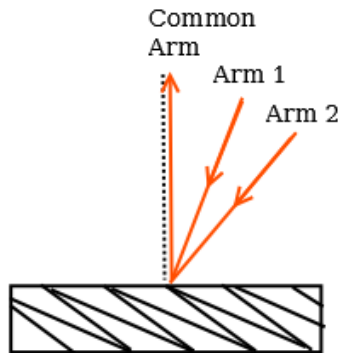


Figure 46: Source of parasitic resonance due to multiplexing. Bragg angles that are multiples of each other will allow Arm 1 to be reflected by the grating for Arm 2 at the normal incidence Bragg wavelength.

An additional design consideration is the interplay of the various combining arms that can occur due to the many multiplexed gratings recorded in the material. These unwanted resonance

conditions can interfere with the combining process and must be considered when designing the combining angles of the device. In coherent beam combining, each grating is designed for the same wavelength and when expanding the number of combining channels, the most obvious way to do this is to make all input channels separated by the same angle. Two such channels on the same side of the common output are illustrated in Figure 46. This makes Arm 1 incident roughly normal to the grating that has been designed for Arm 2. Due to the difference in periods, this will not be resonant with the grating that is intended for Arm 2. But if such a device is used in the configuration shown in Figure 45, there will be multiple wavelengths generated by the gain media which can be resonant on-axis with this grating. This will cause generation of lasing within the cavity formed by this grating. To avoid this unwanted behavior, the combining angles on the same side of the common arm were not made to be multiples of each other as is shown in Figure 47.

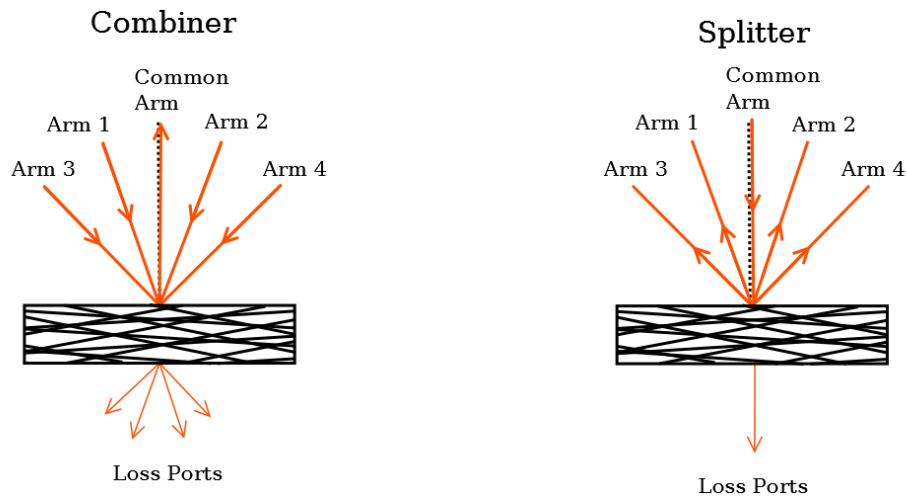


Figure 47: Using a 4x RGB as beam combiner and as a beam splitter. The loss ports exhibit the direction of light if the efficiency of the overall device is not high enough or if misalignment is present.

The figure also demonstrates two ways the 4x RBG can be used. The first use is a combiner as is proposed for Figure 45, and the second use is as a splitter. The splitting configuration is a useful way to characterize the grating performance before being used for beam combining. The measurement of the device as a combiner requires that all inputs be phase matched, whereas the splitting function uses a only a single input and no phase shifting is necessary, making it a much simpler geometry for characterization. The important parameters of the 4x RBG to achieve combination into a single common arm are the grating periods and relative tilt angles between each grating. Therefore when testing the device, both the wavelength and angle response must be measured. This measurement is achieved by using the tunable laser to sweep the wavelength of incident light at a number of different incident angles. Placing photo-detectors in Arms 1-4 enables the diffraction efficiency into each individual arm to be measured under various angles of incidence and wavelengths.

A grating was recorded according to the asymmetric design proposed in Figure 47. The design wavelength is 1064 nm and the angles of incidence for Arms 1-4 are 2°, 4°, 6°, and 10°. Note that the angle of incidence of the combining arm is twice the Bragg angle in air and the tilt of the grating is such that it bisects the input arm and the common arm. Each grating was recorded with equal dosages such that the total dosage of the exposure added up to 0.7 J/cm². Using a tunable laser, the spectral response of each arm was measured for a number of angles of incidence along the common arm. The results of this measurement are shown in Figure 48 and Figure 49 and provide critical information about the quality of the recorded gratings. The first thing to note is

the lack of flatness in the spectra. This flatness occurs when the wavelength sweep is done at the appropriate Bragg angles. The fact that all the spectra are not flat at the same angle of incidence means that there is misalignment of relative tilt angles. The spectra are not always centered at the same wavelength value e.g. the bottom right panel of Figure 49. This is due primarily to the relative shifts of the central wavelength of the tunable laser. Since only one detector was used, each measurement of spectra was done with a slightly shifted starting wavelength and therefore the central wavelength of each individual spectra has some error associated with it on the order of tens of picometers. Regardless, the central wavelengths of each grating are slightly shifted with respect to each other but within the wavelength acceptance of the grating and therefore there is still a significant wavelength band where combination can occur. Finally, the sum of the efficiencies for a given wavelength and angle combination gives >95% efficiency of the grating and there are several specific combinations of wavelength and angle where each arm contains close to 25% of the incident light.

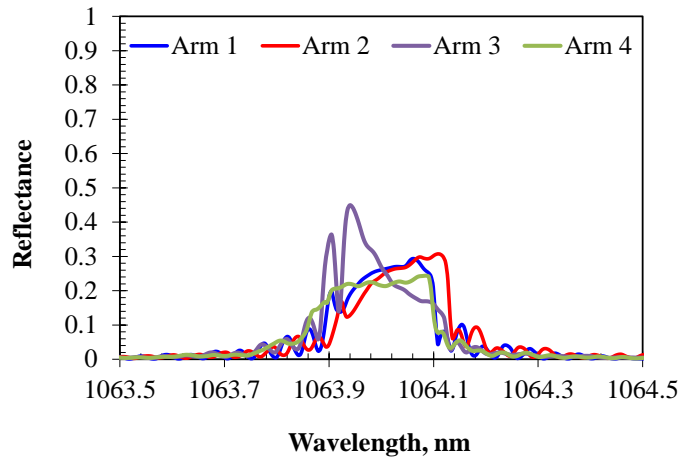


Figure 48: The diffraction efficiency of each arm of the 4x RGB for CBC using a probe beam at normal incidence to the grating.

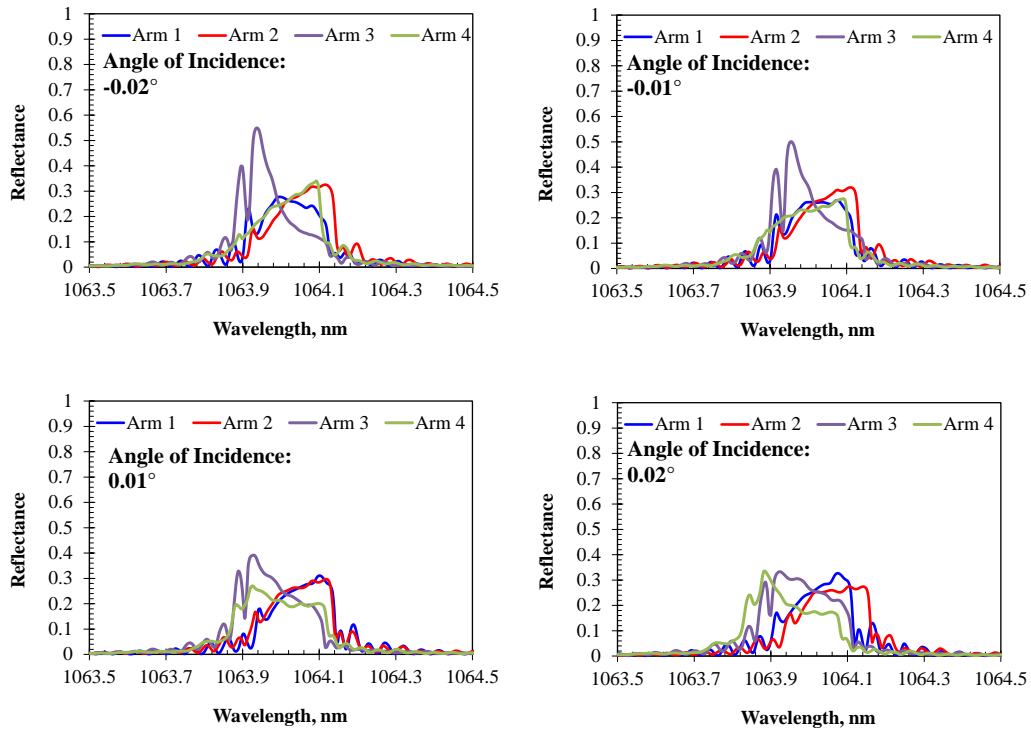


Figure 49: A series of wavelength spectra of efficiency of each arm at different angles of incidence with respect to the grating normal.

The grating was then used to combine four beams at low power for a proof of concept. To verify the ability to coherently combine with high efficiency, a tunable laser source was split into four paths using beam splitters. Turning mirrors mounted on PZTs were used to redirect the beams to the RBG combiner. All beams were incident at the design angle and wavelength to produce reflection into the combined arm. Small adjustments of the position and angle of each arm allowed a zero fringe interference pattern between each reflected beam and spatial overlap better than $100\text{ }\mu\text{m}$ was obtained by monitoring the position of each reflection using a beam profiler. The wavelength for combining was determined by looking at the reflected spectrum of each individual arm. The wavelength that generated the most equal reflectance values with the flattest spectral responses was selected. The incident power of each arm was found to be critical in obtaining high efficiency combining. Without equalizing incident power, only 75% of the incident light was combined when the power in each arm varied by up to 40%. When the power in the arms was equalized to better than 5% using neutral density filters, an absolute combining efficiency of 90% was obtained. The M^2 of the incident beam, each reflected beam, and the final combined beam was also measured. Results showed a slight increase of 0.2 in the M^2 relative to the incident beam. Obtaining higher efficiency combining can be achieved by a number of improvements. The first is more precise alignment of relative tilt angles and grating periods to obtain flatter spectral responses. Secondly, the beam combining setup can be improved to achieve better overlap, more equal incident powers, better metrics for determining zero fringe, and most importantly, computer control of the PZTs. Constructive interference for combining was obtained by hand and iteratively adjusting the phase of each arm until a maximum combined signal was obtained. This method was time consuming and made consistent results difficult to

obtain. Implementing a passive coherent beam combining setup would also alleviate many of these alignment issues. Regardless, proof of concept has been established that this device can be used as a high efficiency coherent beam combiner.

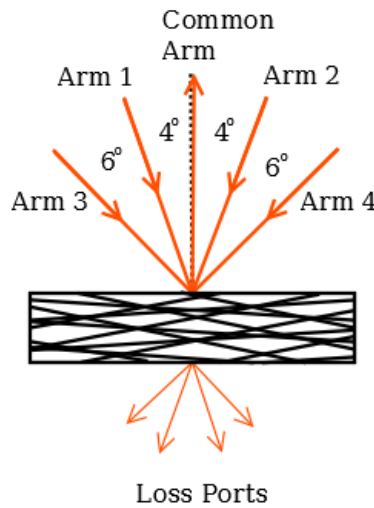


Figure 50: The design for a new multiplexed RGB for CBC targeting better alignment and equality of grating strength.

These limitations have been addressed by recording a new 4x RGB for CBC to improve upon the results presented in Figure 48. The design of the new device is presented in Figure 50. Precision alignment during the recording process provided much better alignment between individual gratings which have been recorded with equal strength. Obtaining equal grating strengths was achieved by modifying the dosage schedule to: 0.1678 J/cm^2 , 0.1763 J/cm^2 , 0.1774 J/cm^2 , and 0.1785 J/cm^2 for each subsequent recording. These values are used to address an increasing absorption level of the recording wavelength during the recording process. Due to the changing absorption during exposure, the first recording receives a higher dosage relative to later

recordings if the same incident dosage is used. The result is that the first recording is shortest and, for larger numbers of multiplexed gratings, the first recording is the only one that varies significantly from the others. In this case there is an increase of 6% in the dosage between first and second recording and the last three recording use essentially the same dosage levels. Characterization after development showed that each grating had a RIM of $115 \text{ ppm} \pm 5 \text{ ppm}$ producing excellent equality of grating strengths.

Based on the previous spectral response of multiplexed RBGs, the target for angular alignment of each individual grating was 0.02° . To achieve this precision, care was taken to precisely control the periods of each grating since the recording stages experience some small but measureable drift after initial alignment. This diligent alignment produced a correct combination of tilt and grating period to align the individual gratings for CBC within the tolerance. The spectral response as a coherent splitting device at the best overall angle of alignment is shown in Figure 51. In this figure, the grating thickness is 7.8 mm and with a RIM of 115 ppm, each grating individually has a DE of 98%. Even with well aligned gratings, and very low transmission at resonance, the spectral of the reflected arms is not an ideal flat top response. To further improve the performance of the device alignment, the grating thickness was reduced to the minimum thickness in order to achieve 99% combining efficiency. This minimum thickness depends on the RIM of each grating and the number of multiplexed gratings. Using CWT it has been shown that the minimum necessary efficiency for an individual grating in CBC is defined by Eq. 32 where N is the number of multiplexed reflection gratings for CBC [111]. When this minimum condition is met, the theoretical combining efficiency will be $>99\%$.

$$DE_{\min} = \tanh^2\left(\frac{3}{\sqrt{N}}\right) \quad (32)$$

By reducing the thickness of the device, the angular acceptance of each grating will increase, this will allow the alignment tolerance to increase even further while still maintaining high combining efficiency. The grating was thinned to 4.1 mm such that each individual grating had an efficiency of 81%. This value is slightly below the desired value of 82% for four reflection gratings, so slightly less than 99% combining efficiency can be expected from this device. The spectral response of the device at the ideal minimum thickness is shown in Figure 52. Less than 2% of light is being transmitted such that 98% combining efficiency can be expected. The reflection spectrum of each arm has a flat top and the reflection efficiency of each arm is $25\% \pm 1\%$. Therefore, to achieve best performance in terms of alignment, it is necessary to control the precision of the recording as well as design the device to operate at the minimum acceptable thickness.

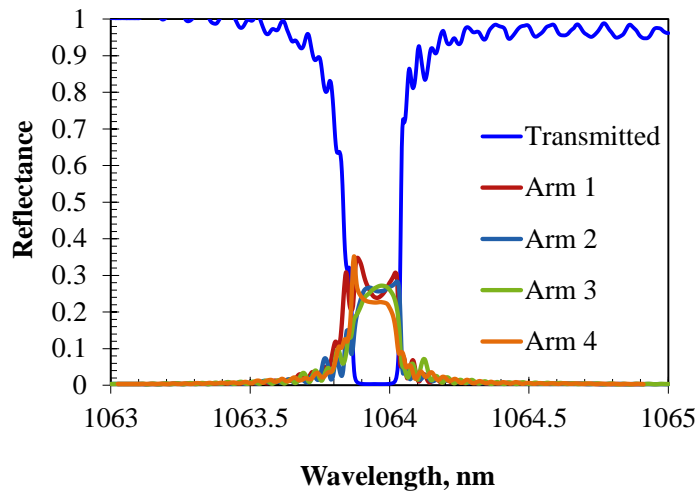


Figure 51: Overmodulated multiplexed RGB for CBC used as a splitter. Total reflection efficiency is high, but reflected arms do not produce flat top spectral response due to higher detuning selectivity for thicker RBGs.

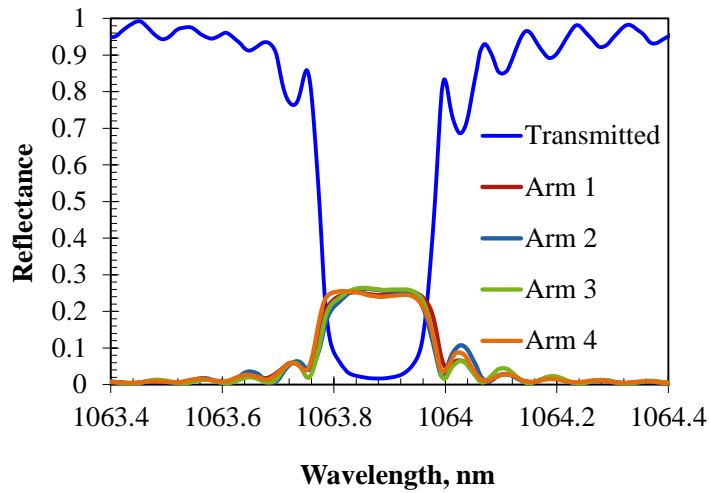


Figure 52: The spectral response of a multiplexed RGB for CBC measured as a splitter at a thickness that meets the minimum individual DE requirement.

To provide further experimental verification of the minimum necessary strength of each grating, the device was further thinned down to 2.1 mm such that the efficiency of each grating is now 40%. The spectral response is shown in Figure 53. The reflection spectra of each arm are nearly indistinguishable due to excellent overlap and equal efficiency. The combining efficiency has dropped to 78%.

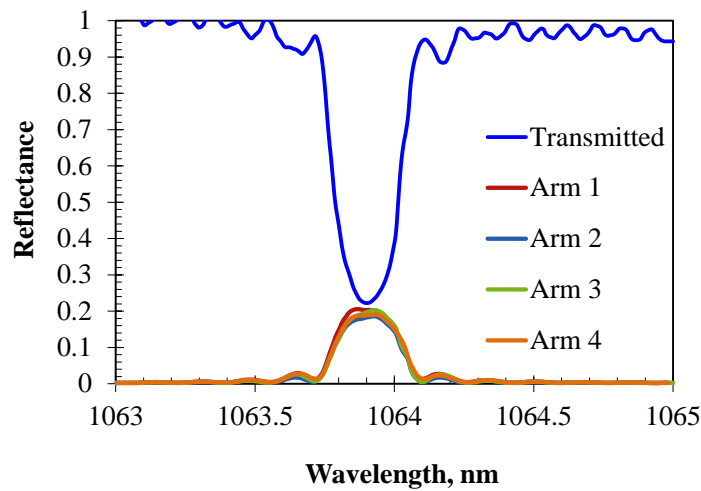


Figure 53: An undermodulated multiplexed RBG for CBC measured as a splitter. The expected combining efficiency is low, but overlap of the spectral response in each reflected arm is very good.

In conclusion, a 4x RBG for coherent beam combining has been demonstrated to give approximately equal splitting into four different channels when the correct conditions are met. The device has been used to efficiently recombine a low-power laser in an active coherent beam combining setup with combining efficiency of 90% with preservation of M^2 beam quality in an active coherent beam combining setup. To improve performance, a new multiplexed grating was recorded to address the relative alignment of the gratings and equalize the strength of each

recording. The design of the grating thickness was also used as a parameter to loosen tolerances of angular alignment to a level that could be achieved with current recording techniques. The device at the optimum thickness showed close to ideal performance with equal splitting between channels, low transmission losses, and flat top performance. Using this device in an active or passive coherent beam combining system is expected to produce excellent combining efficiency with a more reliable and predictable alignment than previous demonstrations.

5 MOIRÉ BRAGG GRATING

The moiré Bragg grating (MBG) is a purely interdependent type of multiplexed grating with unique spectral filtering capabilities. Most generally speaking, the multiplexing that occurs in the MBG is such that a secondary spatial profile is created within the grating. The term moiré is used in optics to refer to the superposition of two periodic structures such that an envelope pattern is created. An example of a moiré pattern is shown in Figure 54 which consists of two overlapping sinusoids of different periods. By eye, a secondary pattern is visible due to the interference of the two sinusoids and corresponding white space. This is also frequently referred to as a beat frequency that occurs due to the superposition of two closely spaced and superimposed frequencies.

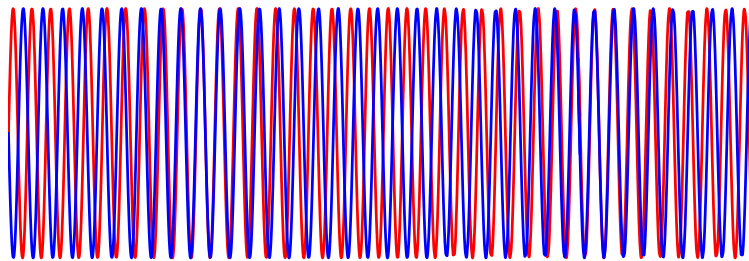


Figure 54: The moiré pattern formed by two overlapping sinusoids with slightly different periods. The points of constructive and destructive interference produce a secondary visual pattern.

The envelope pattern that occurs in the spatial profile of an MBG generates very unique features in the grating's spectral response. The spectral features of the MBG have been demonstrated in fiber as covered in the review section on multiplexed VBGs on page 34. These types of gratings require enough material thickness to realize the effects of the secondary pattern and therefore fibers are well suited to demonstrate the filtering properties. PTR glass is a material that is equally well suited for these sorts of physical thicknesses, making it an exceptional material for demonstrating the filtering capabilities of the MBG for free space applications.

The MBG is a subset of a class of gratings that are referred to as phase-shifted gratings (PSGs). These types of gratings consist of a single Bragg grating structure that is interrupted by discrete phase shifts which induce useful features into the grating's spectral response. Typically, PSGs contain a π shift in the center of a Bragg grating, though devices which contain multiple fractions of π shifts have been demonstrated for different applications [112]. The phase shift may be created in a number of ways including, using typical thin grating recording techniques discussed on page 20.

Until recently, these recording methods have only been applied to the creation of PSGs in fibers. Excellent results for fiber based MBGs have recently been reported using a point by point writing technique. The study reported bandwidths of less than 1 pm with a rejection ratio of -35 dB [113]. For filters in used in free space beam propagation or large aperture applications, PSGs recorded in a bulk media such as PTR must be used, and sequential holographic exposure to produce a moiré pattern is one of the methods for recording such filters. In the moiré method,

two collinear gratings with slightly different periods are recorded in sequence. Mathematically, the RIM of such a recording is the addition of two sinusoids which can be simplified to the product of two sinusoids; one with a spatial frequency that is the average of the two frequencies and one that has the beat frequency between the two gratings as shown in Eq. 33.

$$\begin{aligned}
 n(z) &= n_0 + n_1 \sin(2\pi Q_1 z) - n_1 \sin(2\pi Q_2 z) \\
 &= n_0 + 2n_1 \sin(2\pi Q_{ave} z - \pi/2) \cdot \sin(\pi \Delta Q z)
 \end{aligned}
 \tag{33}$$

Where n_1 is the refractive index modulation of each individual recording, n_0 is the background refractive index and Q is a spatial frequency. The subscripts indicate the number of the recording ΔQ is the difference of Q_1 and Q_2 and Q_{ave} is the average spatial frequency between the two. The physical appearance of this pattern is shown in Figure 55. The resulting pattern produces π phase shift in the high frequency modulation at the zeros of the envelope pattern. By processing the MBG after recording, the exact position and number of these phase shifts can be controlled within the volume and specific filtering properties can be achieved. In this section, the filtering properties of an MBG will be explained and modeled, the methods that have been developed to determine the location of the envelope zeros will be shown, and experimental results from MBGs in PTR for use in laser systems will be demonstrated.

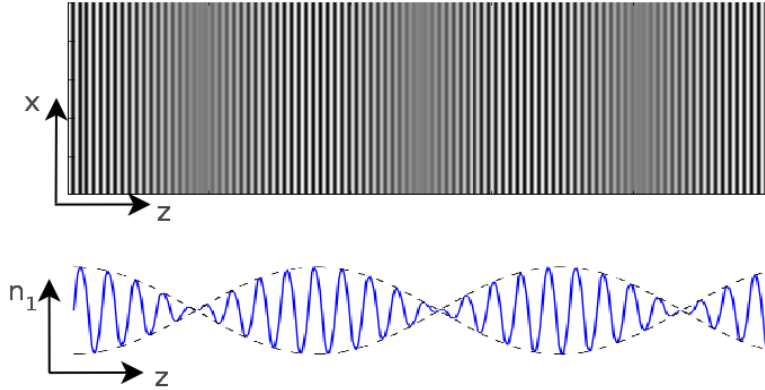


Figure 55: A simulated image of a moiré Bragg pattern is shown above and the corresponding RIM is shown below. At the zero points of the RIM, a phase shift can be seen in the high frequency modulation.

Theoretical Description

The origin of the MBG in PTR glass came about from attempts to create a Fabry-Perot cavity using RBGs as mirror elements [114]. The goal being, to use the narrow reflection bands of the reflecting Bragg gratings to select only a single transmission band of the Fabry-Perot spectrum, resulting in an infinite free spectral range. The moiré Bragg grating was the next logical step in extending this technology to a monolithic FPE. As such, the performance of this device can be described in two ways. The first is as by applying coupled wave theory to this structured Bragg grating and the second is to decompose the MBG into elements of a Fabry-Perot etalon and use the equations from page 6 to describe the performance. While CWT is able to accurately predict the performance of a given filter, it does not necessarily provide an intuitive method for analyzing these complex VBGs. For the purposes of design and analysis of optical components,

it is convenient to obtain simple first order approximations for device performance and in these cases the formulation based on the FPE equations is preferred.

Of the two approaches, the use of coupled wave theory provides the most accurate results and gives the best description of the spectral response. Various implementations of CWT, such as the matrix methods [19, 88], and recursion methods [115] have been proposed. These methods, when applied to a grating that has axially varying RIM and phase shifts, require breaking the grating into a large number of slices and calculating the response as a single, uniform grating. A characteristic matrix or equation is assigned to the response of each slice and the final response can be calculated from the interactions of all the slices. The approach implemented for precise modeling in this dissertation uses a recursive application of an analytical CWT solution for the reflectance of each slice. The inputs for each slice are RIM, phase, and reflectivity of the previous plane [116]. The equation that characterizes a slice is given in Eq. 34.

$$r(-l) = \frac{1 + r_0 \left(\frac{\xi}{v} + j \frac{\sqrt{v^2 - \xi^2}}{v} \coth v \right)}{r_0 \left(\frac{\xi}{v} - j \frac{\sqrt{v^2 - \xi^2}}{v} \coth v \right)} \quad (34)$$

Where r is the complex reflectivity coefficient of a given slice of length l and r_0 is the reflectivity of the preceding section. The inputs to this equation are the dimensionless coupling parameter v from Eq. 12 and the dimensionless detuning parameter ξ from Eq. 13. Starting from the back side of the grating, the reflectivity of each slice is calculated using the previous slice as an input until

the reflectivity is calculated for the entire device. The absolute value squared of the reflectivity gives the reflectance spectrum. The benefit of using this modified formulation is that it allows the angle spectrum of the MBG to be determined as well because the detuning parameter includes both angle and wavelength detuning.

This model can be used to describe an MBG with arbitrary period, envelope period, inequalities of RIM, total length, and location envelope pattern within the device. Because of this versatility it is extremely useful in matching measured spectrum with theory in order to characterize the grating parameters that were achieved. Because the CWT approach is able to handle such complexity, it has a drawback in that it does not provide an intuitive understanding of how the grating spectrum will be affected by changing of the parameters. To model an MBG in an intuitive fashion, the approach of decomposing the grating and describing it in terms of the Fabry-Perot etalon results in a simple to understand model that is useful for designing MBGs. The fundamentals of this approach were used by Barmenkov [117] and are the obvious extension of experiments using RBGs to create Fabry-Perot cavities.

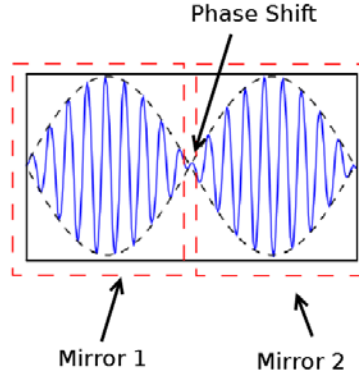


Figure 56: A single period of the moiré envelope is decomposed into the two mirrors and cavity analogous to a Fabry-Perot etalon.

The MBG comprised of the refractive index pattern $n(z)$ from Eq. 33 can be modeled as a Fabry-Perot etalon by spatially decomposing the MBG into two mirrors on either side of the π phase shift induced by the null point of the envelope. A typical MBG is shown decomposed in Figure 56. The mirrors of the FPE are formed by apodized Bragg gratings on either side of the phase shift. The cavity is formed by the phase shift as well as the phase induced by the reflection from the individual apodized grating mirrors. The reflectance coefficients of the mirrors can be calculated from the peak reflection at resonance formed by a simple VBG given by Eq. 35 (a modified version of Eq. 15).

$$R = \tanh^2 \left(\frac{t/2 \cdot a \cdot \pi \cdot 2n_1}{\lambda_0} \right) \quad (35)$$

Here $2n_1$ corresponds to the maximum induced refractive index modulation from both recordings, λ_0 is the central resonant wavelength in air, t is the total thickness of the device and is divided by 2 because each mirror occupies only half of the total device thickness, and \tanh is

hyperbolic tangent. The factor a is a scaling of the length due to the apodization of the grating mirrors by a sinusoid as described in [118] which, for any multiple of the half period of a sinusoid, is 0.6366.

The cavity length of the FPE resonator is formed by the phase induced by reflection from the mirror gratings as well as the π phase shift. The phase induced by a reflecting Bragg grating can be written in terms of design parameters by approximating the reflectance of a grating to be constant within the reflection band of the grating. This is a good approximation for strong reflecting gratings. The derivation follows [117] but retains the dependence on wavelength. The $\kappa=2\pi n_1/\lambda$ and $\chi = 2\pi n_0 \Delta\lambda/\lambda^2$ are the coupling and detuning coefficients. The approximation for the phase of the reflectivity ϕ , for a single mirror given in Eq. 36 will be used.

$$\begin{aligned}
\Phi &= -\tan^{-1} \frac{\sqrt{\kappa^2 - \chi^2}}{\chi \tanh \sqrt{\kappa^2 - \chi^2} t} \\
&\approx -\tan^{-1} \frac{\tanh^{-1} \sqrt{R} / t}{\chi \sqrt{R}} \\
&= -\tan^{-1} \frac{2n_1 \lambda_0}{2n_0 \sqrt{R} \Delta\lambda}
\end{aligned} \tag{36}$$

The physical phase discontinuity in the high frequency pattern must be converted into a cavity length by calculating the magnitude of the phase shift in terms of the resonant wavelength. Using the Bragg condition (Eq. 10), the period of the high frequency grating can be related to the resonant wavelength. For resonance occurring at normal incidence the ratio of grating period to

resonant wavelength is 2:1, hence a π phase shift in the period corresponds to a cavity of length $\lambda_0/4$.

Using the relations for converting the recording parameters into FPE components, the transmission spectrum of the FPE system can be obtained using Eq. 37 which is an expanded version of the transmission discussed in Eq. 4.

$$T = \frac{(1 - R_1)(1 - R_2)}{(1 - \sqrt{R_1 \cdot R_2})^2 + 4\sqrt{R_1 \cdot R_2} \sin^2 \left(2 \left(\beta L_0 + \frac{(\Phi_2 + \Phi_1)}{2} \right) \right)} \quad (37)$$

Here R_1 and R_2 correspond to the strengths of the two Bragg mirrors, L_0 is the effective cavity length formed by the phase shift and Φ_1 and Φ_2 represent the phase-shift upon reflection generated by the Bragg mirrors. This simple model can be used for the first order design for the transmission resonance of an MBG in terms of the design variables such as length and refractive index modulation.

In order to complete the model for the spectral response of a FPE, the spectral dependence of the reflection from a Bragg mirror must be accounted for. The diffraction efficiency is calculated separately and the total response of the MBG is calculated by $T^*(1-DE)$. Inputs for the diffraction efficiency use the full apodized thickness $a \cdot t$ and the total index modulation $2n_I$. A comparison of these results to the results obtained through a full couple wave analysis

following [19] is shown in Figure 57 . Excellent agreement is demonstrated around the area of resonance and variations only begin to occur in the side lobes.

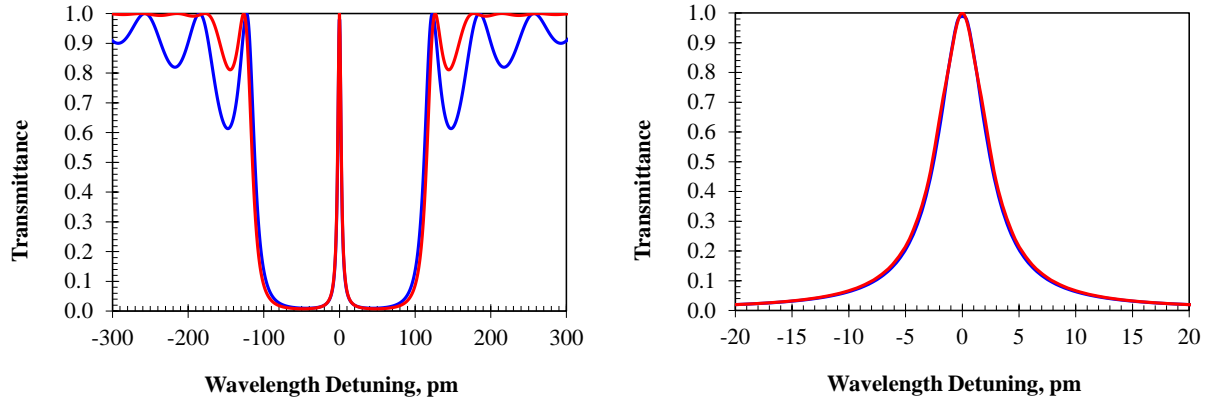


Figure 57: A comparison of the FPE method (blue) and full couple wave analysis (red) of an MBG. Left shows full spectrum and right shows just resonant transmission. Grating parameters are: envelope period = 7.5 mm, grating thickness = 7.5 mm, $n_1=n_2=130$ ppm, $\lambda_0=1064$ nm, resulting in a transmission bandwidth FWHM of 5 pm.

Using the FPE model, the filtering capabilities of the phase shift grating can be determined and design curves can be calculated. Assuming a MBG with a length equal to the period of the moiré envelope, and a phase shift occurring at the center of the grating, the pertinent design parameters are the grating envelope period and n_1 . The transmission bandwidth from FPE model simulations is shown for the various values of the design parameters in Figure 58. Other parameters such as the rejection bandwidth and the peak reflectance can also be obtained using this model.

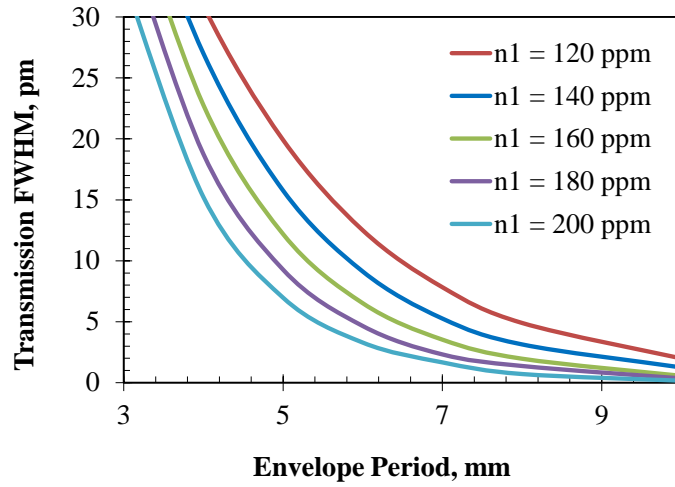


Figure 58: A design curve showing transmission bandwidth for moiré Bragg gratings. Design parameters are the period of the moiré envelope and the refractive index modulation.

To verify this model, a volume MBG was recorded using sequential holography. The spectrum of this MBG is shown in Figure 59. The device parameters are: a resonant wavelength of 1064.34 nm with an envelope period of 3.27 mm and $2n_1$ of 420 ppm. The transmission bandwidth is measured to be 25 pm and the peak transmission is 93%.

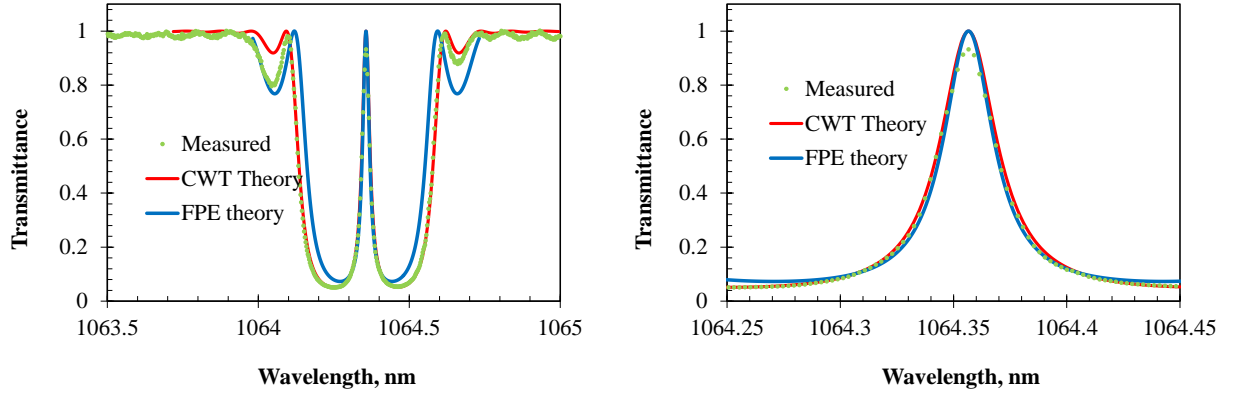


Figure 59: An MBG demonstrating above 90% transmission. Green dots show measured results, Blue shows FPE theory and Red is coupled wave theory. The primary cause of reduction of transmission efficiency is the difference of the reflectance of each cavity mirror.

The origin of the differences between theoretical and measured results is due to the FPE theory working best for high finesse systems. This occurs when the grating strength of the individual mirrors is high, such as the case in Figure 57. For low finesse systems, the model still accurately describes the transmission resonance, but there are small differences in the width of the rejection band. For the design of the filtering properties of an MBG, these results show that the spectral response of an MBG obtained by FPE approximations is sufficiently matched to the more rigorous matrix based CWT approach. Both models have been applied to the measured spectrum of an MBG recorded in bulk material and excellent agreement was shown between the shapes and bandwidths of the transmission peaks.

Measurement of Axial Profile

The most important aspect of recording an MBG with good performance in a bulk medium is the centering of the phase shift within the volume. The effects of shifting this location will be covered in the next section. This section is devoted to the various methods that have been applied to determining the axial refractive index profile by measurement in the transverse direction. Here the axial direction refers to axis of measurement, i.e. the z direction in Figure 55 and the x axis is the transverse direction in which characterization of the profile occurs. All methods relate to the differences between the regions with large refractive index modulation versus the areas with low modulation (the zero points of the envelope). While both regions receive the same spatially averaged dosage, the presence of the modulation changes some of the properties of PTR glass as compared to an area with a uniform flood exposure, but the mechanisms for these differences is not well understood at present. Therefore, these measurements are not only important to the characterization of MBGs but they also provide an excellent way to compare uniform refractive index change to the refractive index modulation in a grating. The properties of PTR that can be investigated are the changes in background index, absorption, scattering, photo-darkening and diffraction efficiency. To provide an example for these measurements, an MBG was recorded with target central wavelength of 1064 nm, resonant wavelength separation of the two gratings of 150 pm, and $n_1 = n_2 = 210$ ppm. The glass dimensions are 25 mm x 25 mm x 6 mm with the grating vector along one of the 25 mm lengths. This grating was used to demonstrate the various quantities that can be tested for determining the refractive index profile. A photo of the grating after development is shown in Figure 60 and evidence of photo-darkening is clearly visible.

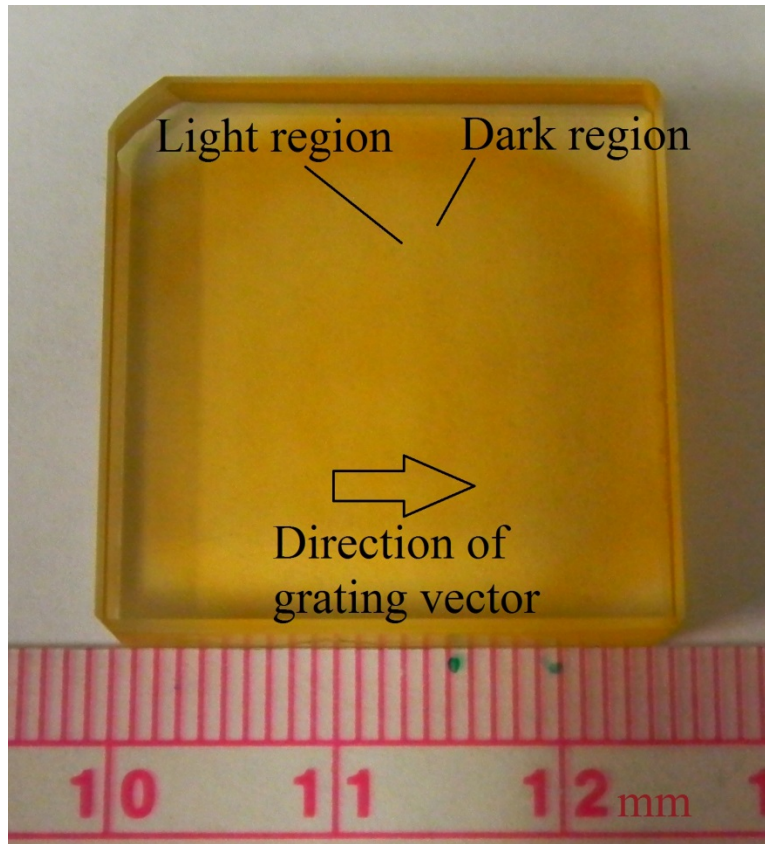


Figure 60: An image of an MBG used for demonstrating methods for determining the envelope profile. Photo-darkening of different regions is evident.

After observing photo-darkening, the next simplest property to analyze is the combined losses through the grating by monitoring the transmission through the sample when probing orthogonal to the grating vector as shown in Figure 61. The result of a scan across the MBG is shown in Figure 62. There is some modulation of the transmission, but actual determination of peaks and valleys of this data is difficult due to the low signal to noise ratio. Improvements to this method might be achieved by looking directly at the diffuse scattering or by blocking the ballistic light when measuring in transmission if more detailed understanding of the loss mechanisms is

desired. For now, the current method provided enough resolution to make a rough mapping of the peaks and valleys of the combined losses in the MBG.

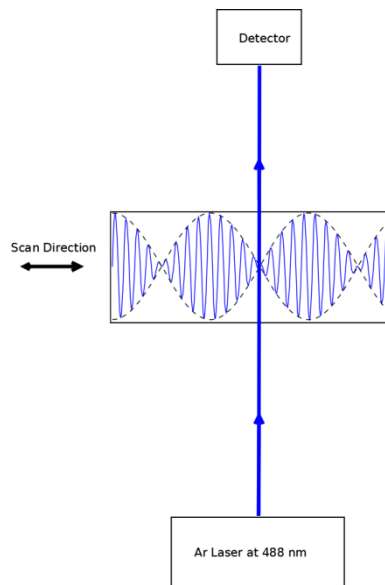


Figure 61: Setup for testing the axial profile of an MBG using losses.

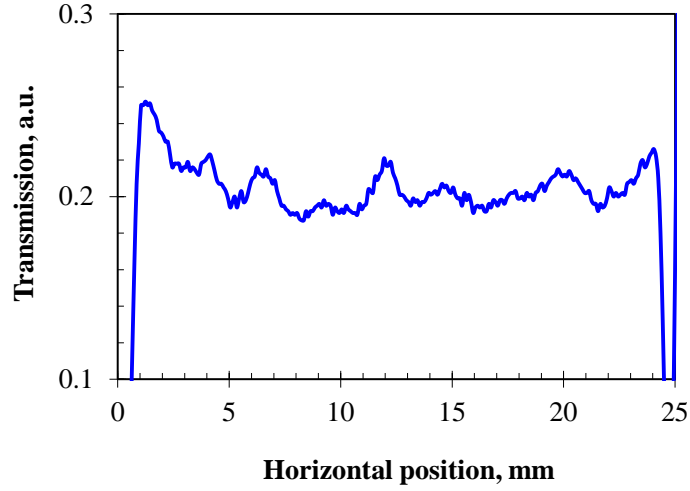


Figure 62: The transmission through the transverse direction of the MBG for measuring spatially dependent combined losses.

The next method was to look at the modification of the background index n_0 in the MBG. A change in the background index results in a different phase incursion in sections. Therefore, by placing the sample in a Zygo interferometer and measuring the double pass phase incursion across the sample face, the relative change in background index can be inferred. The map of the phase from this measurement is shown in Figure 63 and line profile near the center is shown in Figure 64. Also note that the phase profile of the reflection from one of the surfaces was measured to rule out the possibility that the phase incursion is due to surface relieve on the sample. It is clear that, through a double pass of the 6 mm thickness, the background index varies between regions of high grating modulation and low modulation and the background refractive index difference is approximately 5 ppm.

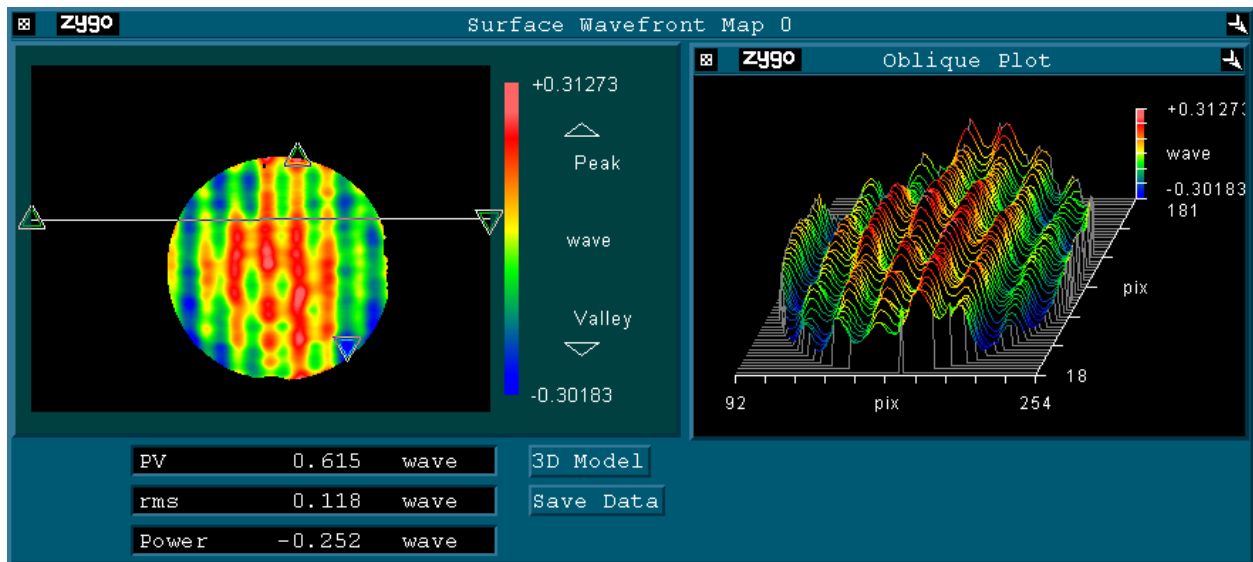


Figure 63: The wavefront data of double pass transmitted light at 633 nm through the face of an MBG.

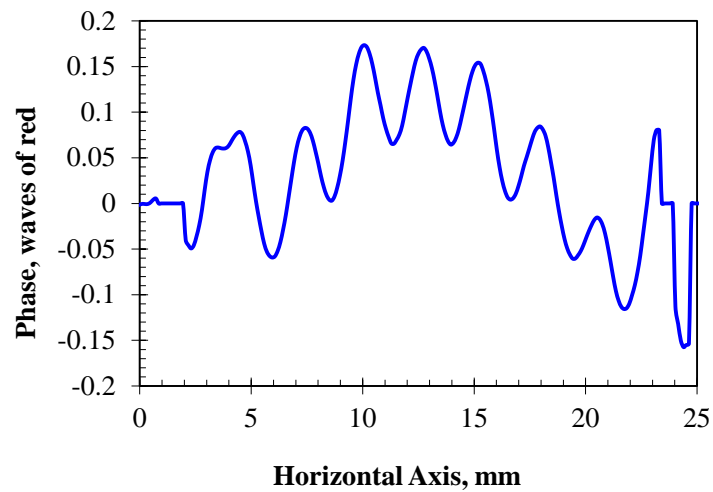


Figure 64: The line profile near the center of the wavefront data taken with the Zygo interferometer.

The final method for measuring relies on the use of the MBG in the transverse direction as a transmitting Bragg grating by probing the 25 mm x 25 mm face with visible laser with a small beam radius at an angle such that it is diffracted from the grating structure as shown in Figure 65. In the form presented, this method will be called the transverse diffraction efficiency method as the diffraction is being generated in the plane that is transverse to the designed diffraction plane. Areas of high index modulation will create a strong diffraction and areas with low modulation, such as the zeros of the envelope, will create a weak diffraction.

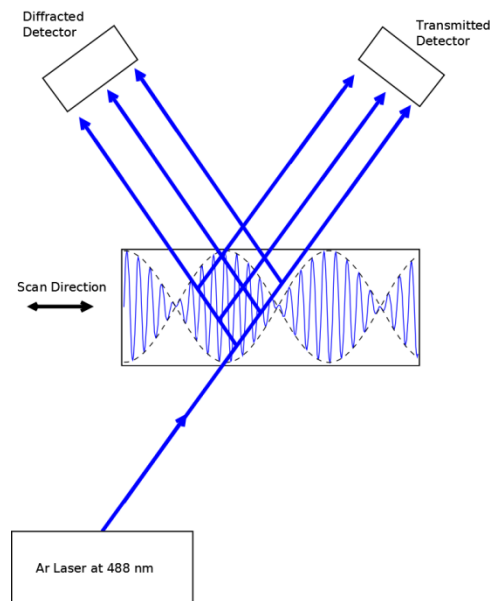


Figure 65: Using diffraction to measure the transverse profile of an MBG. Due to the large thickness of the grating and angle of incidence, there is a wide cone of diffraction that occurs.

This process is greatly complicated by the fact that the probe beam traverses the structure at a large angle and through a thickness that creates a large cone of diffraction as shown in Figure 66.

This means that the diffracted light within this cone encounters a variety of different refractive index modulations as illustrated by the many rays in Figure 65. For this reason, a laser of the lowest wavelength and hence the lowest Bragg angle according to Eq. 9, is desirable for this test.



Figure 66: The cone of diffraction is able to be imaged from the scattering of blue light when measuring an MBG in a transmission grating geometry.

A blue argon ion laser operating at 488 nm was used to probe this MBG with an angle of incidence of 42° . The choice of a short wavelength laser improves the ability to isolate diffractive regions of interest. Regardless, if the envelope period has a length of under approximately 5 mm, the cone of diffraction will still encounter many different index modulations. To address this, the scan can be completed at both the positive and negative angles of incidence as depicted in Figure 67. In the left portion of the figure, the diffraction efficiencies measured at the + and - angles will be unequal because of the different paths traversed, but in the right hand side of the figure the paths are symmetric and the same diffraction efficiency can be achieved. This method allows accurate determination of the peaks and minima of the RIM in the MBG.

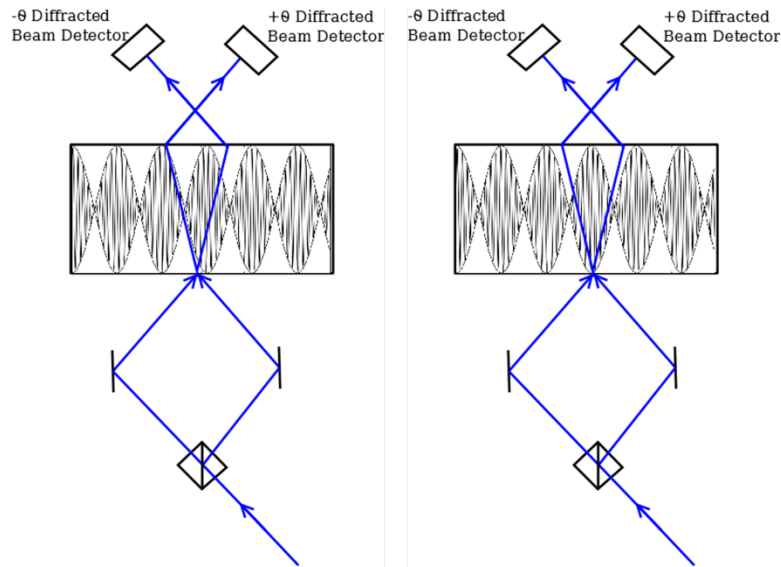


Figure 67: Scanning an MBG for diffraction with positive and negative angles of incidence allows maxima and minima to be located easily since the diffraction in the two arms will be equal at these points as shown here.

A representative scan across the grating with both positive and negative angles is shown in Figure 68. From such scans, the locations of equal diffraction efficiency represent minima and maxima. The general shape of the curves gives an indication of which points are maxima versus which are minima but this depends strongly on the period of the envelope, the maximum refractive index modulation, and the thickness of the grating in the transverse direction. The ambiguity of this measurement and the reliance on the experience and ‘feel’ of the operator make it less than ideal as a general measurement tool for MBGs. Yet, very accurate and repeatable results have been achieved using this method to determine the location of the envelope zeros within hundreds of microns. The accuracy of this, and all previously mentioned techniques, depends on accurately locating the envelope’s zeros with respect to some physical reference such as the edge of the glass. The strength of this method is that scanning a small probe beam across

the face of the grating provides easily identifiable transmission features regarding both the zeros as well as the physical borders of the device as can be seen at the edges of Figure 68. The processing of these signals is the primary method for determining the envelope zeros in the MBGs presented in subsequent sections.

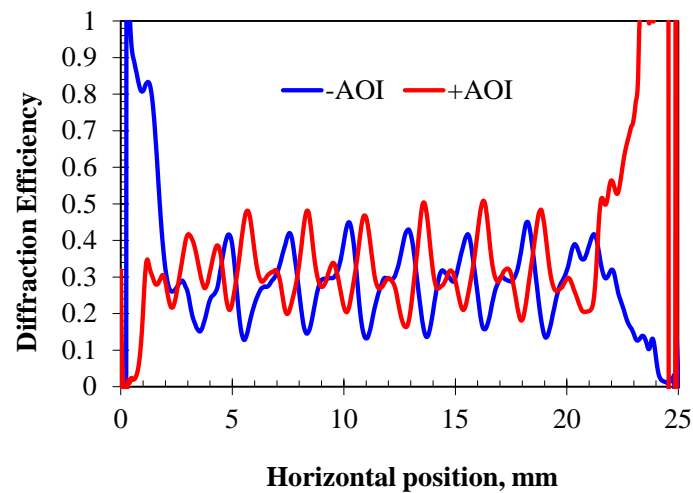


Figure 68: The diffraction efficiency of an MBG measured as a transmission grating in the transverse direction. Using the symmetry of the scans at positive and negative angles of incidence (AOI) allows the locations of the maxima and minima of the envelope pattern to be determined.

The ambiguity of the measurements of axial profile using diffraction efficiency coupled with the difficulty in modeling a grating system that occupies a diffraction cone of significantly varying RIM encouraged an investigation into an alternative geometry for such a measurement. The result of this inquiry is shown in Figure 69. This variant of the transverse diffraction efficiency method uses an aperture to only look at the primary ray of transmission. The goal of this measurement is to provide a much simpler system for modeling in future investigation of MBG

behavior because only the depletion of the primary transmitted ray needs to be accounted for as opposed to the intricate coupling of the many rays being generated in the diffracted and transmitted orders. Practically speaking isolation of only the primary transmitted ray is difficult, but for the subsequent measurements, an iris with a similar diameter to the probe beam was used to aperture the transmitted orders. A representative scan from this measurement is shown in Figure 70. Compared to the scan from the full transverse diffraction efficiency method, this measurement produces much simpler profiles but still requires a scan at both the positive and negative angles of incidence. So while the measurement technique does not provide additional resolution for processing the MBG, it does provide a simpler system for modeling diffraction through the transverse direction.

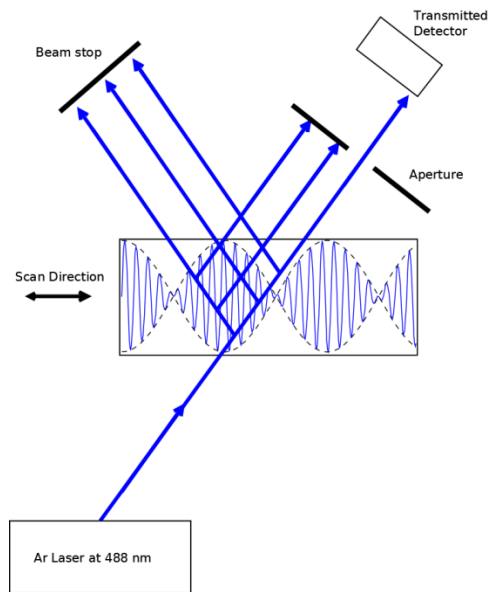


Figure 69: An alternative diffraction measurement for determining the axial profile of an MBG utilizing only the primary transmission ray.

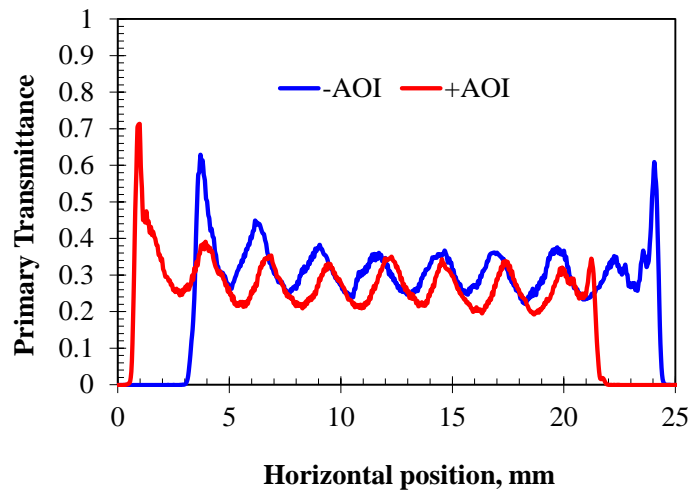


Figure 70: The signal from an axial scan of an MBG using only the primary transmission ray to determine the locations of the envelope zeros.

The results from these various transverse MBG measurements across the 25 mm x 25 mm face of the MBG have been compiled in Figure 71. The points indicate locations of the envelope zeros. These points correspond to locations of low RIM, higher losses, lower background refractive index, and higher photodarkening. Full scans across the aperture at multiple vertical locations were completed for measurement systems that have been automated, for other tests that have not been automated only a single vertical line profile was analyzed. Excellent coincidence between the various measurement techniques is evident. Measurements made with the Zygo interferometer appear slightly shifted. This is due to the difficulty of obtaining an appropriate reference surface and scale in the data which was obtained. In future interferometric measurements this can be addressed by scribing a thin reference into the transverse face for more accurate results. The aggregation of these measurements was used to determine the locations for cutting the MBG to create a device with a phase shift located in the center of the thickness. The

spectral transmission through this processed MBG is shown in Figure 72. A narrow transmission peak with a transmission value of 85% and a FWHM bandwidth of 10 pm was obtained. These results fit well with theoretical predictions for a well centered phase shift given the recording parameters. By producing this narrow spectral transmission, the effectiveness of all the measurements presented in this section has been demonstrated. Additionally, interesting material dynamics of PTR glass have been experimentally demonstrated in a controlled manner. Differences between areas of uniform exposure and areas of sub-micron period gratings show dramatically different properties. Namely, the presence of lower transmission losses, lower photo-darkening, and higher background refractive index have been revealed in regions of high RIM.

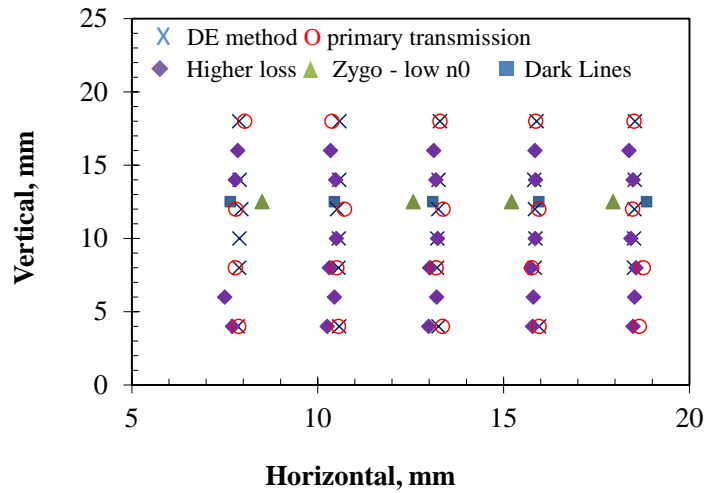


Figure 71: A summary of the measured locations of envelope zeros of an MBG using different transverse measurement techniques.

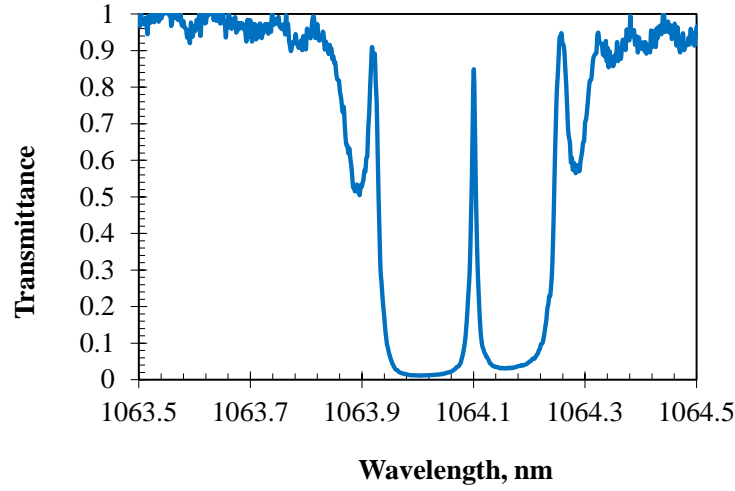


Figure 72: The spectral transmission of the MBG that was cut to produce a phase shift in the center of the volume using the aggregated results of the transverse measurement techniques.

The transverse measurement methods have been shown to produce accurate measurements of the envelope pattern, but are still a fundamentally time consuming endeavor to produce extremely accurate results. To bypass this complexity, an alternative processing method is proposed. This method avoids the need to determine the exact location of zero points and at the same time reveals an interesting functionality of free space MBGs. This variant of the MBG filter allows for a tunable spectral bandwidth. Such tuning is achieved by varying the axial location of the phase shift as a function of the transverse position on the device, see. Figure 73b. The MBG after recording is processed such that, across the aperture of the device, the position of the zeros of moiré envelope corresponding to π -phase shift will move linearly along the axial direction and the envelope will vary from a sine to a cosine profile. The processing requires only a knowledge of the period of the envelope and not the exact positions of the envelope zeros. The complexity and accuracy required for these steps is significantly reduced from the previously mentioned

methods and allows MBGs to be rapidly characterized. The additional benefit which will be discussed here is the opportunity to confirm the theoretical calculations of the effect of a shift of the envelope pattern within the media. In terms of applications, this provides a unique advantage over phase shifted gratings recorded in fiber because aperture dependent tuning can be built into the device, as well as a better tolerance to high power radiation.

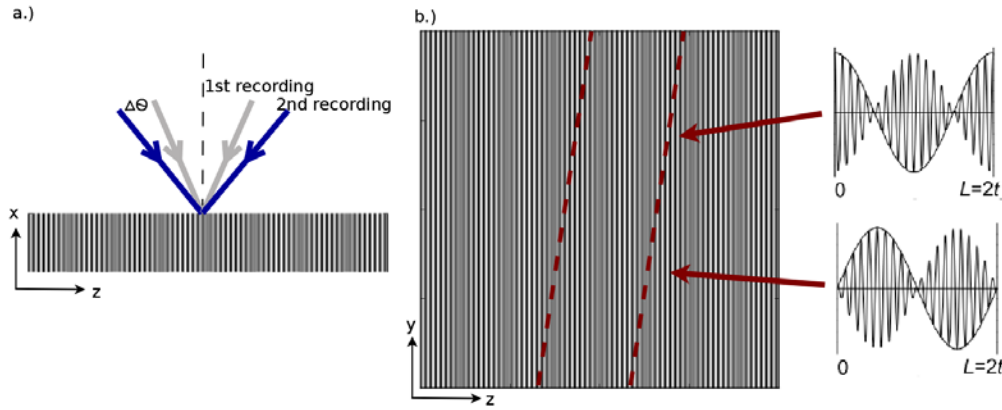


Figure 73: Side view of the recording of an MBG in PTR (a) and a top view of an unprocessed grating (b) along with the cutting locations for producing a tilted MBG with sine and cosine envelope profiles.

To demonstrate this concept a 25 mm x 25 mm x 6 mm sample of PTR glass was exposed with a first interference pattern designed to give resonance at 1063.86 and a second interference pattern designed to give Bragg resonance at 1064.10 nm. After development, the sample was measured to determine the period of the grating envelope of $L = 3.27$ mm. The grating was cut along the dashed lines shown in Figure 73b. These lines are at approximately 5° with respect to fringes of refractive index modulation. The thickness is equal to the envelope period, L . This cut angle allows the envelope profile to vary from a sine to a cosine within a 20 mm aperture.

The moiré grating was tested using a tunable laser source with sub-picometer resolution. Light was incident parallel to the grating vector and a photodiode was used to measure the irradiance of light being transmitted through the MBG as the wavelength of the tunable source was swept. Two representative spectra, taken at different points on the grating, are shown in Figure 74 for the sine profile and Figure 75 for the cosine profile of the slowly varying envelope. Theoretical spectral curves were obtained using the standard transfer matrix technique for Bragg gratings.

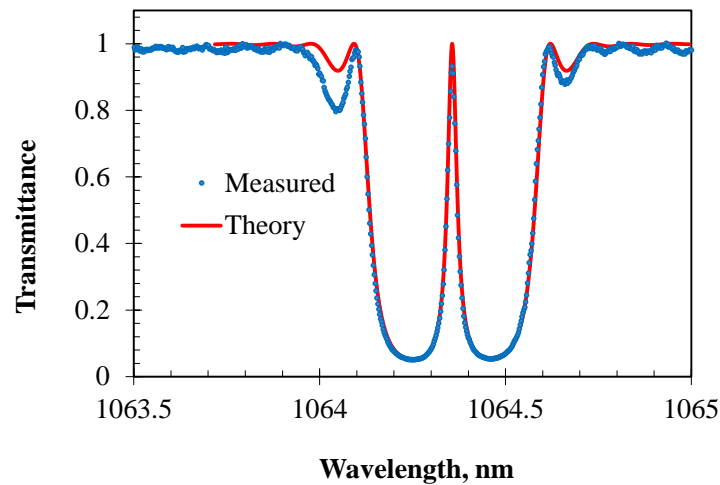


Figure 74: The transmission spectrum of an MBG obtained at the point of minimum transmission bandwidth of 30 pm corresponding to a sinusoidal envelope profile.

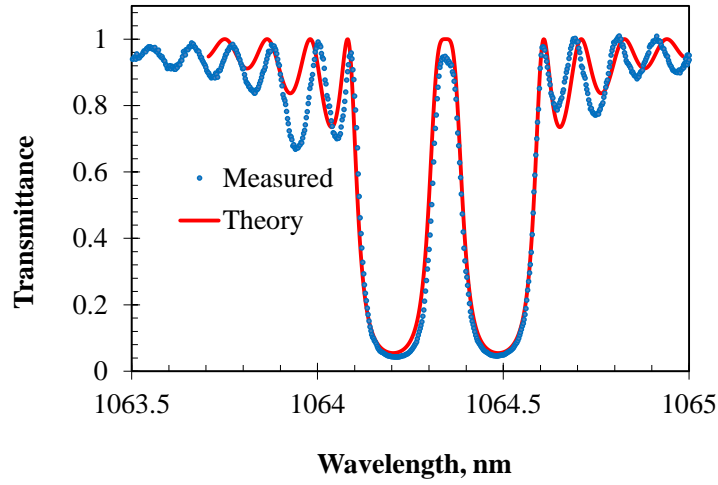


Figure 75: The transmission spectrum of an MBG obtained at the point of maximum transmission bandwidth of 90 pm corresponding to a cosine envelope profile.

Similar spectral scans were completed across the entire aperture of the grating. The important features for characterizing the filter as a function of the aperture position are bandwidth shown in Figure 76 and peak transmission shown in Figure 77. The FWHM bandwidth of the transmission peak varies across the aperture from 30 pm to 90 pm and peak transmissions of >90% are maintained.

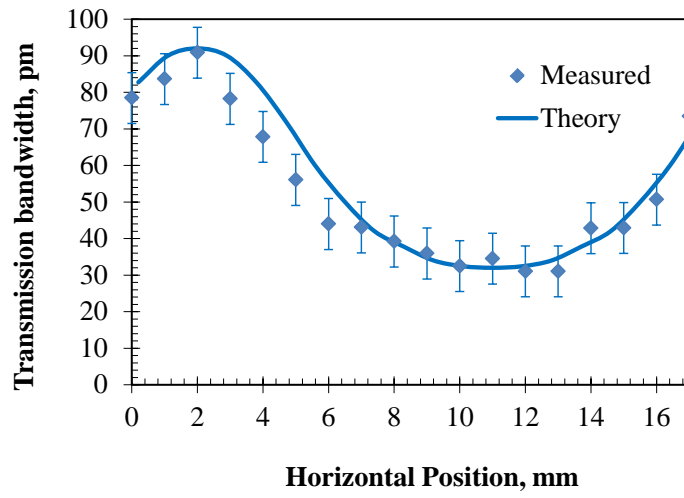


Figure 76: The FWHM bandwidth of the transmission peak across a tilted MBG shows a sinusoidal tunability with horizontal position.

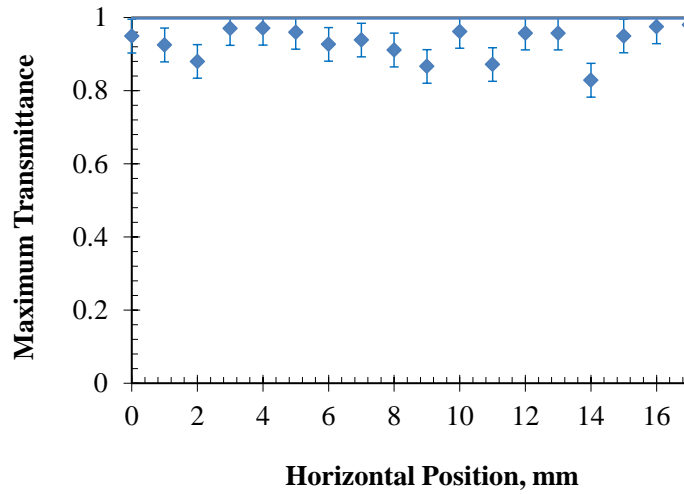


Figure 77: The peak transmittance of the MBG resonance across the face of a tilted MBG shows consistently high transmission that is unaffected by the envelope pattern.

In conclusion, the ability to vary the bandwidth of a moiré volume Bragg grating by simply translating the probe beam across the aperture of the grating has been demonstrated. The measured results match well with theoretical predictions. The resonant wavelength and peak transmission of the filter are also maintained across the face of the device indicating excellent homogeneity of the recording. This device may find useful applications in pulse shaping, mode control in laser resonators, and high-resolution spectroscopy. For development of MBGs in bulk recording material, this method provides a fast way to process MBGs and test various aspects of the device without absolute knowledge of the envelope zero locations.

Sources of Decreased Peak Transmission

A number of potential sources of error that prevent optimal performance of an MBG have been identified. Primarily, these sources of error affect the bandwidth that can be achieved and the peak transmission at resonance. Understanding the origin of these imperfections and defining tolerances for production of such devices is a task that is greatly simplified by using FPE model over a full CWT treatment. The primary concern of these studies was to increase the peak transmission that can be achieved in an MBG so that the device is able to operate in laser systems without introducing losses.

Several factors are able to contribute to a drop in the peak transmission. The critical parameters for the performance of the MBG are the centering of the envelope pattern inside the device, the total length compared to the semiperiod of the envelope and the difference of index modulation

between the two VBGs recorded. All of these factors can contribute to an inequality of the effective mirrors of the FPE. From Eq. 7, the peak transmission of an FPE depends on the equality of the mirror reflectance values. In the case of an MBG, these reflectance values will be equal for an envelope pattern that is symmetric about the phase shift or for the case where the total length is equal to the envelope period. Therefore, in order to decrease the peak transmission of the filter, the grating length must differ from the grating period and the phase discontinuity must be decentered. In the case where the reflectance between the two cavity mirrors differs by a small amount such that $\sqrt{R_1 R_2} \approx R_{ave}$, the change in transmission is given by Eq. 38. For example, the spectrum shown in Figure 57 will drop the peak transmission to 90% when grating length changes by +/-1.0 mm. A strong MBG will be more susceptible to shifts in the period and require higher precision in terms of determining the locations of the null points of the envelope.

$$\frac{dT_{max}}{dR_{2,1}} \approx \frac{1}{R_{1,2} - 1} \quad (38)$$

This tolerance can be applied to the spectrum measured in Figure 59 which exhibited a peak transmission of about 93%. Using Eq. 35, the reflectance values for each of the mirrors in this MBG is about 74%. A drop in transmission efficiency of 7% for this filter can be the result of a difference in mirror reflectance of just 2% using Eq. 38.

In recent experiments with MBGs, another source of decreased transmission peak was noted. An MBG with such a spectrum is illustrated in Figure 78. This MBG was designed with a 1064 nm

central wavelength, an envelope period of 5.5 mm and $2n_l$ of 380 ppm. The MBG demonstrates a bandwidth of 9 pm FWHM but only a 73% peak transmission.

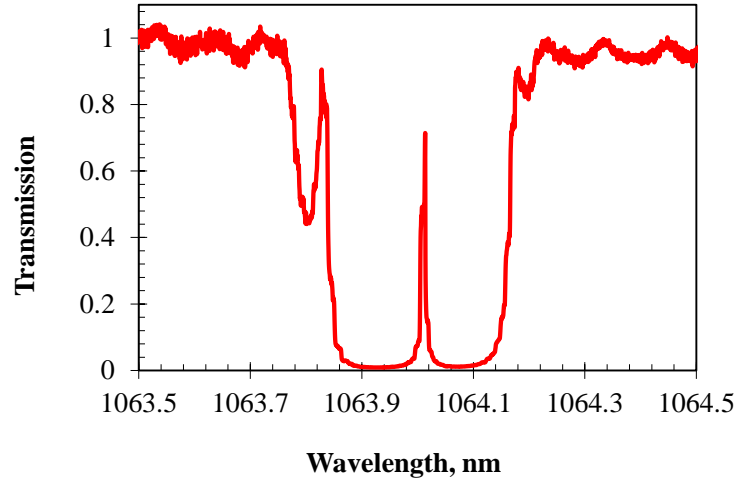


Figure 78: An MBG spectrum demonstrating the effect of a gradient of resonant wavelength approximately equal to the bandwidth of the transmission peak.

The decrease in transmission peak for the MBG is due primarily to a lack of homogeneity of the resonant wavelength of the grating structure across the aperture of the measuring beam. The effect of inhomogeneity, measured in pm/mm, can be modeled by averaging the effect of resonant wavelength shifts over the aperture using Eq. 39.

$$T(\lambda) = \frac{\int P(\lambda + d\lambda) d\lambda}{\int d\lambda} \quad (39)$$

Here $P(\lambda)$ is a spectrum describing the shape of the transmission window which, for a FPE can be sufficiently described using a Lorentzian distribution. The effect of this shift on the peak transmission of the filter as well as the effective spectral width has been calculated as a function of the total resonant wavelength shift ($\Delta\lambda_{res}$) over the aperture, normalized by the nominal FWHM ($\Delta\lambda_{in}$) of the designed MBG. In order to preserve the peak transmission of greater than 95%, the ratio of $\Delta\lambda_{res}/\Delta\lambda_{in}$ must be less than 0.4.

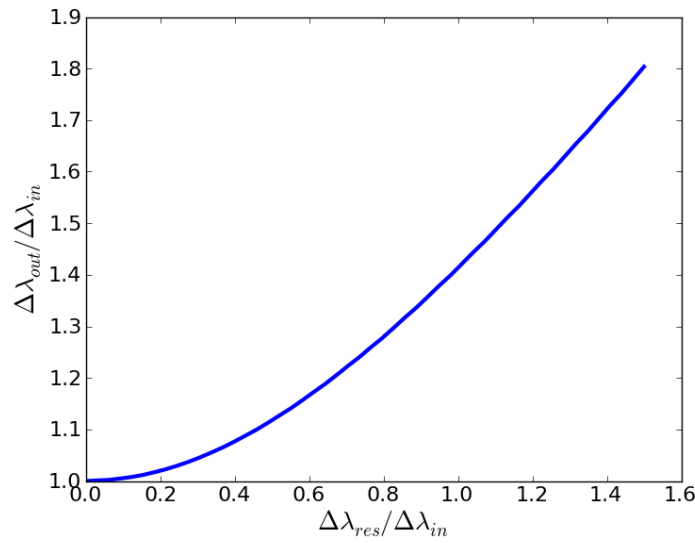


Figure 79: The relative increase in the spectral width of the filter ($\Delta\lambda_{out}$) due to a relative change in the resonant wavelength across the working aperture.

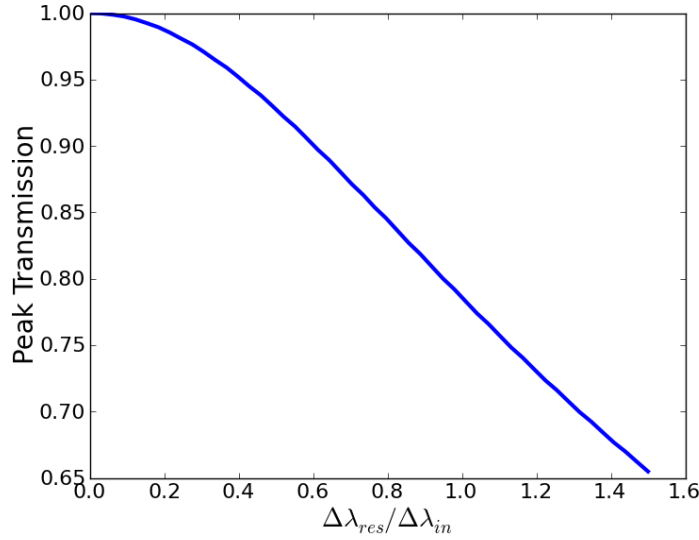


Figure 80: The drop in peak transmission due to a relative change in the resonant wavelength across the working aperture.

The MBG from Figure 78 was measured at several locations across the aperture of the grating and a gradient of resonant wavelength was measured to be 10 pm/mm. This gradient is on the same order as the final bandwidth ($\Delta\lambda_{res}/\Delta\lambda_{in} \approx 1$). According to Figure 79, a widening of the bandwidth by about 1.5 times can be expected and a peak transmission of 73% is a reasonable result according to Figure 80.

After identifying the primary sources of decreased transmission and quantifying their extent, it was necessary to create methods to mitigate these errors. As noted previously, a grating with a well centered phase shift with a thickness equal to the period of the envelope pattern will have equal effective mirror strengths. The improvement of the transverse measurement techniques for determining the axial profile of an MBG has greatly improved the peak transmissions that have

been obtained. Accurate determination of the zero points and the envelope period was the first critical improvement to MBGs. Additional improvements have been realized by reducing the gradient of resonant wavelength. The primary source of gradients in the resonant wavelength are due to shifting background refractive index through the depth of the recording. This can be caused by light absorption through the depth of the grating during recording. The highest photodosage is applied at the incident surface and absorption of the UV light by Ce^{3+} depletes the radiation as it passes to the back surface. This inequality of dosage through the depth causes the spatial average of refractive index change to be higher at the incident surface which relates to a slightly shifted background index and hence different resonant wavelengths. Several methods to remove this gradient have been suggested. One is to illuminate the back side of the grating after holographic exposure to a uniform beam in order to equalize the background dosage applied to the front and the back. Experiments trying to remove the gradient from single RBGs were unsuccessful in producing any meaningful change in the gradient and in fact, inconsistent measurements of the gradient level were obtained such that even the sign of the gradient changed from sample to sample. The solution that was pursued to reduce this effect of vertical gradient was to use PTR with lower absorption levels. This required longer recording times since the photosensitivity lowers as well. Therefore, the ability to phase stabilize the recording was a critical tool for these recordings.

Two different glass melts with a third and a quarter of the cerium content were used to demonstrate the benefits of lower absorption PTR for MBG recording. The melt with a third of the cerium gave a gradient of about 5 pm/mm and the melt with a quarter of the cerium gave no

discernable gradient in the background refractive index. The shift of the resonant wavelength of the transmission peak and the center of the reflection lobes with respect to the average resonant wavelength across the aperture is shown in Figure 81. The vertical position of zero is the back surface of the recording and 12.5 mm is the incident surface of recording. Both the location of the transmission peak and the center of the reflection band are located at the same location and do not show any monotonic decrease of the resonance wavelength from back to front as expected for the case of strong absorption.

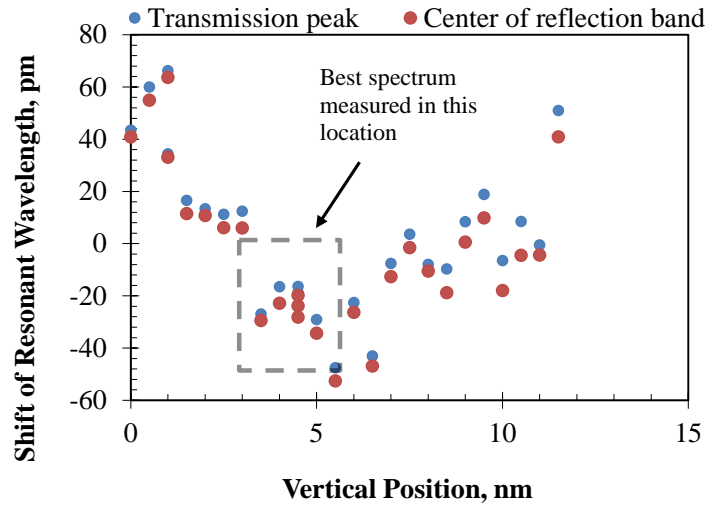


Figure 81: The vertical gradient in a MBG recorded in a low absorption PTR glass melt.

The transmission spectrum through the device was measured and the best performance was found at a location marked in Figure 81. The transmission spectrum is shown in Figure 82 along with a simulation of the performance predicted by CWT. The grating has a thickness of 4.4 mm with and envelope period of 4.4 mm, a resonant wavelength of 1063.93, and a maximum

refractive index modulation of 375 ppm. The measured data gives a transmission efficiency of 90% and the transmission bandwidth is $15 \text{ pm} \pm 1 \text{ pm}$. The rejection ratio between the transmission peak and the minimum transmission is -15 dB. The gradient at this location is minimal. Therefore, the primary detriments to the MBG transmission efficiency are most likely other types of inhomogeneity in the medium and the recording.

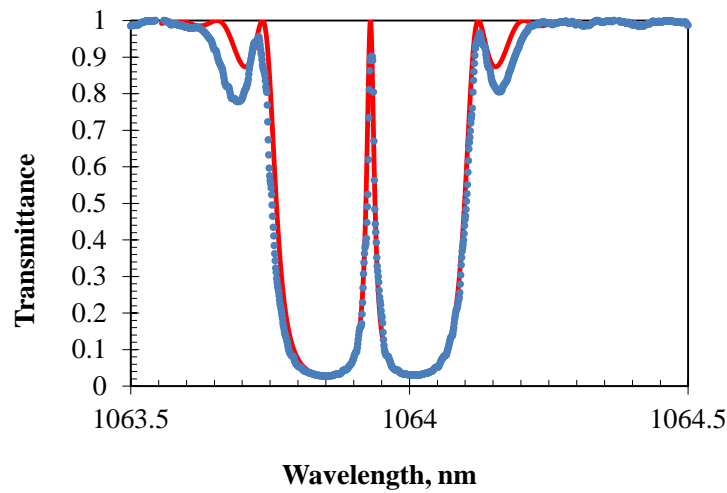


Figure 82: The transmission spectrum of a MBG recorded in low absorption glass with 15 pm transmission bandwidth and 90% transmission. Solid red is CWT simulation and blue dots are measured values.

Due to the very sharp resonance, this transmission peak is very sensitive to small inhomogeneities that do not cause severe detriment to uniform RBGs and TBGs. Inhomogeneity that shifts the resonance can be caused by local differences in refractive index. A difference of just 10 ppm in the refractive index can shift the resonant wavelength by 7 pm. The affect that this would have on the resonance would depend on the location and size of the inhomogeneity. This

level of inhomogeneity is certainly possible and can have significant impact on the peak transmission. Small levels of losses such as absorption and scattering can also have disproportionate effects on the transmission peak. This is because resonant transmitted light is essentially passing through a high Q resonator and will make multiple passes within the grating before exiting. Therefore, even small levels of losses can reduce the efficiency of the device more so than for a uniform RBG or TBG. These issues provide a material based limit to the efficiency that can be achieved in a MBG, but also provide an excellent way to directly monitor improvements made to PTR glass in that the MBG requires much higher quality than other typical types of VBGs. The current performance that has been achieved still exhibits very narrow resonance with high efficiency of 90%.

Application in a Laser System

An MBG filter with a transmission bandwidth of 15 pm is presented here for use in a laser cavity to select longitudinal modes. The device was recorded for a central wavelength of 1064 nm with a difference in resonant wavelength of 100 pm between the two individual gratings. This was achieved by using a shift in recording angle of 9.4 arcseconds between each recording while keeping the bisector angle constant. As previously mentioned, this type of recording results in a moiré pattern with the envelope in an undefined state and it is necessary to process the pattern to accurately determine the locations of the zeros in the envelope. This was accomplished by using a transverse diffraction efficiency scan. From identifying these locations, the grating was cut and

polished such that the final grating contained a single envelope zero located near the center of the grating.

The transmission spectrum of the grating was measured using a tunable laser diode with sub-picometer resolution. The testing setup is shown below in Figure 83. A fiber coupled tunable laser is sent through a 3 dB coupler. One arm probes the grating with a collimated beam, while a power detector measures the transmission through the grating. The unused arm of the coupler is used to monitor back reflection from the sample to ensure that the grating is characterized at normal incidence.

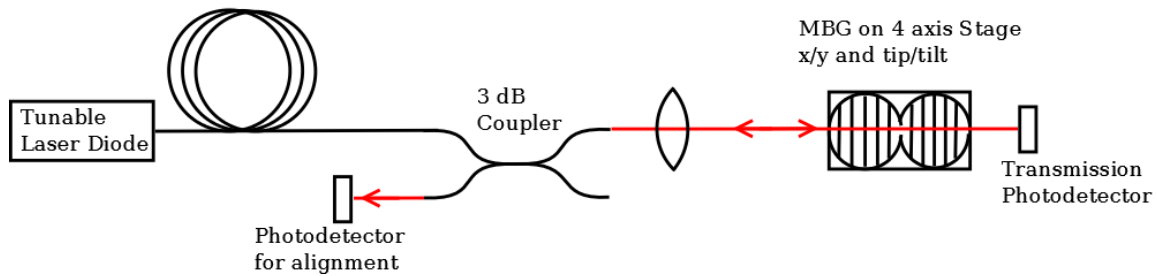


Figure 83: The setup for characterization of the spectral transmission of an MBG with a high resolution tunable laser. A 3 dB coupler is used to determine alignment by monitoring the intensity of back reflection from the gratings rejection band.

The resultant transmission spectrum of the MBG is shown in Figure 84. It shows experimental data as well as a theoretical fit using matrix CWT. The width of the transmission peak is 15 pm FWHM and rejection band is 254 pm FWHM. The filter has a peak transmission of 84% with 4.2% being transmitted in the reflection band giving a rejection ratio of -13 dB between the peak transmission and the minimum transmission. The spectrum shows a distinct asymmetry about the

resonant peak. It was found that this asymmetry is primarily due to a mismatch in the recording dosages. By inducing a mismatch in the strength of the RIM in the simulation, the level of error in the exposure can be established. The mismatch in RIM is 50 ppm from the specified value. Excellent coincidence between experimental results and the theory can be seen in the region of the pass band and rejection band of our filter. For the use of such a grating in a laser system it is also important to understand the angular selectivity of the MBG as this will be operating under an angle in the final system to avoid lasing off of the reflection bands. The angular spectrum was measured using the same system and the results are shown in Figure 85. The angular response is very wide and the peak transmission has a flat response over about 0.3° , meaning that the device can achieve optimal performance even when operating under small angles. In comparison with a typical FPE which has an angle selectivity of 17° for every nanometer of spectral bandwidth, this filter has $43^\circ/\text{nm}$, meaning that MBGs have at least twice the acceptance angle of a normal FPE.

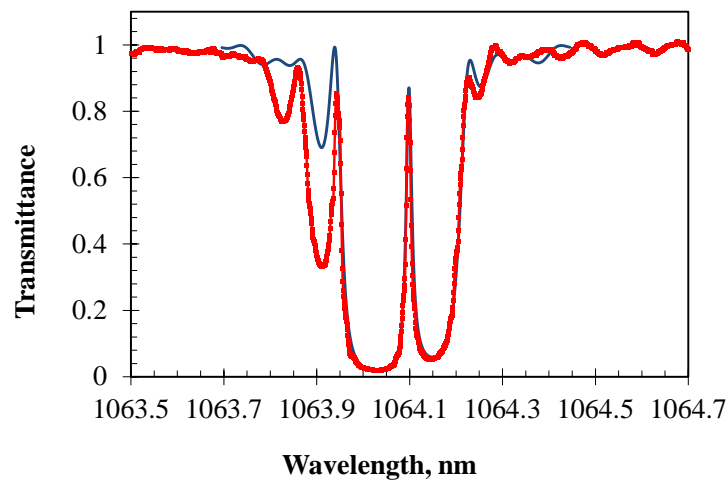


Figure 84: Transmission spectra of an MBG in PTR glass with length = 5.3 mm, refractive index modulation $n_1=126$ ppm, $n_2=234$ ppm. Blue – theory, red – experiment.

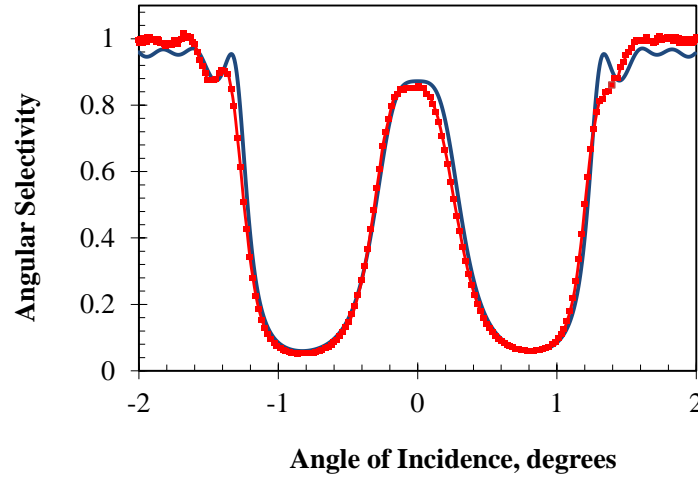


Figure 85: Angular selectivity of an MBG in PTR glass with length = 5.3 mm, refractive index modulation $n_1=126$ ppm, $n_2=234$ ppm. Blue – theory, red – experiment.

The narrow band transmission can be used as an intracavity filter for the generation of single frequency laser as depicted in Figure 86. The laser cavity consists of an ytterbium doped fiber as the gain medium. The output is coupled into the free space cavity where the MBG is placed to achieve longitudinal mode selection. A uniform RBG with 30% reflectance is used as an output coupler. The spectral width of the output coupler is selected to match the spectral width of the MBG such that only the modes within the resonance peak of the MBG are allowed to resonate in the cavity. The longitudinal mode structure of the laser is characterized using a scanning Fabry Perot interferometer. The cavity length of the laser is approximately 1.5 m resulting in a longitudinal mode spacing of 120 MHz (0.5 pm).

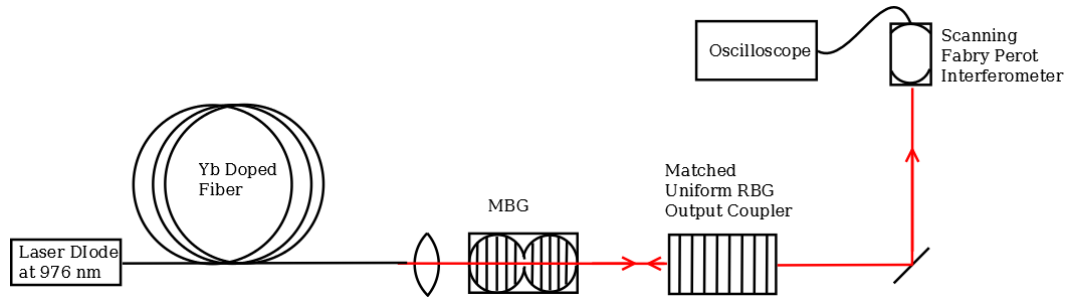


Figure 86: A fiber laser with free space section of cavity incorporating a MBG for mode selection. A scanning Fabry Perot interferometer is used to determine the longitudinal modes present in the laser.

Alignment of the MBG is achieved by first aligning the reflection in the rejection band such that the laser is locked to the rejection band. The MBG is then tilted so that lasing is not achieved from reflections from the MBG. Note that the angular selectivity of the grating in Figure 85 is 0.64° FWHM and over 0.3° there is a drop of only 5% in the transmission. In comparison, a tilt of tens of arc seconds is sufficient to destroy lasing off of the reflection from the rejection bands. This tilt causes no appreciable change in the filter characteristics and it is therefore acceptable to align the grating off normal incidence.

The spectral output of the laser with an intracavity MBG was measured using a scanning Fabry-Perot interferometer with a resolution of 7.5 MHz and a free spectral range of 1.5 GHz. Figure 87 shows the spectrum that was generated without the MBC in the cavity and Figure 88 show the spectral output with the MBG aligned in the cavity. Without the filter in place, the modes fill the FSR of the etalon. The 15 pm bandwidth of the filter effectively acts as a filter with bandwidth around 2 pm due to only a very narrow region in the transmission peak of Figure 84 being above lasing threshold. The filter thus allows selection of three modes from the spectrum.

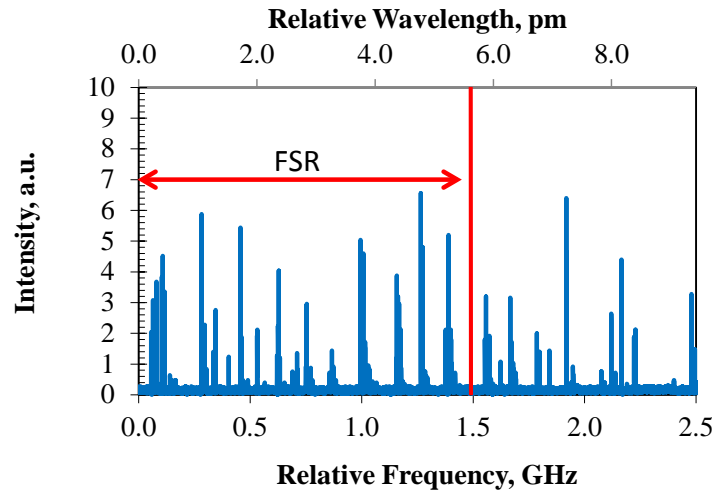


Figure 87: The spectrum of the output of the fiber laser system operating without an MBG in the cavity as measured by scanning Fabry Perot etalon.

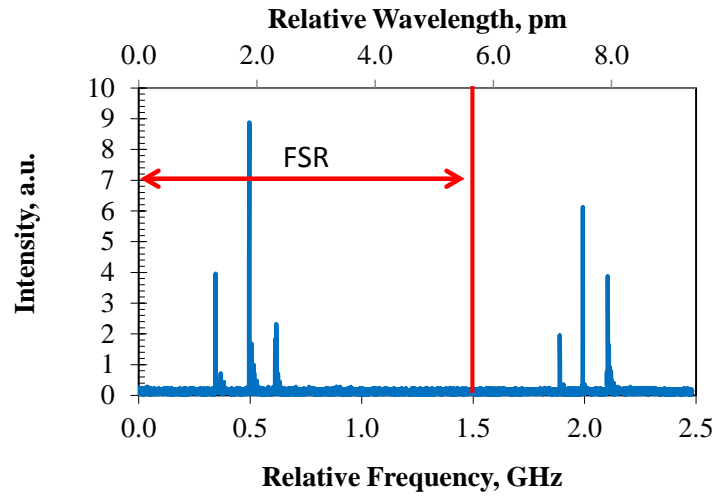


Figure 88: The spectrum of the output of the fiber laser system operating with an MBG in the cavity as measured by scanning Fabry Perot etalon, demonstrating a reduction of the longitudinal modes to a total of three.

A moiré volume Bragg grating with spectral FWHM of 15 pm is demonstrated with good conformity to theory. The application of the MBG into a laser cavity shows the potential for generating high power single frequency output. Given the current laser configuration, the number of resonating longitudinal modes is reduced to three. The primary benefit of this mode selection device is the simple alignment procedure for free space laser cavity systems. Further work will focus on fabrication of MBG grating devices with higher transmission throughput and narrower bandwidths for laser systems that require single mode operation.

This work in developing MBGs shows the strength of interdependent multiplexing in that very unique spectral filtering can be achieved by the interplay of two sequentially recorded VBGs. A simplified theory of operation is presented that shows good agreement with measured results. The issue of determining the location of phase shifts in an MBG recorded in bulk glass is addressed using a number of transverse measurement techniques. The axial profile measurement methods show good accuracy and also reveal a number of material differences between regions containing strong refractive index modulation and regions with roughly uniform refractive index change. These differences will serve as a source of future work in understand the mechanisms of refractive index change in PTR glass. A number of MBGs have been characterized using these method and show various levels of bandwidth and peak transmission. The sources of non-optimal peak transmission have been investigated theoretically and tested against measured results. By understanding these sources, the best MBG performance to be achieved had a bandwidth of 15 pm and peak transmission of 90%. Finally, the use of an MBG in a laser cavity showed the application of this spectral filter for selecting longitudinal modes. This section adds

to the state of the art in phase shifted gratings by addressing unique technical challenges that exist in creating high efficiency moiré Bragg gratings in bulk glass.

6 MANY CHANNEL MULTIPLEXED VBGs

The final type of multiplexed grating to be discussed is referred to as a many channel multiplexed VBG. These gratings have ‘many’ channels in that multiple gratings are used to create not just one, but multiple diffraction orders over a broad wavelength spectrum, angular spectrum, or both. This behavior is distinct from a single thin grating that produces multiple diffraction orders in that a different Bragg condition is fulfilled for each one of the many orders. Fabrication of a many channel device of this type is achieved by recording several gratings into the same volume of PTR glass, each with similar properties that are shifted incrementally with respect to the other adjacent gratings. Because of the proximity of the spectra of each individual grating the net operation of these many channel multiplexed gratings can appear to be not unlike a single grating. Such a device can be used to increase the number of combining channels in a multiplexed grating for use in SBC or CBC applications. This type of grating is an intermediate step between interdependent multiplexed gratings and a more complex structure like an image hologram.

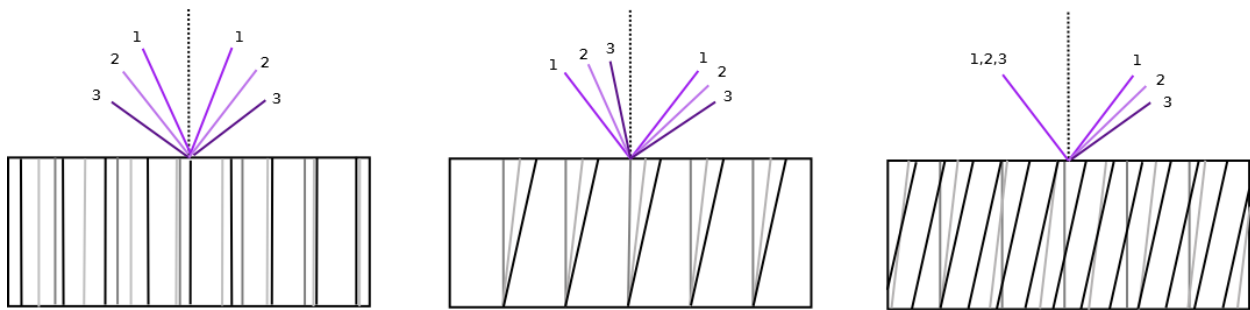


Figure 89: Examples of many channel multiplexed gratings. From left to right: broadband mirror, broad angle mirror, and many channel splitter.

Examples of many channel reflection gratings are shown in Figure 89. For purposes of illustration, the geometry for each type of broadly multiplexed grating is shown using only three recordings, however in practice these types of gratings would include several times this number of recordings. In these examples broad wavelength response is achieved by recording multiple grating periods which are controlled by the interference angle of the two recording beams. Broad angle acceptance is achieved by recording the same period multiple times with a different tilt angle each time, which is achieved by tilting the sample for each subsequent recording. Broadband splitting, as shown in the third example, is achieved by modifying both the period and tilt angle for each recording. The unique features of these proposed devices are presented in this section.

Broadband Mirrors and Multi-notch Filters

The technique of recording multiple reflection gratings using the same tilt angle but different grating periods can be used to create devices with broad wavelength selectivity and multi-notch filters. Notch filters are useful for applications such as astronomy or spectroscopy where unwanted atmospheric noise signals needs to be removed. For such applications, several notch filters can be multiplexed into a signal device which will transmit all desired wavelengths of light while excluding the select noise signatures. Alternatively, if the notches are designed in close spectral proximity to each other, a broad spectral reflection grating can be created, though this finds limited application as broadband reflectivity can be more easily achieved using thin

recording media. The multi-notch Bragg grating is investigated as an example of a many channel VBG which employs multiple collinear gratings of varying spatial periods.

A broad spectrum multiplexed reflection grating was recorded with spectral responses that were separated by 0.5 nm. This allows the performance of each grating to be observed and assessed individually. One such device was recorded with a total of 18 exposures such that each notch has a resonant wavelength which is separated by 0.5 nm, in the vicinity of 1064 nm. The transmission spectrum of the device in Figure 90 was measured using a tunable wavelength laser source and a photo-detector to measure transmitted light. The grating has a thickness of 20 mm and produces 18 notches, each with a rejection greater than 10 dB with respect to the out-of-band transmitted light and a bandwidth of around 50 pm. It should be noted that even though the grating at 1067.5 nm was recorded with too low of a dosage, it still produced a rejection efficiency of 90%. This demonstration is the greatest number of high efficiency individual RBGs multiplexed within the same volume of PTR shown to date.

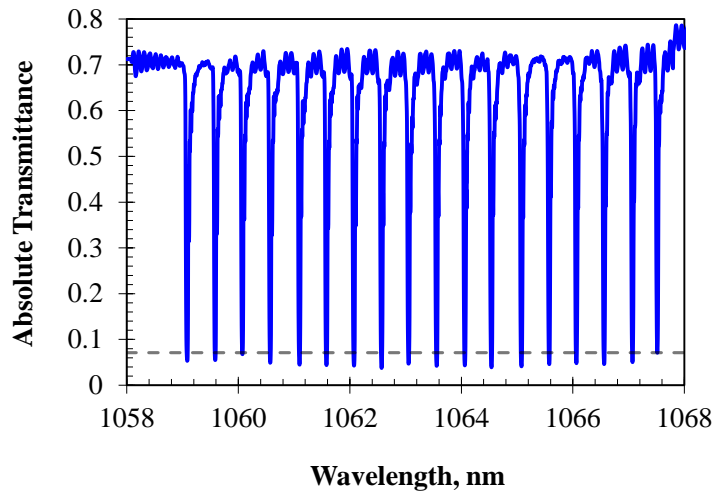


Figure 90: The transmittance spectrum of a broadband mirror distinct, separated spectral responses for each grating. Results demonstrate the recording of 18 gratings in one piece of PTR with a rejection efficiency greater than 90%.

One interesting property of this many channel VBG that can be explored in future work, is the use of the broadband mirror structure to create apodization profiles. This type of multiplexed grating is essentially a moiré Bragg grating with many more recordings. Addition of sinusoids allows any type of apodization structure to be created. For example, recording a sampling of grating periods within a discrete range and of equal strength will generate a *sinc* apodization profile which appears periodically throughout the thickness of the device. Practically speaking this sort of behavior is very difficult to control since the actual locations of these structures can only be controlled if the phase of each grating relative to each other can be controlled. For multiplexed gratings with relatively tightly grouped grating periods, the pattern may not appear at all within the thickness of a typical 25 mm sample. For other designs where the multiplexed gratings have relatively widely grouped grating periods, the recording plane will have to be

changed between recordings and any sort of relative phase control will be lost. The difficulties in either case are not insurmountable technical challenges but would require significant effort to achieve. Between these two extremes there may exist particular designs that are well suited for this recording setup that warrant further investigation in future work. Such work would combine results demonstrated by the 18 channel multi-notch filter described in this section, and the techniques demonstrated in the section regarding moiré Bragg gratings, in order to create this new type of multiplexed grating design.

Broad Angle Mirror

The broad angle mirror shown in Figure 89 is a mirror with broad angular response that contains many gratings with the same period but different grating tilt directions. Such a device acts as a mirror with narrow spectral bandwidth, but an increased angular acceptance compared to a similar RBG of the same thickness. While the broad angle acceptance of this device does not distinguish it significantly from a thinner RBG or mirror, there is at least one potentially unique design of interest for the broad angle mirror which is essentially a discrete implementation of a concave mirror. Such a mirror could be used in a laser to obtain cavity configurations that are more robust to alignment errors or to facilitate transverse mode control.

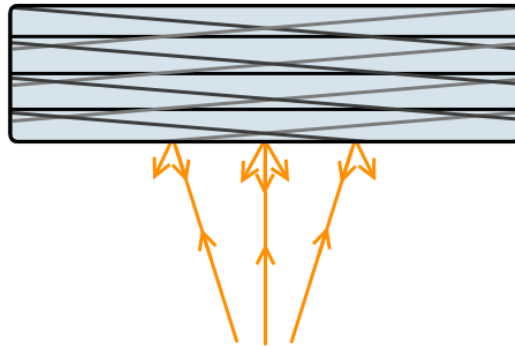


Figure 91: The use of a broad angle mirror to increase the number of back reflections for a divergent beam.

The basic operation of the aforementioned broad angle mirror design as it back-reflects a divergent incident laser beam is shown in Figure 91. Three discrete gratings of the same period are angle multiplexed within the same volume with the central non-tilted grating serving to exactly back reflect normally incident light. Each of the angled gratings are symmetrically tilted at a small angle with respect to the non-tilted grating and are designed such that they exactly back reflect the most highly divergent rays contained in the beam.

The important feature to note here is that the divergent beams will be exactly back reflected despite their non-normal angle of incidence. This behavior differs from a standard RBG which reflects any incident ray within its angular acceptance range in the same fashion as a planar mirror. In this sense, the broad angle mirror behaves in a fashion similar to that of a concave mirror. However, the device differs from a concave mirror in a number of ways. First, it is spectrally selective, and though spectrally selective coatings are often applied to laser mirrors, the narrow spectral selectivity of this device is inherent. Second, there are a discrete number of

gratings so the rays in between the rays depicted in Figure 91 will not be paired with any grating and will not be exactly back reflected. This can of course be addressed by multiplexing a larger number of gratings to fill in these gaps. The end goal for such a device is a discretized concave mirror consisting of many tilted RBGs. Third, if the tilts of the multiplexed gratings are smaller than the angular acceptance of any individual grating, then the incident light will be resonant with several gratings simultaneously. This third case is included in Figure 91, where each incident ray is resonant with several gratings at the same time, and as a result multiple reflections are generated. Therefore, a normally incident ray is reflected and diverges according to the various tilts of each of the three gratings. The divergent rays may only be resonant with two gratings as shown in this case, but still diverge upon reflection.

Finally, every grating is contained throughout the volume of the device. This is a potentially important distinction compared to a concave mirror because the position of incidence will not change the characteristics of the reflection. For a concave mirror or other focusing elements, translation within the aperture will induce a tilt of the reflected light. In contrast, the broad angle mirror is insensitive to translation of the incident beam within the aperture.

In order to explore the unique characteristics of such a device, a broad angle mirror was fabricated with a design based off of a non-tilted RBG at 1064 nm with a thickness of 10 mm and a refractive index modulation of 100 ppm. At normal incidence the FWHM bandwidth of this grating is 90 pm and the FWHM angle of acceptance is about 0.7° in air. Based on these parameters, a five channel multiplexed grating was designed such that the angular spectrum of

each grating would overlap. The tilt angles of the gratings were selected such that light would be back reflected for the following angles of incidence in air: 0° , $\pm 0.18^\circ$, and $\pm 0.36^\circ$. The grating was developed such that a maximum RIM of 500 ppm was achieved so that each grating reached the desired RIM of 100 ppm.

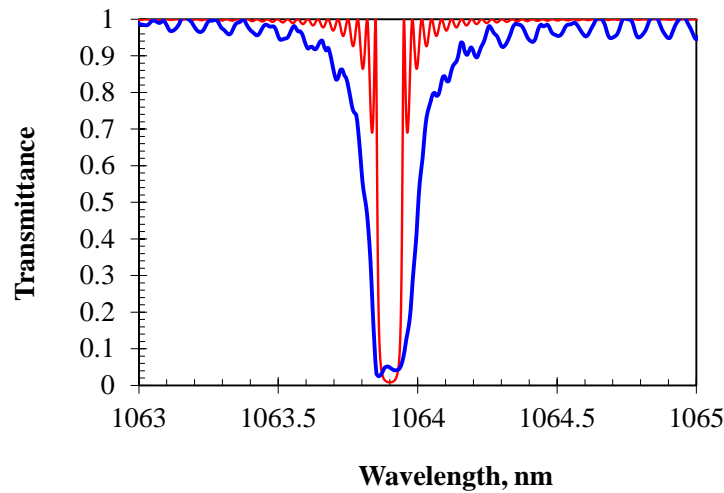


Figure 92: The transmission spectrum of a five channel broad angle mirror. Blue shows the measured transmission through the device. Red shows the transmission spectrum of a single RBG with a thickness of 10.45 mm and RIM of 100 ppm.

After recording and development the grating was cut to a thickness of 10.45 mm. Collimated light from a tunable laser source was sent to the device at normal incidence with a beam diameter of approximately 3 mm. The transmission through the device was measured using a photo-detector. The incident wavelength was swept and the transmission monitored to generate the spectral response of the device shown in Figure 92. The measured transmission is compared to the spectral response of a single RBG with the same refractive index modulation and thickness.

The spectrum of the broad angle mirror is slightly broadened by comparison, but is still roughly similar to that of a single RBG. The broadening can be expected due to the tilted gratings which will allow resonance at lower wavelengths. The difference in spectral width can also be due to inducing a RIM larger than 100 ppm. Only by developing a full coupled wave theory for broad angle mirrors, which would take into account the interaction of adjacent gratings, will a truly accurate comparison be possible. For this initial demonstration, it is clear that the spectral bandwidth remains relatively narrow at 195 pm and efficiency is high at 95%. What is not evident from the spectral transmission is the angle at which the light is reflected. When light of the resonant wavelength of 1063.9 nm is incident on the device, the light is reflected back towards the source and diverges in the plane of the grating tilts. Future work will address the actual divergence of the reflected light and look into how a divergent (either small diameter or defocused) beam will interact and reflect off of the grating. However, the current analysis serves to confirm the assumption that, at first order, the device operates according to Figure 91 and the associated discussion.

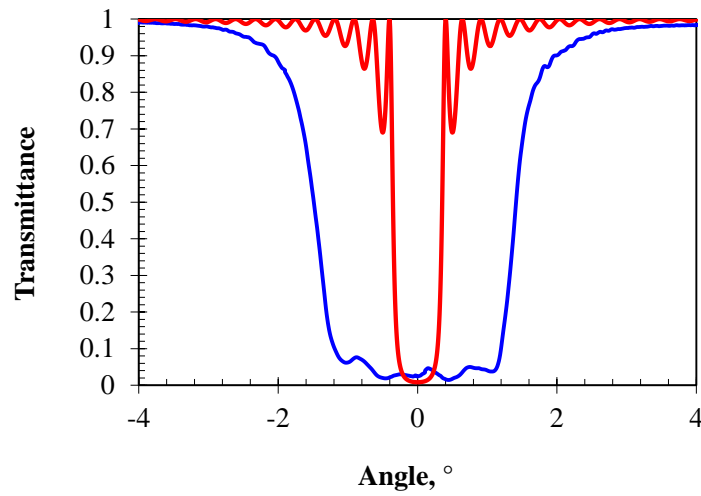


Figure 93: The angular acceptance of the five channel broad angle mirror for light at 1063.90 nm. Blue shows measured data. Red shows the angular acceptance of a 10.45 mm grating with RIM of 100 ppm.

The characteristic of most interest with the broad angle mirror is not the spectral response, but rather the angular selectivity of the device. With a fixed wavelength of 1063.90, the transmitted light was measured as the angle of incidence on the device was changed. The transmitted angular response of the device is shown in Figure 93 along with the theoretical angular acceptance of a single RBG with the same thickness of 10.45 mm and similar RIM of 100 ppm. This figure demonstrates that the angular response of the grating is significantly broadened, while the spectrum remains narrow as previously shown in Figure 92.

Further confirmation of the narrow spectral response can be made by observing the angular selectivity at four different wavelengths shown in Figure 94. At higher wavelengths, the gratings become out of resonance and the overall efficiency starts to decrease. At lower wavelengths, the

reflections begin to occur far from normal incidence. A change of wavelength of 50 pm shows some degradation of the angle response, and significant degradation is seen 100 pm away from the nominal resonance. This demonstrates that such a mirror in a resonant cavity would only provide significant feedback within a spectral band of ± 50 pm.

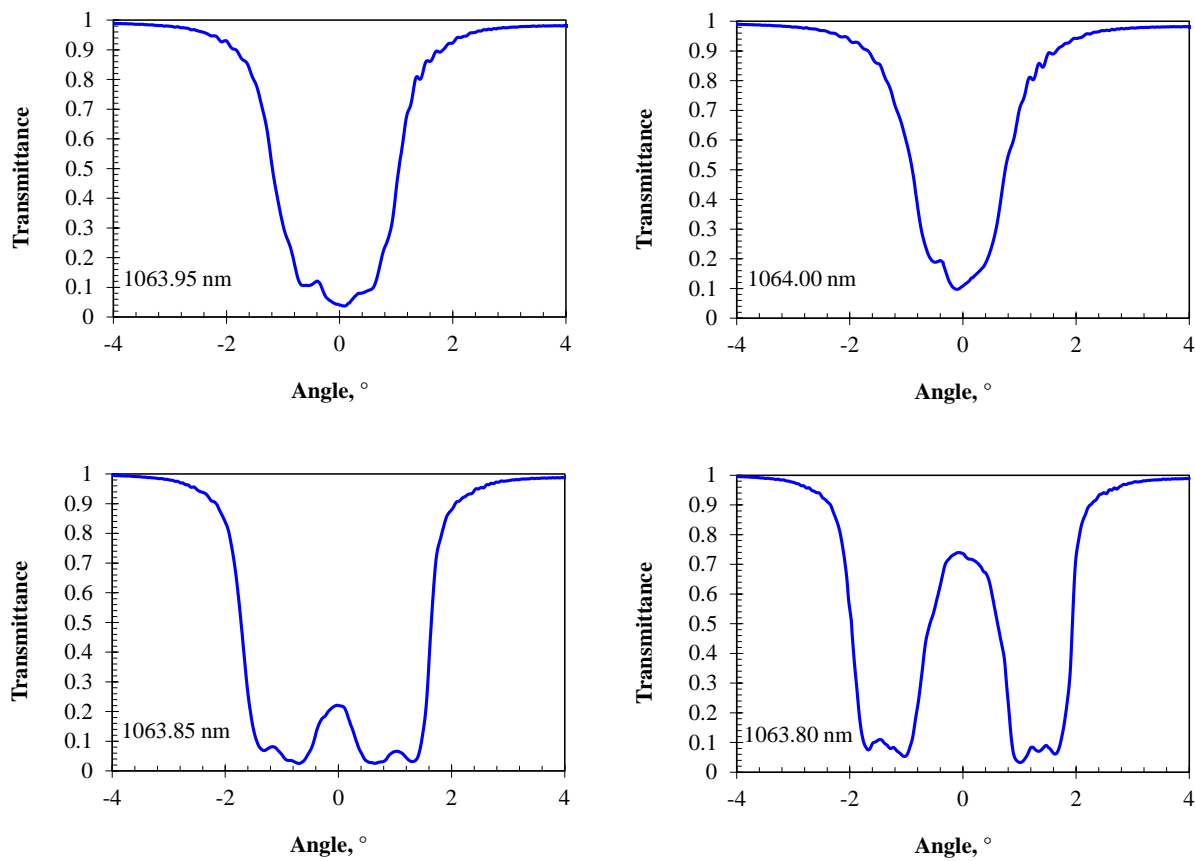


Figure 94: The angular acceptance of the five channel broad angle mirror at different angles of incidence. The top row shows the response to wavelengths higher than nominal resonance and the lower row shows the response for wavelengths lower than the nominal wavelength of 1063.90 nm.

The broad angle mirror demonstrated here is a proof of concept. It is intended to serve as a discrete implementation of a concave mirror, with several important differences outlined above within this section. The initial broad angle device appears to function as expected. Namely it is able to produce narrow wavelength band reflection within a broad angle of acceptance and light is reflected at multiple angles. The overall efficiency of the device is above 95%. This initial demonstration serves to encourage future development of this unique new multiplexed grating device.

Many Channel Splitter

The most generalized form of the three many-channel multiplexed grating designs combines many gratings with variation in both tilt and period. By tailoring the tilt and period of the multiplexed gratings, the angular dispersion of the grating can be precisely and arbitrarily customized to any desired dispersion profile. Such devices can be designed for coherent beam combining, spectral beam combining (wavelength division multiplexing), coherent splitting, or spectral splitting (wavelength division demultiplexing) depending on the desired application. Examples of these functionalities are illustrated in the various subfigures of Figure 95. Figure 95a depicts such a device being used to split a single wavelength into multiple channels with Figure 95b showing the same system reversed for coherent combining. Figure 95c is, again, the same device being used at a different angle of incidence to disperse broadband light into an array of angle channels.

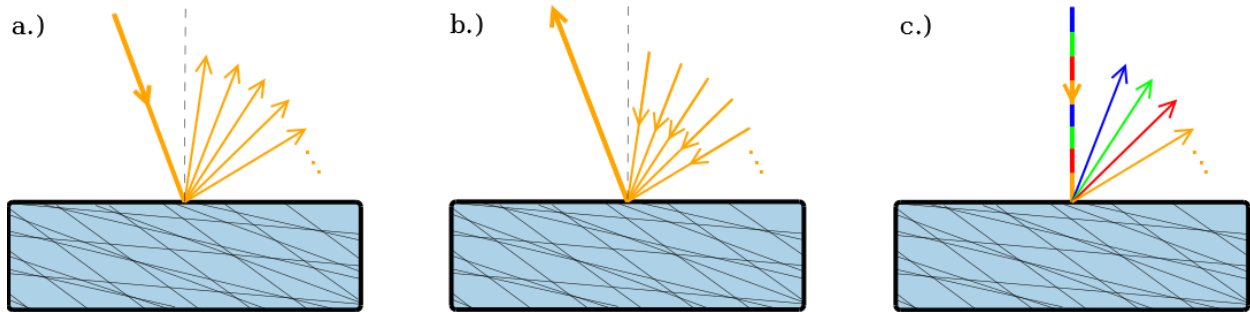


Figure 95: The many channel splitter can be used in several ways. a.) shows the use as a coherent 1:N splitter, b.) shows the system reversed to give a coherent N:1 combiner, and c.) shows a wavelength demultiplexer which is achieved by using a different angle of incidence

The particular design shown in Figure 95 is capable of achieving all of these configurations using the same device, as will be discussed in more detail later in this section. This configurability makes it useful for demonstrating the various properties of many channel splitters. But in general, the design of the angular dispersion can be arbitrary and therefore custom tailored to a specific experiment. The arbitrary dispersion profile is due to the device containing many discrete gratings, each of which is used to generate a different splitting channel. This feature makes such devices very flexible and highly desirable for a range of applications.

To demonstrate a proof of concept of this versatile multiplexed grating, the design of Figure 95 was implemented with 20 channels. The design uses an angle of incidence of 10° (in air) with respect to the surface normal for the common degenerate arm. The angles of the individually split arms range from -2° to -12.25° in steps of 0.75° when used in the configuration of Figure 95a. The dosage for each of the twenty exposures was 0.035 J/cm^2 . The target resonant

wavelength was in the vicinity of 1064 nm. Finally, to prepare the device for characterization, it was cut to a thickness of 10.4 mm after photo-exposure and thermal development.

The device was tested by probing at 10° angle of incidence using a tunable laser source to measure the transmitted irradiance as the wavelength of the laser was swept, which generated the spectral response of the device shown in Figure 96. When the tunable laser source is set to the resonant wavelength of the many channel splitter, light reflected from the device can be observed on a screen and 20 spots, separated by 0.75° , are visible. At this particular angle of incidence (10°), all gratings are being addressed simultaneously and the device effectively acts as a 20 way splitter with 90% of the light going into the split arms. By reversing the alignment of this configuration as was shown in the previous section on 4x RBGs for CBC, coherent combining of 20 channels can be achieved with up to 90% combining efficiency.

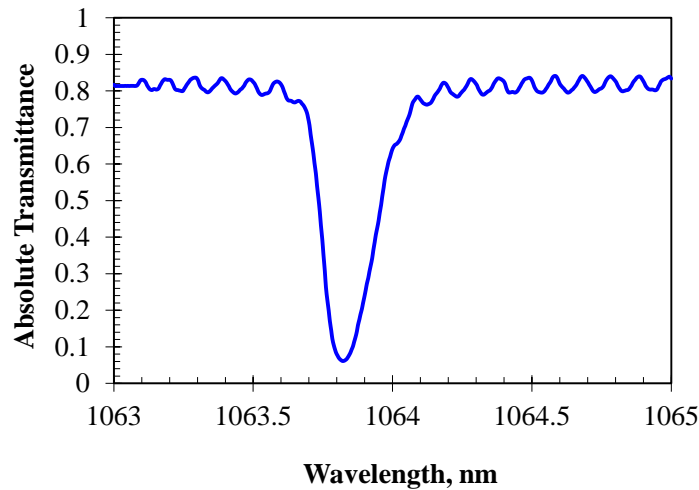


Figure 96: The transmission spectrum of the coherent splitter, as measured with a tunable laser. Reflected light is split into 20 channels separated by 0.75° .

Examination of the device at other angles of incidence gives further insight into its capabilities. This is demonstrated in Figure 97, where spectral transmission scans were taken at a variety of angles of incidence. It can be seen that the overall transmission bandwidth finds a minimum value at an angle of incidence of 10° . This is because all of the grating spectra start to converge to a single resonant wavelength. This location corresponds to the alignment for coherent splitting or combining that was just demonstrated in Figure 96. At angles far from this location, the individual gratings become resonant at different wavelengths and the transmission spectrum broadens. When the individual resonant wavelengths are split wide enough, the device can be used for spectral beam combining or wavelength division de/multiplexing.

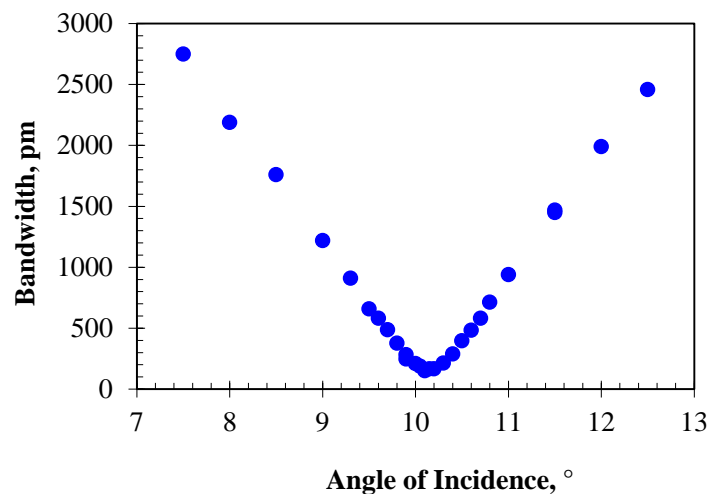


Figure 97: The reflection bandwidth of the 20 channel multiplexed VBG depends on the angle of incidence of light on the grating structure. Incidence at 10° gives a coherent beam splitter/combiner. At angles far from normal, the device acts as a wavelength division de/multiplexer.

Unique performance is achieved at an angle of 7° . At this alignment, the spectra are fully decoupled and act as individual gratings. The spectral transmission at this angle of incidence is shown in Figure 98 with reflections occurring over a 3.2 nm range. It is important to note that the device was not designed to produce 100% diffraction efficiency for the individual gratings. Rather they are intended to operate coherently. So this particular device produces only approximately 30% efficiency as a demultiplexer at this alignment since each of the gratings are operating independently. The efficiency of 30% corresponds to the individual efficiency of the gratings. At this angle, the device can be used as a splitter/demultiplexing with 30% being demultiplexed and 70% being transmitted. A similar device could be manufactured such that it is optimized for high efficiency in this wavelength demultiplexing configuration. The ability to record the large number of high efficiency, independently multiplexed gratings for this configuration was previously demonstrated in Figure 90.

As the wavelength of the incident light is tuned over the device's 3.2 nm reflection band, the reflected light is deviated in steps of 0.75° as the light becomes resonant with each subsequent grating, giving an angular dispersion is $4.4^\circ/\text{nm}$. Therefore, at this particular alignment, the angle of reflection can be selected by changing the incident wavelength. At angles of incidence within $\pm 1^\circ$ of 10° , multiple adjacent reflected spots can be addressed by a single wavelength until the alignment reaches 10° , the point at which all of the reflected spots are illuminated with a single wavelength. This means that 1:N switching can occur, with N being controlled by the angle of incidence, and the output angle can be switched by tuning of the incident wavelength. This tunable angle switching function is another interesting potential use of this device.

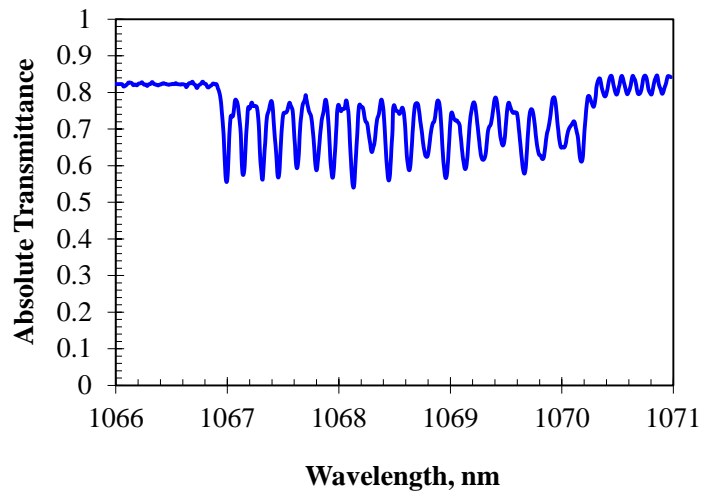


Figure 98: At an angle of incidence of 7° , the individual gratings start to decouple and the spectra start to shift away from each other. At this alignment, the gratings acting independently with an efficiency of about 30%.

This many channel splitter is an example of the most general type of many channel multiplexed grating and provides a number of useful and unique configurations. Given a well aligned CBC setup with active phase control, this device can achieve $>90\%$ combining efficiency. Operating as a demultiplexer the device can give 30% splitting into 20 reflected channels. At alignments between the SBC and CBC configurations, the device can act as a tunable 1:N angle switcher. The many channel broadband splitter design presented here provides an excellent starting point for a number of different highly multiplexed volume Bragg grating devices for future work.

The examples of many channel multiplexed devices, such as the multi-notch filter, the broad angle mirror, and the many channel splitter that have been presented in this section show concepts for new devices in PTR. Demonstrating these new types of devices confirms the

scalability of previous experiments in multiplexing and provides the ability to develop new types of beam control devices. Precision control over recording parameters has made it possible to mutually align many gratings within the same volume such that these results could be achieved. Working towards further developing these initial demonstrations of many channel multiplexed VBGs will provide new opportunities for the use of PTR glass in laser systems.

7 CONCLUDING REMARKS

This dissertation investigates the physics, recording, and applications of multiplexed volume holograms written in PTR glass. This study has enabled improvements of holographic recording methods, design of novel single VBGs, the design and recording of several types of multiplexed VBGs, and the applications of these technologies to laser systems. These improvements have enabled the recording of multiplexed gratings with precise spectral and angular filtering characteristics and high efficiency.

Topics in design and recording of multiplexed volume Bragg gratings, developments in holographic recording procedures, and applications of multiplexed volume Bragg gratings have all been covered in this document. In particular I have demonstrated a novel method for phase stabilization of holographic recording that operates independently of the recording media. The system possesses sensitivity to lateral shifts at the recording plane and utilizes a measurement beam that makes a double pass through the system to achieve high sensitivity to phase noise. The implementation of phase stabilization in the recording setup led to improved performance by increasing the refractive index modulation by 1.5 times in a reflecting Bragg grating compared to an unstabilized recording. Further, work related to single volume Bragg gratings has led to a new type of design parameter for transmitting gratings which find applications in transverse laser mode selection. This new design parameter is achieved by overmodulating a transmitting grating to achieve high diffraction efficiency while tailoring the shape of the angular response of the VBG device. Several types of multiplexed gratings have also been demonstrated and applied to

laser systems for beam control. Multiplexed gratings have been used to show the scaling of combined power in a spectral beam combining system. Greater than 95% combining efficiency was achieved with combined power of 420 W and no significant beam degradation. Scaling this system to four reflected combining channels showed no decrease in grating efficiency or reflected beam quality and opens a path to future work in scaling the system to higher powers with more combining channels. Next, a four channel coherent beam combining device was demonstrated to give 90% combining efficiency with no decrease in beam quality. This device required good mutual alignment and strength of each recorded grating. Improvements in recording procedure has allowed the design of this grating to be improved significantly. A unique type of interdependent multiplexed grating called the moiré Bragg grating has also been studied. The device behaves as a Fabry-Perot etalon and can easily achieve narrowband filtering on the order of tens of picometers within a thickness of 10 mm. Such a device has been implemented in a laser system for selection of longitudinal modes. In addition, a simplified theory of operation based on Fabry-Perot cavities has been used for determining tolerances for processing of MBG devices. Several methods for determining the axial profile of an MBG have been developed and used in order to process MBGs after recording. These methods reveal important differences between regions exposed by a sinusoidal pattern and regions that experience a roughly uniform exposure. A MBG with a spectral bandwidth of 15 pm and 90% transmission efficiency was demonstrated. Finally, a demonstration of extending the number of multiplexed gratings within the volume of PTR glass was shown. High efficiency multiplexed reflection Bragg gratings with 18 independent gratings each operating at >90% were shown, and several possible designs for useful many channel multiplexed gratings discussed. The path

forward leads toward multiplexing many more gratings within a single PTR glass sample in order to increase the functionality of these devices. The implications of this work will provide opportunities for creating more complex holographic structures through the interplay of the various recordings.

The research presented here paves the way for future work in making novel devices and demonstrates useful applications of multiplexed VBG technology. By contributing this knowledge to the body of science, I have provided a method for creating high-efficiency, robust, multiplexed volume Bragg gratings. To further this work, my results can be applied to novel devices that will extend the range of applications for multiplexed volume Bragg gratings recorded in PTR glass.

LIST OF REFERENCES

- [1] E. G. Loewen and E. Popov, *Diffraction gratings and applications*. CRC Press, p. 61, 1997.
- [2] “Optical Spectrum Analysis: Application Note 1550-4,” *Agil. Technol.*, p. 3, 2000.
- [3] J. C. Urbach and R. W. Meier, “Properties and limitations of hologram recording materials,” *Appl. Opt.*, vol. 8, no. 11, pp. 2269–81, 1969.
- [4] J. R. Lakowicz, *Principles of fluorescence spectroscopy*, Springer, 3rd ed., p. 38, 2006.
- [5] C. C. Katsidis and D. I. Siapkas, “General transfer-matrix method for optical multilayer systems with coherent , partially coherent , and incoherent interference,” *Appl. Opt.*, vol. 41, no. 19, pp. 3978-87, 2002.
- [6] J. Bland-Hawthorn, W. van Breugel, P. R. Gillingham, I. K. Baldry, and D. H. Jones, “A Tunable Lyot Filter at Prime Focus: A Method for Tracing SuperCluster Scales at $Z \sim 1$,” *Astrophys. J.*, vol. 563, no. 611, pp. 1–21, 2001.
- [7] C. Fricke-Begemann, M. Alpers, and J. Höffner, “Daylight rejection with a new receiver for potassium resonance temperature lidars,” *Opt. Lett.*, vol. 27, no. 21, p. 1932, 2002.
- [8] R. M. Hill, “Some Fringe-broadening Defects in a Fabry-Perot Etalon,” *J. Mod. Opt.*, vol. 10, no. 2, pp. 141–152, 1963.
- [9] A. L. Fehrembach, A. Talneau, O. Boyko, F. Lemarchand, and A. Sentenac, “Experimental demonstration of a narrowband, angular tolerant, polarization independent, doubly periodic resonant grating filter,” *Opt. Lett.*, vol. 32, no. 15, pp. 2269–71, 2007.
- [10] G. Hernandez, “Fabry-Perot with an absorbing etalon cavity,” *Appl. Opt.*, vol. 24, no. 18, p. 3062, 1985.
- [11] M. Bartek, I. Novotny, and R. Ydurahn, “Quality Factor of Thin-Film Fabry-Perot Resonators: Dependence on Interface Roughness,” *EuroSensors XIII*, p. 13P3, 1999.
- [12] W. H. Bragg and W. L. Bragg, *X Rays and Crystal Structure*. London: G Bell and Sons, Ltd., 1915.

- [13] R. R. . Syms, *Practical Volume Holography*. Oxford, UK: Clarendon Press, pp. 48, 64, 132–162, 1990.
- [14] H. Kogelnik, “Coupled Wave Theory for Thick Hologram Grating,” *Bell Syst. Tech. J.*, vol. 48, no. 9, pp. 2909–2945, 1969.
- [15] P. Taylor, “Modal Theory for Thick Holographic Gratings with Sharp Boundaries,” *J. Mod. Opt.*, vol. 27, no. 2, pp. 171–182, 1980.
- [16] M. G. Moharam and T. K. Gaylord, “Rigorous coupled-wave analysis of planar grating diffraction,” *J. Opt. Soc. Am.*, vol. 71, no. 7, pp. 811–818, 1981.
- [17] M. G. Moharam and T. K. Gaylord, “Chain-matrix analysis of arbitrary-thickness dielectric reflection gratings,” *J. Opt. Soc. Am.*, vol. 72, no. 2, p. 187, 1982.
- [18] I. V. Ciapurin, L. B. Glebov, and V. I. Smirnov, “Modeling of phase volume diffractive gratings, part 1: transmitting sinusoidal uniform gratings,” *Opt. Eng.*, vol. 45, no. 1, p. 015802, 2006.
- [19] L. B. Glebov, J. Lumeau, S. Mokhov, V. I. Smirnov, and B. Y. Zeldovich, “Reflection of light by composite volume holograms: Fresnel corrections and Fabry-Perot spectral filtering,” *J. Opt. Soc. Am. A*, vol. 25, no. 3, pp. 751–64, 2008.
- [20] A. Podvyaznyy, G. Venus, V. Smirnov, D. Hostutler, and L. Glebov, “250 W LD bar pump source with 10 GHz spectral width for rubidium vapor medium,” *Proc. SPIE Vol.*, vol. 7686, 76860P, 2010.
- [21] L. H. Lin, “Method of Characterizing Hologram-Recording Materials,” *J. Opt. Soc. Am.*, vol. 61, no. 2, pp. 203–208, 1971.
- [22] R. Collier, C. Burchardt, and L. Lin, *Optical Holography*. New York: Academic, 1971.
- [23] D. Gabor, “A New Microscopic Principle,” *Nature*, vol. 161, no. 4098, pp. 777–778, 1948.
- [24] J. M. Kim, H. I. Bjelkhagen, and N. J. Phillips, “HOEs recorded in silver halide sensitised gelatin emulsions,” *Proc. SPIE*, vol. 3956, pp. 354–366, 2000.
- [25] T. A. Shankoff, “Phase Holograms in Dichromated Gelatin,” *Appl. Opt.*, vol. 7, no. 10, pp. 2101–2105, 1968.
- [26] B. J. Chang and C. D. Leonard, “Dichromated gelatin for the fabrication of holographic optical elements,” *Appl. Opt.*, vol. 18, no. 14, pp. 2407–17, 1979.

- [27] T. Kubota, T. Ose, M. Sasaki, and K. Honda, "Hologram formation with red light in methylene blue sensitized dichromated gelatin.," *Appl. Opt.*, vol. 15, no. 2, pp. 556–8, 1976.
- [28] L. Dhar, A. Hale, H. E. Katz, M. Schilling, M. G. Schnoes, and F. C. Schilling, "Recording media that exhibit high dynamic range for digital holographic data storage," *Opt. Lett.*, vol. 24, no. 7, pp. 487–489, 1999.
- [29] W. S. Colburn and K. a Haines, "Volume hologram formation in photopolymer materials.," *Appl. Opt.*, vol. 10, no. 7, pp. 1636–41, 1971.
- [30] S.-D. Wu and E. N. Glytsis, "Holographic grating formation in photopolymers: analysis and experimental results based on a nonlocal diffusion model and rigorous coupled-wave analysis," *J. Opt. Soc. Am. B*, vol. 20, no. 6, p. 1177, 2003.
- [31] R. T. Ingwall and H. L. Fielding, "Hologram recording with a new photopolymer system," *Opt. Eng.*, vol. 24, no. 5, pp. 808–811, 1985.
- [32] D. Yu, H. Liu, H. Wang, J. Wang, Y. Jiang, and X. Sun, "Improvement of holographic thermal stability in phenanthrenequinone-doped poly(methyl methacrylate-co-methacrylic acid) photopolymer," *Opt. Eng.*, vol. 50, no. 8, p. 085803, 2011.
- [33] T. N. Smirnova, O. V. Sakhno, I. a. Strelets, and E. a. Tikhonov, "Temperature stability and radiation resistance of holographic gratings on photopolymer materials," *Tech. Phys.*, vol. 43, no. 6, pp. 708–713, 1998.
- [34] F. S. Chen, J. T. LaMacchia, and D. B. Fraser, "Holographic Storage in Lithium Niobate," *Appl. Phys. Lett.*, vol. 13, no. 7, p. 223, 1968.
- [35] G. Cadena, O. Momtahan, and A. Adibi, "Simple and efficient software-based stabilized holographic recording system," *Opt. Eng.*, vol. 45, no. 12, p. 125801, 2006.
- [36] P. a Santos, L. Cescato, and J. Frejlich, "Interference-term real-time measurement for self-stabilized two-wave mixing in photorefractive crystals.," *Opt. Lett.*, vol. 13, no. 11, pp. 1014–6, 1988.
- [37] S. I. Stepanov, "Applications of photorefractive crystals," *Rep. Prog. Phys.*, vol. 57, pp. 39–116, 1994.
- [38] M. P. Bernal, H. Coufal, R. K. Grygier, J. a Hoffnagle, C. M. Jefferson, R. M. Macfarlane, R. M. Shelby, G. T. Sincerbox, P. Wimmer, and G. Wittmann, "A precision tester for studies of holographic optical storage materials and recording physics.," *Appl. Opt.*, vol. 35, no. 14, pp. 2360–74, 1996.

- [39] J. J. Amodei, "Holographic Pattern Fixing in Electro-Optic Crystals," *Appl. Phys. Lett.*, vol. 18, no. 12, p. 540, 1971.
- [40] A. Samui, "Holographic Recording Medium," *Recent Patents Mater. Sci.*, vol. 1, no. 1, pp. 74–94, 2008.
- [41] J. Canning, "Fibre gratings and devices for sensors and lasers," *Laser Photonics Rev.*, vol. 2, no. 4, pp. 275–289, 2008.
- [42] K. O. Hill, Y. Fujii, D. C. Johnson, and B. S. Kawasaki, "Photosensitivity in optical fiber waveguides: Application to reflection filter fabrication," *Appl. Phys. Lett.*, vol. 32, no. 10, pp. 647–649, 1978.
- [43] E. Fertein, C. Przygodzki, H. Delbarre, a Hidayat, M. Douay, and P. Niay, "Refractive-Index Changes of Standard Telecommunication Fiber through Exposure to Femtosecond Laser Pulses at 810 nm," *Appl. Opt.*, vol. 40, no. 21, pp. 3506–8, 2001.
- [44] L. B. Glebov, "Kinetics modeling in photosensitive glass," *Opt. Mater. (Amst.)*, vol. 25, no. 4, pp. 413–418, 2004.
- [45] O. M. Efimov, L. B. Glebov, and V. I. Smirnov, "High-frequency Bragg gratings in a photothermorefractive glass," *Opt. Lett.*, vol. 25, no. 23, pp. 1693–5, 2000.
- [46] O. M. Efimov, L. B. Glebov, and V. I. Smirnov, "Diffractive Optical Elements in Photosensitive Inorganic Glasses," *Inorganic Optical Materials III*, vol. 4452, pp. 39–47, 2001.
- [47] K. O. Hill, B. Malo, F. Bilodeau, D. C. Johnson, and J. Albert, "Bragg gratings fabricated in monomode by UV exposure through a phase mask photosensitive optical fiber," *Appl. Phys. Lett.*, vol. 62, no. 10, pp. 1035–1037, 1993.
- [48] A. Martinez, M. Dubov, I. Khrushchev, and I. Bennion, "Direct writing of fibre Bragg gratings by femtosecond laser," *Electron. Lett.*, vol. 40, no. 19, pp. 19–20, 2004.
- [49] K. O. Hill and G. Meltz, "Fiber Bragg grating technology fundamentals and overview," *J. Light. Technol.*, vol. 15, no. 8, pp. 1263–1276, 1997.
- [50] E. N. Leith and J. Upatnieks, "Reconstructed Wavefronts and Communication Theory," *J. Opt. Soc. Am.*, vol. 52, no. 10, p. 1123, 1962.
- [51] G. J. Steckman, a Pu, and D. Psaltis, "Storage density of shift-multiplexed holographic memory," *Appl. Opt.*, vol. 40, no. 20, pp. 3387–94, 2001.

- [52] G. B. Ingersoll and J. R. Leger, "Theoretical analysis of multiplexed volume holograms for spectral beam combining," *Proc. SPIE*, vol. 7195, 71951P, 2009.
- [53] B. Moslehi, P. Harvey, J. Ng, and T. Jansson, "Fiber-optic wavelength-division multiplexing and demultiplexing using volume holographic gratings," *Opt. Lett.*, vol. 14, no. 19, pp. 1088–1090, 1989.
- [54] R. Kowarschik, "Diffraction efficiency of sequentially stored gratings in reflection volume holograms," *Opt. Quantum Electron.*, vol. 10, no. 2, pp. 171–178, 1978.
- [55] L. Cao, X. Ma, Q. He, H. Long, M. Wu, and G. Jin, "Imaging spectral device based on multiple volume holographic gratings," *Opt. Eng.*, vol. 43, no. 9, p. 2009, 2004.
- [56] H. Ishio, J. Minowa, and K. Nosu, "Review and Status of WaveLength-Division-Multiplexing Technology and Its Application," *J. Light. Technol.*, vol. LT-2, no. 4, pp. 448–463, 1984.
- [57] S. Breer and K. Buse, "Wavelength demultiplexing with volume phase holograms in photorefractive lithium niobate," *Appl. Phys. B Lasers Opt.*, vol. 66, no. 3, pp. 339–345, 1998.
- [58] Y. Luo, P. J. Gelsinger, J. K. Barton, G. Barbastathis, and R. K. Kostuk, "Optimization of multiplexed holographic gratings in PQ-PMMA for spectral-spatial imaging filters.," *Opt. Lett.*, vol. 33, no. 6, pp. 566–8, 2008.
- [59] O. Beyer, I. Nee, F. Havermeier, and K. Buse, "Holographic recording of Bragg gratings for wavelength division multiplexing in doped and partially polymerized poly(methyl methacrylate).," *Appl. Opt.*, vol. 42, no. 1, pp. 30–7, 2003.
- [60] Y. Painchaud, H. Chotard, A. Mailloux, and Y. Vasseur, "Superposition of chirped fibre Bragg grating for third-order dispersion compensation over 32 WDM channels," *Electron. Lett.*, vol. 38, no. 24, pp. 1572–1573, 2002.
- [61] M. J. Cole, W. H. Loh, R. I. Laming, M. N. Zervas, and S. Barcelos, "Moving fibre/phase mask-scanning beam technique for enhanced flexibility in producing fibre gratings with uniform phase mask," *Electr. Eng.*, vol. 31, no. 17, pp. 1488–1490, 1995.
- [62] D. C. J. Reid, C. M. Ragdale, I. Bennion, D. J. Robbins, J. Buus, and W. J. Stewart, "Phase-Shifted Moire Grating Fibre Resonators," *Electron. Lett.*, vol. 26, no. 1, pp. 10–12, 1990.
- [63] T. Y. Fan, "Laser Beam Combining for High-Power , High-Radiance Sources," *Sel. Top. Quantum Electron.*, vol. 11, no. 3, pp. 567–577, 2005.

- [64] M. C. Farries, A. C. Carter, G. G. Jones, and I. Bennion, "Tuneable Multiwavelength Semiconductor Laser with Single Fibre Output," *Electron. Lett.*, vol. 27, no. 17, pp. 1498–1499, 1991.
- [65] S. Tidwell, S. Roman, D. Jander, and D. Lowenthal, "Spectral Beam Combining of diode laser bars to achieve efficient , near diffraction limited , output power," *High-Power Diode Laser Technology and Applications*, vol. 4973, pp. 42–46, 2003.
- [66] C. Wirth, O. Schmidt, I. Tsybin, T. Schreiber, T. Peschel, and F. Brückner, "2 kW incoherent beam combining of four narrow-linewidth photonic crystal fiber amplifiers," *Opt. Express*, vol. 17, no. 3, pp. 1178–1183, 2009.
- [67] O. Andrusyak, V. Smirnov, G. Venus, N. Vorobiev, and L. Glebov, "Applications of volume Bragg gratings for spectral control and beam combining of high power fiber lasers," *Proc. SPIE*, vol. 7195, 71951Q, 2009.
- [68] H. Bruesselbach, S. Wang, M. Minden, C. Jones, and M. Mangir, "Coherent phase-locking of seven laser transmitters on a 408 meter outdoor range," *CLEO*, CTuG5, 2005.
- [69] H. Bruesselbach, M. Minden, J. L. Rogers, D. C. Jones, and M. S. Mangir, "200 W self-organized coherent fiber arrays," *CLEO*, CMDD4, 2005.
- [70] S. J. McNaught, H. Komine, S. B. Weiss, R. Simpson, A. M. Johnson, J. Machan, C. P. Asman, M. Weber, G. C. Jones, M. M. Valley, A. Jankevics, D. Burchman, M. McClellan, J. Sollee, J. Marmo, and H. Injeyan, "100 kW Coherently Combined Slab MOPAs," *CLEO-IQEC*, CThA1, 2009.
- [71] S. J. Mcnaught, J. E. Rothenberg, P. A. Thielen, M. G. Wickham, M. E. Weber, and G. D. Goodno, "Coherent Combining of a 1.26-kW Fiber Amplifier," *Lasers, Sources and Related Photonic Devices*, p. AMA2, 2010.
- [72] A. Jain, D. Drachenberg, O. Andrusyak, G. Venus, V. Smirnov, and L. Glebov, "Coherent and spectral beam combining of fiber lasers using volume Bragg gratings," *Proc. SPIE*, vol. 7686, p. 768615, 2010.
- [73] A. Jain, O. Andrusyak, G. Venus, V. Smirnov, and L. Glebov, "Passive coherent locking of fiber lasers using volume Bragg gratings," *Proc. SPIE 7580*, 2010, vol. 7580, p. 75801S.
- [74] K. Sayano, H. E. Miller, and N. Karlovac, "Subpicometer accuracy laser wavelength sensor using multiplexed Bragg gratings," *IEEE Photonics Technol. Lett.*, vol. 9, no. 11, pp. 1493–1495, 1997.

- [75] P. J. Gelsinger-Austin, Y. Luo, J. M. Watson, R. K. Kostuk, G. Barbastathis, J. K. Barton, and J. M. Castro, "Optical Design for a Spatial-Spectral Volume Holographic Imaging System.," *Opt. Eng.*, vol. 49, no. 4, p. 43001, 2010.
- [76] E. S. Maniloff and K. M. Johnson, "Maximized photorefractive holographic storage," *J. Appl. Phys.*, vol. 70, no. 9, p. 4702, 1991.
- [77] K. Anderson and K. Curtis, "Polytopic multiplexing.," *Opt. Lett.*, vol. 29, no. 12, pp. 1402–4, 2004.
- [78] Q. Zhai, S. Tao, T. Zhang, and D. Wang, "Investigation on mechanism of multiple holographic recordings in photopolymers," *Proc. SPIE*, vol. 7505, 75051F, 2009.
- [79] H. Lee, "Cross-talk effects in multiplexed volume holograms.," *Opt. Lett.*, vol. 13, no. 10, pp. 874–6, 1988.
- [80] R. Alferness and S. K. Case, "Coupling in doubly exposed, thick holographic gratings," *J. Opt. Soc. Am.*, vol. 65, no. 6, p. 730, 1975.
- [81] D. Brotherton-Ratcliffe, "Analytical treatment of the polychromatic spatially multiplexed volume holographic grating.," *Appl. Opt.*, vol. 51, no. 30, pp. 7188–99, 2012.
- [82] G. E. Moss, "Method for making balanced multiple exposures in single layer holograms," *SPIE*, vol. 3011, pp. 194–199, 1997.
- [83] E. M. de Miguel-Sanz, J. Limeres, L. Arizmendi, and M. Carrascosa, "Nonlinear generation of higher-order combinational gratings during sequential recording in LiNbO₃," *J. Opt. Soc. Am. B*, vol. 16, no. 10, p. 1658, 1999.
- [84] E. Goodwin and J. C. Wyant, *Field Guide to Interferometric Optical Testing*. SPIE Press, 2006.
- [85] N. Chen, "Aberrations of volume holographic grating," *Opt. Lett.*, vol. 10, no. 10, pp. 472–474, 1985.
- [86] Y. Suzaki, J. Mohri, K. Nakayama, M. Ando, K. Sakamoto, M. Yamauchi, Y. Mizutani, T. Yokouchi, and S. Ejima, "Effect of Spherical Aberration on Fabrication of Fiber Bragg Gratings," *Jpn. J. Appl. Phys.*, vol. 45, no. 6A, pp. 5035–5038, 2006.
- [87] M. Ma, X. Wang, and F. Wang, "Aberration measurement of projection optics in lithographic tools based on two-beam interference theory," *Appl. Opt.*, vol. 45, no. 32, pp. 8200–8208, 2006.

- [88] M. Yamada and K. Sakuda, "Analysis of almost-periodic distributed feedback slab waveguides via a fundamental matrix approach," *Appl. Opt.*, vol. 26, no. 16, pp. 3474–3478, 1987.
- [89] M. SeGall, D. Ott, I. Divliansky, and L. Glebov, "Effect of aberrations in a holographic system on reflecting volume Bragg gratings," *Appl. Opt.*, vol. 52, no. 32, pp. 7826–7831, 2013.
- [90] G. Rousset, "Wavefront Sensing," *NATO ASI Ser. C Math. Phys. Sci. Study Inst.*, vol. 423, pp. 115–138, 1994.
- [91] T. Y. Chew, R. M. Clare, and R. G. Lane, "A comparison of the Shack–Hartmann and pyramid wavefront sensors," *Opt. Commun.*, vol. 268, no. 2, pp. 189–195, 2006.
- [92] S. Velghe, J. Primot, N. Guérineau, M. Cohen, and B. Wattellier, "Wave-front reconstruction from multidirectional phase derivatives generated by multilateral shearing interferometers," *Opt. Lett.*, vol. 30, no. 3, pp. 245–247, 2005.
- [93] G. B. Venus, V. I. Smirnov, and L. B. Glebov, "Spectral stabilization of laser diodes by external Bragg resonator," *SSDLTR*, no. 407, pp. 1–4, 2004.
- [94] D. B. Neumann and H. W. Rose, "Improvement of recorded holographic fringes by feedback control," *Appl. Opt.*, vol. 6, no. 6, pp. 1097–1104, 1967.
- [95] D. R. Macquigg, "Hologram fringe stabilization method," *Appl. Opt.*, vol. 16, no. 2, pp. 291–2, 1977.
- [96] A. A. Kamshilin, J. Frejlich, and L. H. Cescato, "Photorefractive crystals for the stabilization of the holographic setup," *Appl. Opt.*, vol. 25, no. 14, p. 2375, 1986.
- [97] C. C. Guest and T. K. Gaylord, "Phase stabilization system for holographic optical data processing," *Appl. Opt.*, vol. 24, no. 14, p. 2140, 1985.
- [98] J. D. Muhs, P. a Leilabady, and M. Corke, "Fiber-optic holography employing multiple beam fringe stabilization and object/reference beam intensity variability," *Appl. Opt.*, vol. 27, no. 17, pp. 3723–7, 1988.
- [99] J. W. Goodman, "Holography," in *Introduction to Fourier Optics*, 2nd ed., New York: McGraw-Hill, pp. 336–346, 1996.
- [100] S. Wise, V. Quetschke, a. Deshpande, G. Mueller, D. Reitze, D. Tanner, B. Whiting, Y. Chen, a. Tünnermann, E. Kley, and T. Clausnitzer, "Phase Effects in the Diffraction of Light: Beyond the Grating Equation," *Phys. Rev. Lett.*, vol. 95, no. 1, p. 013901, 2005.

- [101] C. Rothleitner and O. Francis, "On the influence of the rotation of a corner cube reflector in absolute gravimetry," *Metrologia*, vol. 47, no. 5, pp. 567–574, 2010.
- [102] G. M. Kuan and S. J. Moser, "Sensitivity of Optical Metrology Calibration to Measured Corner Cube Retroreflector Parameters for the Space Interferometry Mission," *Proc. SPIE*, vol. 4852, pp. 795–802, 2013.
- [103] B. Saleh and M. Teich, *Fundamentals of Photonics*. John Wiley & Sons, Inc., p. 86, 1991
- [104] B. Anderson, G. B. Venus, D. Ott, I. Divliansky, and L. B. Glebov, "Transverse Mode Selection in a thin rod Yb:YAG laser by volume Bragg gratings," *Solid State and Diode Laser Technology Review*, pp. 2–5, 2012.
- [105] D. Drachenberg, I. Divliansky, V. Smirnov, G. Venus, and L. Glebov, "High Power Spectral Beam Combining of Fiber Lasers with Ultra High Spectral Density by Thermal Tuning of Volume Bragg Gratings," *Proc. SPIE*, vol. 7914, no. 1, p. 79141F, 2011.
- [106] "ISO Standard 11146, Lasers and laser-related equipment – Test methods for laser beam widths, divergence angles and beam propagation ratios." 2005.
- [107] D. R. Drachenberg, O. Andrusyak, I. Cohanoschi, I. Divliansky, O. Mokhun, A. Podvyaznyy, V. Smirnov, G. B. Venus, and L. B. Glebov, "Thermal tuning of volume Bragg gratings for high power spectral beam combining," *Proc SPIE 7580*, 2010, vol. 7580, p. 75801U.
- [108] F. Ghiringhelli and M. Zervas, "Time delay distribution in Bragg gratings," *Phys. Rev. E*, vol. 65, no. 3, p. 036604, Feb. 2002.
- [109] C. Lu, A. Flores, E. Bochove, W. P. Roach, V. Smirnov, and L. B. Glebov, "Active coherent superposition of five fiber amplifiers at 670W using multiplexed volume Bragg gratings," *Proc. SPIE*, vol. 8601, 86011A, 2013.
- [110] R. Kowarschik, "Diffraction Efficiency of Sequentially Stored Gratings in Transmission Volume Holograms," *Opt. Acta Int. J. Opt.*, vol. 25, no. 1, pp. 67–81, 1978.
- [111] S. Mokhov, A. Jain, C. Spiegelberg, V. Smirnov, O. Andrusyak, G. Venus, B. Zeldovich, and L. Glebov, "Multiplexed Reflective Volume Bragg Grating for Passive Coherent Beam Combining," *Laser Science XXVI*, LWG2, 2010.
- [112] F. Bakhti and P. Sansonetti, "Wide bandwidth, low loss and highly rejective doubly phase-shifted UV-written fibre bandpass filter," *Electron. Lett.*, vol. 32, no. 6, pp. 581–582, 1996.

- [113] Y. Painchaud, M. Aubé, G. Brochu, and M. Picard, “Ultra-narrowband notch filtering with highly resonant fiber Bragg gratings,” *Opt. Soc. Am.*, p. BTuC3, 2010.
- [114] J. Lumeau, V. Smirnov, and L. B. Glebov, “Phase-shifted volume Bragg gratings in photo-thermo-refractive glass,” *Proc. SPIE*, vol. 6890, no. 407, p. 68900A, 2008.
- [115] P. Baumeister, *Optical coating technology*. SPIE Optical Engineering Press, 2004.
- [116] S.-H. Kim and C. G. Fonstad, “Tunable narrow-band thin-film waveguide grating filters,” *IEEE J. Quantum Electron.*, vol. 15, no. 12, pp. 1405–1408, Dec. 1979.
- [117] Y. O. Barmenkov, D. Zalvidea, S. Torres-Peiró, J. L. Cruz, and M. V Andrés, “Effective length of short Fabry-Perot cavity formed by uniform fiber Bragg gratings,” *Opt. Express*, vol. 14, no. 14, pp. 6394–9, 2006.
- [118] K. Ennser, M. N. Zervas, and R. I. Laming, “Optimization of apodized linearly chirped Fiber Gratings for Optical Communications,” *IEEE J. Quantum Electron.*, vol. 34, no. 5, pp. 770–778, 1998.